



저작자표시-비영리-변경금지 2.0 대한민국

이용자는 아래의 조건을 따르는 경우에 한하여 자유롭게

- 이 저작물을 복제, 배포, 전송, 전시, 공연 및 방송할 수 있습니다.

다음과 같은 조건을 따라야 합니다:



저작자표시. 귀하는 원저작자를 표시하여야 합니다.



비영리. 귀하는 이 저작물을 영리 목적으로 이용할 수 없습니다.



변경금지. 귀하는 이 저작물을 개작, 변형 또는 가공할 수 없습니다.

- 귀하는, 이 저작물의 재이용이나 배포의 경우, 이 저작물에 적용된 이용허락조건을 명확하게 나타내어야 합니다.
- 저작권자로부터 별도의 허가를 받으면 이러한 조건들은 적용되지 않습니다.

저작권법에 따른 이용자의 권리는 위의 내용에 의하여 영향을 받지 않습니다.

이것은 [이용허락규약\(Legal Code\)](#)을 이해하기 쉽게 요약한 것입니다.

[Disclaimer](#)

Doctor of Philosophy

Characterization of Optical Properties of Single Gold Nanoparticles
and Their Applications

The Graduate School of the University of Ulsan

Department of Chemistry

Geun Wan Kim

Characterization of Optical Properties of Single Gold Nanoparticles
and Their Applications

Supervisor Professor Ji Won Ha

A Dissertation

Submitted to

The Graduate School of the University of Ulsan

In partial fulfillment of the requirements

for the degree of

Doctor of Philosophy in Department of Chemistry

by

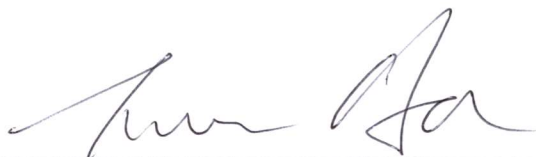
Geun Wan Kim

M.S., University of Ulsan, Ulsan, Korea 2018

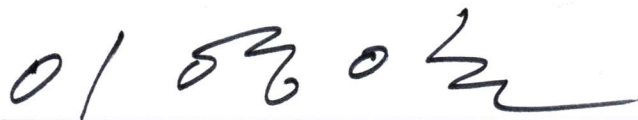
February, 2022

Characterization of Optical Properties of Single Gold Nanoparticles
and Their Applications

This certifies that the dissertation of Geun wan Kim is approved.



Committee Member Prof. Ji Won Ha



Committee Member Prof. Youngil Lee



Committee Member Prof. Jong Wook Hong



Committee Member Prof. Yong-Ill Lee



Committee Member Prof. Seong Ho Kang

Department of Chemistry

Ulsan, Korea

February, 2022

국문요약

금 나노입자는 지난 수십 년간 고유한 광학 및 화학적 특성으로 인해 국부 표면 플라즈몬 공명 (Localized surface plasmon resonance, LSPR) 감지, 광학 탐침, 약물 전달, 광열 치료, 진단, 표면 증폭 라만 분광법 (Surface enhanced Raman spectroscopy, SERS)와 같은 다양한 영역에서 널리 연구되고 있다. 금 나노입자의 독특한 광학적 특성은 LSPR 효과로 인해 나타나고, 크기, 모양, 주변 매질의 굴절률에 따라 달라진다. LSPR 효과란 특정 파장의 빛이 플라즈모닉 나노입자에 조사되었을 때, 전도띠의 자유 전자가 집단적으로 진동하며 빛을 흡수하게 되는 현상을 말한다. 본 연구에서는 광학 현미경을 이용하여 다양한 모양을 가진 금 나노입자의 광학적 특성과 그 응용에 대해 연구하였고, 보다 구체적인 내용은 아래와 같다.

2장에서는 표면에 여러 개의 긴 가지가 돌출되어 있는 별 모양의 금 나노입자와 짧은 가지가 있는 성게형 금 나노입자의 LSPR 파장에서 편광과 파장에 의존하는 비초점 산란 특성을 단일 입자 수준에서 연구하였다. 입자에 조사되는 빛의 편광을 회전시키면서 산란광의 세기 변화를 관찰하였을 때, 금 나노입자의 산란광의 세기는 편광의 회전에 따라 주기적으로 변하였다. 그러나 비초점에서 나타나는 입자의 특징적인 산란 패턴의 형태는 편광의 회전에 관계없이 변하지 않았다. 이를 통해 다중 가지 나노 입자가 편광 감응성 광특성을 증명하였다. 게다가, 입자에

조사되는 빛의 파장을 변경해주었을 때, 비초점 산란 패턴이 보여주는 단일 쌍극자의 배향이 변경될 뿐만 아니라, 편광의 회전에 따른 산란광의 세기의 주기도 바뀔음을 확인하여, 실험에 사용된 입자가 파장 감응성 광특성을 가지고 있음도 확인하였다.

3장에서 플라즈모닉 금 나노로드 (Au nanorods, AuNRs)는 많은 생물물리학 연구에서 광학 배향 탐침으로 널리 연구되었다. 그러나, 대물 렌즈의 동일한 초점 평면에서 AuNRs의 3차원 배향을 규명하는 일은 매우 까다롭다. 이 문제를 극복하기 위해 타원형 또는 구형 다공성 실리카 껍질로 싸인 단일 AuNR (AuNR@mSiO₂)를 제작했다. 구형 AuNR@mSiO₂는 중심 AuNR이 3차원 공간에서 무작위로 배향을 가지기 때문에 AuNRs의 3차원 배향을 같은 초점 평면에서 대용량으로 동시에 관측 가능하였다. 또한, 구형의 AuNRs@mSiO₂와 flow cell을 이용해 입자에 외력을 가하여 AuNRs@mSiO₂의 굴러가도록 하였고, 이에 따른 중심 AuNRs의 배향 변화를 In-situ로 유도하고 관측하였다. 마지막으로, 다기능성 광학 탐침을 개발하기 위해, 미분 간섭 현미경으로 동적 생물학적 환경에서 AuNRs@mSiO₂를 다기능 방향 탐침으로 사용 가능성을 보였다.

4장에서는 산소 플라즈마 처리와 수은 아말감 반응이 단일 AuNR 및 AuNRs@mSiO₂의 구조와 스펙트럼에 어떻게 영향을 미치는지를 연구하였다. AuNR 중형비는 산소 플라즈마 처리와 수은 아말감 반응의 시간에 따라 점차 감소하였다. 그러나 AuNRs@mSiO₂는 수은 아말감

반응에도 불구하고 다공성 구조 꺾질 때문에 구조적 안정성이 더 높았다. 따라서 AuNR의 종횡비 감소의 영향 없이 수은 아말감 반응에 의한 광 특성 변화를 관찰할 수 있었다. 이 장에서는 단일 입자 수준에서 수은 아말감 반응과 스펙트럼 변화 사이의 관계에 대한 기본적인 정보를 제공한다.

Abstract

Over the few decades, gold nanoparticles (AuNPs) have been widely used in various areas such as localized surface plasmon resonance (LSPR) sensing, optical probe, drug delivery, photo-thermal therapy, diagnostics, and surface-enhanced Raman spectroscopy (SERS) due to their unique optical and chemical properties. The unique optical properties of AuNPs depend on the size, shape, and refractive index of a surrounding medium because of the LSPR effect. The LSPR is the collective oscillation of free electrons of the conduction band with incident light. In this study, we investigated the optical properties of AuNPs with various shapes under optical microscopy and their application.

In chapter 2, we demonstrate the polarization- and wavelength-dependent defocused scattering properties at the LSPR wavelengths of single Au nanostars with multiple long branches protruding from their surfaces and Au nanourchins with multiple short branches. The defocused scattering intensities of multiple branch nanoparticles at two LSPR excitation wavelengths changed periodically as a function of the rotational angle of a polarizer, whereas the doughnut-shaped scattering pattern remained unaltered. Furthermore, the characteristic doughnut-shaped defocused scattering pattern enabled the resolution of the spatial field distributions of single dipoles on the same AuNPs surface at two LSPR wavelengths.

In chapter 3, many biophysical studies have investigated plasmonic gold nanorods (AuNRs) as optical orientation probes. However, characterizing the various three-dimensional (3D) orientations of anisotropic AuNPs in the same focal plane of

the objective lens is challenging. We fabricated single AuNRs (10 nm × 30 nm) coated with either an elliptical or spherical mesoporous silica shell (mSiO₂) to overcome this challenge. The spherical AuNRs@mSiO₂ achieved high-throughput detection because the AuNR core is randomly oriented in 3D space. Additionally, by taking advantage of the spherical shape of the AuNRs@mSiO₂, in situ monitoring of the tilting angles of the anisotropic core is achieved by inducing the movement of the AuNRs@mSiO₂ through applying an external fluidic force in a flow cell. Furthermore, we demonstrate the use of AuNRs@mSiO₂ as multifunctional orientation probes in dynamic biological environments under DIC microscopy.

Chapter 4 demonstrates how oxygen plasma treatment and Hg amalgamation affect the structural, spectral changes in single AuNRs and AuNRs@mSiO₂. The samples subjected to different reaction times were characterized by scanning electron microscopy and dark-field microscopy. The aspect ratio of bare AuNRs was a gradually decreasing function of plasma treatment and amalgamation time. However, AuNRs@mSiO₂ showed higher structural stability due to the mSiO₂ shell against the Hg elemental. Therefore, we observed the change in optical properties caused by the Hg deposition and inward diffusion without the effect of the decrease in aspect ratio. This chapter provides fundamental information on the relationship between the physical, chemical reaction and structural, spectral changes of AuNRs at the single particle level.

Index

국문요약	i
Abstract	iv
Index	vi
Figure index	ix
Chapter 1. General Introduction	1
Objectives and Scope of This Work	1
1.1 Localized Surface Plasmon Resonance	2
1.2 Optical Imaging Technique	3
1.3 Single Particle Orientation and Rotation Tracking	5
1.4 References	7
1.5 Figure and Captions	12
Chapter 2. Wavelength- and Polarization-Dependence of Multiple Branch Gold Nanoparticle	18
2.1 Direct Visualization of Wavelength-Dependent Single Dipoles Generated on Single Gold Nanourchins with Sharp Branches	18
2.1.1 Abstract	18
2.1.2 Introduction	19
2.1.3 Experimental Section	21
2.1.4 Results and Discussion	23
2.1.5 Conclusion	27
2.1.6 References	29
2.1.7 Figures and Captions	35
2.1.8 Supplementary Materials	40
2.2 Polarization- and Wavelength-Dependent Defocused Scattering Imaging of Single Gold Nanostars with Multiple Long Branches	43
2.2.1 Abstract	43
2.2.2 Introduction	44
2.2.3 Experimental Section	46
2.2.4 Results and Discussion	48
2.2.5 Conclusion	52
2.2.6 References	54
2.2.7 Figures and Captions	61
2.2.8 Supplementary Materials	66
Chapter 3. High-Throughput Characterization and Real Time Tracking the Rotational Motion of Single AuNR@mSiO ₂	68

3.1 High-Throughput in-focus Differential Interference Contrast Imaging of Three-Dimensional Orientations of Single Gold Nanorods Coated with a Mesoporous Silica Shell	68
3.1.1 Abstract	68
3.1.2 Introduction	69
3.1.3 Experimental Section	70
3.1.4 Results and Discussion	72
3.1.5 Conclusion	77
3.1.6 References	79
3.1.7 Figures and Captions	83
3.1.8 Supplementary Materials	88
3.2 High-Throughput Characterization and In Situ Control of Three-Dimensional Orientations of Single Gold Nanorods Coated with Spherical Mesoporous Silica Shell	92
3.2.1 Abstract	92
3.2.2 Introduction	93
3.2.3 Experimental Section	95
3.2.4 Results and Discussion	98
3.2.5 Conclusion	106
3.2.6 References	108
3.2.7 Figures and Captions	113
3.2.8 Supplementary Materials	118
3.3 Mesoporous Silica Shell-Coated Single Gold Nanorods as Multifunctional Orientation Probes in Dynamic Biological Environments	124
3.3.1 Abstract	124
3.3.2 Introduction	125
3.3.3 Experimental Section	126
3.3.4 Results and Discussion	129
3.3.5 Conclusion	134
3.3.6 References	135
3.3.7 Figures and Captions	139
3.3.8 Supplementary Materials	144
Chapter 4. Structural and Spectral Changes of AuNPs in Physical and Chemical Reactions.....	145
4.1 Single-Particle Study: Effects of Oxygen Plasma Treatment on Structural and Spectral Changes of Anisotropic Gold Nanorods	145
4.1.1 Abstract	144
4.1.2 Introduction	146
4.1.3 Experimental Section	148
4.1.4 Results and Discussion	149
4.1.5 Conclusion	153
4.1.6 References	155

4.1.7 Figures and Captions	161
4.1.8 Supplementary Materials	165
4.2 Single-Particle Study: Plasmonic Damping Induced by Mercury Amalgamation in Mesoporous Silica Coated Gold Nanorods	168
4.2.1 Abstract	168
4.2.2 Introduction	169
4.2.3 Experimental Section	170
4.2.4 Results and Discussion	172
4.2.5 Conclusion	175
4.2.6 References	177
4.2.7 Figures and Captions	182
4.2.8 Supplementary Materials	187
Chapter 5. Future Works	188
Acknowledgments	190

Figure index

Figure 1. Schematic image of localized surface plasmon resonance	12
Figure 2. Scheme of advantage of single particle measurement	13
Figure 3. Photograph to show the experimental setup for single particle spectroscopy	14
Figure 4. The working principle of DF microscopy and spectroscopy	15
Figure 5. The working principle of DIC microscopy. The incident light is split into two orthogonally linearly polarized beams by the first Nomarski prism. Two beams pass through the sample and are recombined by the second Nomarski prism to create an interference pattern	16
Figure 6. (A) Schematic diagram to show the definitions of the polar angle θ and azimuthal angle φ of single dipole generated on the AuNP surface in 3D space. (B) Schematic diagram depicting three-perpendicular dipoles along the three axes. E_a denotes the scattering electric field of the nanorod along the main long axis	17
Figure 7. (A) SEM image of 90 nm AuNUs with sharp and short branches. (B) UV-Vis absorption spectrum of 90 nm AuNUs dispersed in water. A single broad peak is observed at approximately 634 nm indicated by the yellow-dotted line	35
Figure 8. (A) DF scattering image of 90 nm AuNUs deposited on a glass slide. (B) Single particle scattering spectrum of AuNU1 highlighted with a red square in (A) . A single LSPR peak was observed around 650 nm for the AuNU1. The yellow-dotted lines indicate the incident LSPR wavelengths (600 nm, 640 nm, 700 nm) used in this study	36

Figure 9. (A) Normalized DF intensities for AuNU1 at the three different LSPR wavelengths as a function of the rotational angle. (B) Enlarged SEM image of a single AuNU with a spiky uneven surface. (C) Schematic diagram showing the generation of single dipoles with different wavelengths in multiple directions on the same AuNU surface 37

Figure 10. (A, C) Measured and best-matched simulation patterns of single AuNU1 on a glass slide at 600 nm. (B, D) Measured and best-matched simulation patterns of single AuNU1 at 700 nm. The white-dotted line shows the single dipole orientation generated on the AuNU surface at the LSPR wavelength. The scale bar represents 1 μm 38

Figure 11. (A) Changes in the normalized scattering intensities for three AuNUs (AuNU2 to AuNU4) at 640 nm as a function of the rotational angle. (B) Changes in the normalized scattering intensities for three AuNUs (AuNU2 to AuNU4) at 700 nm as a function of the rotational angle 39

Figure 12. (A) SEM image of AuNSs with sharp and long branches. The scale bar in the inset is 10 nm. (B) UV–Vis extinction spectrum of AuNSs dispersed in water. A single broad peak is observed at approximately 634 nm, as indicated by the red dashed line 61

Figure 13. (A) Focused DF scattering image of single AuNSs. (B) Defocused DF scattering image of the same AuNSs. (C) Scattering spectrum of AuNS1 in (A), a single AuNS. (D) Scattering spectrum of AuNS2 in (A). The red dashed lines indicate the incident LSPR wavelengths (640 nm, 700 nm) used in this study 62

curve), and **(C)** spherical AuNRs@mSiO₂ (blue curve). **(D)** Overlaid UV-vis extinction spectra of bare AuNRs (yellow curve), elliptical AuNRs@mSiO₂ (red curve), and spherical AuNRs@mSiO₂ (blue curve). The anisotropic AuNRs yielded two distinct LSPR peaks 83

Figure 18. **(A)** Schematic of bare AuNRs deposited on a glass slide. Their projected lengths are almost the same. **(B)** Schematic of elliptical AuNRs@mSiO₂ particles and their projections on a glass slide. **(C)** Schematic of spherical AuNRs@mSiO₂ particles with their AuNR cores randomly oriented in the shell. Their projected lengths depend on their spatial orientations, which are freely available in 3D space 84

Figure 19. **(A)** TEM image of spherical AuNRs@mSiO₂ with randomly oriented AuNR cores inside the silica shell. **(B)** SEM image of spherical AuNRs₂ particles, and **(C)** DIC image of AuNRs@mSiO₂ particles, showing their different orientations on the same focal plane. The color image was generated in ImageJ for better demonstration of bright and dark DIC images of AuNRs@mSiO₂. Note that high-throughput detection is possible 85

Figure 20. **(A)** DIC image of spherical AuNRs@mSiO₂. **(B)** DIC images of spherical AuNR1@mSiO₂ captured at different rotational angles (interval ¼ 30 °). **(C)** Dark and bright intensities of spherical AuNR1@mSiO₂ as functions of rotation angle. **(D)** DIC polarization anisotropy computed from the dark and bright intensities of the spherical AuNR1@mSiO₂ 86

Figure 21. Histograms showing the polar angle (θ) distributions of **(A)** elliptical AuNRs@mSiO₂ and **(B)** spherical AuNRs@mSiO₂, determined from the DIC

measurements	87
Figure S3. Schematic to show AuNRs embedded in a gel matrix at the different focal planes. The embedded AuNRs are measured by vertical scanning in the z-axis under DIC microscopy	88
Figure S4. DIC images of elliptical AuNR1@mSiO ₂ as a function of rotational angle with 10° increment from 0° to 180°	89
Figure S5. (A) Normalized DIC intensities of elliptical AuNR1@mSiO ₂ in Fig. S4 as a function of rotational angle. (B) Change in the DIC polarization anisotropy calculated from two dark and bright intensities in (A) for the elliptical AuNR1@mSiO ₂	90
Figure S6. Consecutive DIC images of the embedded AuNRs (25 nm × 73 nm) measured by z-axis scanning with a vertical step size of 40 nm. The AuNRs in gel matrix has random 3D orientations at the different focal planes	91
Figure 22. (A) Schematic showing bare AuNRs deposited on a glass slide, yielding projections having almost the same length. (B) Schematic depicting AuNRs@mSiO ₂ with the AuNR cores exhibiting random 3D orientations in the shell. The projected length varies depending on their 3D spatial orientations in the spherical shell. (C, D) TEM images of bare AuNRs (C) and AuNRs@mSiO ₂ (D), respectively	113
Figure 23. TEM image analysis based on a custom MATLAB script of the sizes (length and diameter) of bare AuNRs without the silica shell and AuNRs with the spherical mesoporous silica shell	114
Figure 24. (A) Schematic showing AuNRs embedded in a gel matrix at different focal	

planes. The embedded AuNRs need to be measured by vertical scanning in the z-axis.

(B) Schematic showing spherical AuNRs@mSiO₂ deposited on a glass slide at the same focal plane of the objective lens. The AuNR cores are positioned with random 3D orientations inside the silica shell 115

Figure 25. Defocused orientation imaging of spherical AuNRs@mSiO₂. **(A)** A DF scattering image of single AuNRs@mSiO₂ in the focal plane. **(B)** Single particle scattering spectra of two AuNRs@mSiO₂ indicated by a square in **(A)**. **(C)** Measured defocused image patterns of the two AuNRs@mSiO₂ (left). The white dashed line indicates the single dipole orientation. The scale bar represents 1 μm. The corresponding best-fit simulated scattering patterns for the two AuNRs@mSiO₂ are also presented (right). **(D)** The 3D spatial orientations of two AuNRs@mSiO₂ determined through the pattern match analysis are illustrated. The red line shows the determined 3D orientation, and the blue-dotted line is the corresponding in-plane projection 116

Figure 26. In situ control and tracking of positions and 3D orientations of single AuNRs@mSiO₂. **(A)** Schematic showing the concept of controlling the positions and spatial orientations of a single AuNR@mSiO₂ by applying an external fluidic force. **(B)** Doughnut-shaped defocused scattering images of AuNR3@mSiO₂ to show clear transitions between up and down in the opening direction on the patterns indicated by a white-dotted arrow. **(C)** Trajectory of the center position of AuNR3@mSiO₂ when moving forward by the external flow. **(D)** Real-time tracking of azimuthal (top) and polar (bottom) angles of AuNR3@mSiO₂ for 40 consecutive frames the temporal

resolution was 100 ms	117
Figure S7. UV–Vis extinction overlaid spectra of AuNRs without shell (blue curve) and AuNRs@mSiO ₂ (red curve). Two distinct LSPR peaks are observed for the anisotropic AuNRs	118
Figure S8. Changes in the DF scattering intensities of two in-focus AuNRs@mSiO ₂ (AuNR1@mSiO ₂ and AuNR2@mSiO ₂) in Fig. 25 as a function of polarization angle with 10° increment	119
Figure S9. (A) Consecutive DF images of the embedded AuNRs (25 nm × 73 nm) measured by z-axis scanning with a vertical step size of 40 nm. The AuNRs in gel matrix has random 3D orientations at the different focal planes. (B) Defocused scattering patterns of the four AuNRs circled in (A) obtained at the different focal planes. The white-dotted line shows an in-plane orientations of the AuNRs	120
Figure S10. (A) Consecutive DF scattering images of AuNRs@mSiO ₂ chosen from movie recorded at a temporal resolution of 100 ms. (B, C) Enlarged DF scattering images of AuNRs@mSiO ₂ recorded at 1 Frame (B) and 60 Frame (C), respectively	121
Figure S11. Consecutive DF images of a AuNR@mSiO ₂ chosen from recorded movie. This movie was recorded at the frame rate of 10 fps. The AuNR@mSiO ₂ is detached from a glass slide over time under the same external fluidic condition (a flow rate of 0.5 μL/min in a flow cell)	122
Figure S12. (A) Consecutive DF scattering images of AuNR3@mSiO ₂ as a function of frames obtained from recorded movie	123

Figure 27. (A) TEM image of AuNRs@mSiO₂. The average length and width are 120 and 40 nm. The inset illustrates the AuNRs@mSiO₂. **(B)** Normalized ultraviolet–visible (UV–Vis) extinction spectrum of AuNRs@mSiO₂ dispersed in water 139

Figure 28. (A) DF image of single AuNRs@mSiO₂ on a glass slide. **(B)** Single-particle scattering spectra of the two AuNRs@mSiO₂ (AuNR1@mSiO₂, AuNR2@mSiO₂) marked with a yellow square in **(A)**..... 140

Figure 29. (A) DIC image of single AuNRs@mSiO₂ with different orientations on a glass slide. The AuNRs@mSiO₂ were illuminated at their longitudinal SPR wavelength of 720 nm. The inset represents the definition of the orientation angle ϕ of a AuNR@mSiO₂ with respect to the dark polarization axis. **(B)** Single-particle scattering spectrum of AuNR3@mSiO₂, highlighted by the yellow square in **(A)**. The longitudinal SPR peak was observed at approximately 720 nm. **(C)** Polarization-dependent DIC images of single AuNR3@mSiO₂ obtained by rotating the stage in increments of 10° at 720 nm excitation 141

Figure 30. (A) DIC intensity profiles and **(B)** polarization anisotropy P of AuNR3@mSiO₂ as a function of rotation angle. In **(B)**, the experimental values of P (pink dots) fit the calculated P values well (green curve) 142

Figure 31. (A) DIC image of AuNR5@mSiO₂ bound onto a live cell membrane. **(B)** 20 successive DIC images of AuNR5@mSiO₂ chosen from recorded movie. The temporal resolution was 100 ms. **(C)** DIC polarization anisotropy P for AuNR5@mSiO₂ as a function of time for all consecutive frames in recorded movie 143

Figure S13. (A) DIC image of AuNR6@mSiO₂ bound onto a live cell membrane. (B) DIC polarization anisotropy P for AuNR6@mSiO₂ as a function of time for all consecutive frames. (C) 100 successive DIC images of AuNR6@mSiO₂ chosen from all consecutive frames in (B). The temporal resolution was 100 ms 144

Figure 32. Schematics of (A) a CTAB-capped AuNR on the glass slide substrate before the oxygen plasma treatment, and (B) removal of CTAB from the AuNR surface by oxygen plasma treatment 161

Figure 33. (A–I) SEM images of AuNRs after different oxygen plasma treatment times. Large structural deformation is observed at 180 s. In the *ex-situ* measurements, a new sample was used for each exposure time 162

Figure 34. (A, B) DF images of single AuNRs before and after 1800 s of oxygen plasma treatment, respectively. (C) Normalized DF spectra of two AuNRs (AuNR1 and AuNR2) highlighted by the yellow-edged squares in panels (A) and (B). The scattering spectra were fitted by the Lorentzian function to extract the homogeneous LSPR linewidth and LSPR wavelength 163

Figure 35. (A) LSPR linewidth of AuNRs versus plasma treatment time. Increasing the oxygen plasma treatment time for removing the CTAB capping material shortened the AuNRs, as shown in the schematic. The inset is an enlargement of the main plot in the range of 0–120 s 164

Figure S14. UV–Vis extinction spectrum of AuNRs (25 nm × 73 nm on average) showing two distinct transverse and longitudinal LSPR peaks 165

Figure S15. (A) Changes in the width (top) and length (bottom) of AuNRs as a

function of the plasma treatment time (0, 5, 10, 30, 60, 120, 180, 300, and 1800 s). **(B)** Corresponding change in aspect ratio (AR) of AuNRs 166

Figure S16. Changes in the LSPR wavelength of AuNRs as a function of the plasma treatment time (0, 5, 10, 30, 60, 120, 180, 300, and 1800 s) 167

Figure 36. Schematics of Structural changes during mercury amalgamation of **(A)** Bare AuNR and **(B)** AuNR@mSiO₂ 182

Figure 37. **(A)** Structure characterization of AuNRs@mSiO₂ and **(B)** after Hg amalgamation of AuNR@mSiO₂ **(C)** Enlarged SEM image and corresponding of Au **(D)** and Hg **(E)** elemental maps of Hg-AuNR@mSiO₂. Au and Hg elements were homogeneously distributed in the whole AuNR core 183

Figure 38. **(A)** TEM image analysis of the sizes (length and diameter) of bare AuNRs and **(B)** AuNRs@mSiO₂ 184

Figure 39. **(A)** DF scattering images of Bare AuNRs **(B)**, AuNRs@mSiO₂. **(C)** The overlaid DF scattering spectra of AuNRs before and after amalgamation, **(D)** and AuNR@mSiO₂ **(E)** average FWHM and **(F)** LSPR wavelength based on cumstun MATLAB script 185

Figure 40. **(A)** Real time monitoring of the blue shift of LSPR wavelength and **(B)** FWHM of AuNR and AuNR@mSiO₂ due to mercury amalgamation 186

Figure S17. **(A)** Structure characterization of AuNRs and **(B)** after Hg amalgamation of AuNRs **(C)** Enlarged SEM image and corresponding of Au **(D)** and Hg **(E)** elemental maps of Hg-AuNR. Au and Hg elements were homogeneously distributed in the whole AuNR 187

Chapter 1. General Introduction

Objectives and Scope of This Works

This dissertation consisted of a general introduction (Chapter 1) and followed 5 Chapters presented as 7 scientific manuscripts including introduction, experimental section, results and discussion, cited literature, and figures.

Chapter 2 reports a wavelength- and polarization-dependence of multiple branched gold nanoparticles that can be used as orientation sensors for single particle orientation tracking. Through this result, we can obtain background knowledge for the development of multispectral orientation probes.

Chapter 3 describes the high-throughput characterization of three-dimensional (3D) orientation of anisotropic gold nanorods (AuNRs) core in mesoporous silica shell(mSiO₂). Differential interference contrast (DIC) polarization anisotropy and dark-field (DF) defocused orientation imaging were used for tracking the rotational motions during a fast dynamic process. In addition, in situ variations of the tilting angles of the core AuNRs are achieved by inducing the movement of the spherical shell AuNRs@mSiO₂ through applying an external fluidic force in a flow cell. Finally, we demonstrate the use of AuNRs@mSiO₂ as multifunctional orientation probes in dynamic biological environments.

Chapter 4 describes the single particle study on structural and spectral changes of gold nanoparticles (AuNPs) as a result of physical or chemical reactions. We confirmed the structural and spectral changes caused by oxygen plasma treatment and

Hg amalgamation of single AuNR. Furthermore, in-situ monitoring of single AuNRs was carried out for a better understanding of the plasmonic damping process.

1.1 Localized Surface Plasmon Resonance Effect

Localized surface plasmon resonance (LSPR), defining the collective oscillations of free electrons in the conduction band of plasmonic gold nanoparticles (AuNPs) (**Fig. 1**), has gained considerable interest for its unique optical properties. Moreover, plasmonic gold nanoparticles (AuNPs) have the advantages of high chemical and photostability, excellent biocompatibility, and easy surface modification or functionalization with biomolecules. Thus, AuNPs have been widely studied in various areas such as LSPR sensing^{1, 2}, bioimaging³, surface-enhanced Raman spectroscopy⁴, plasmon enhanced fluorescence⁵, energy harvesting⁶, catalysis⁷, and biomedical therapies⁸.

In previous studies, Plasmonic AuNPs were primarily investigated at the ensemble level, which provides only the averaged spectral information of individual AuNPs with inherent sample inhomogeneity. This limitation of ensemble averaging can be overcome by advanced experimental and simulation techniques. Single particle spectroscopy has emerged as an invaluable tool to investigate plasmonic AuNPs of various shape and size. Single particle spectroscopy combined with electromagnetic calculations can further enhance our insight into the optical properties of AuNPs (**Fig. 2**).

Anisotropic AuNPs such as Au nanorods (AuNRs)⁹, Au nanobipyramids¹⁰, Au

nanourchins (AuNUs)¹¹, Au nanostars (AuNSs)¹², and Au nanoplates¹³ have been extensively investigated because of their signature optical properties induced by anisotropic shape. Particularly, the AuNRs, the typical anisotropic AuNPs, have attracted much interest as orientation probes because of their anisotropic shape-induced optical properties. The AuNRs have two geometrically confined LSPR wavelengths along the longitudinal and transverse axes.¹⁴ The excited single dipole of the surface plasmon bands enables AuNRs to be applied as orientation sensors similar to fluorescent dye.^{14, 15}

1.2 Optical Imaging Technique

A key factor for single particle spectroscopy is how to prepare isolated nanoparticles for detecting the individual nanoparticles with sufficient signal. Background free optical signal is desirable because there are excess background materials in the sample matrix compared with single nanoparticles. Because shorter wavelength emission than the fluorescence can be selectively removed with a relevant filter, Molecular fluorescence is suitable for single particle study. Recently Emission from plasmonic nanoparticles has been reported to be an excellent optical signal for single particle spectroscopy.¹⁶ The experimental setup used for single-particle microscopy and spectroscopy is presented in **Fig. 3**

Scattering-based dark-field (DF) microscopy is the most commonly used optical imaging technique to detect single AuNPs.^{15, 17} Remarkably, AuNPs are strong scatterers and absorbers from visible light to the near-infrared region because of the

LSPR effect.¹⁸ However, this optical imaging technique can only image large nanoparticles more significant than 20 nm in diameter because the scattering cross-sections of AuNPs decrease with the sixth power of the radius (R) of a nanoparticle.¹⁹ Recently, Absorption-based methods were developed to overcome the drawback of scattering-based methods.^{14, 20, 21} In this method, a single AuNP with 5 nm in diameter was detected by using a photothermal effect with a high signal-to-noise ratio. Besides, differential interference contrast (DIC) microscopy, an interferometric approach, can also be employed as a powerful method to visualize individual AuNPs down to 20 nm in diameter.²²

Richard Adolf Zsigmondy developed Scattering-based DF microscopy in 1923. The working principle of DF microscopy is shown in **Fig. 4**. the numerical aperture of the condenser is larger than that of the objective lens. An annular stop in the condenser blocks the central part of the illumination light beam coming from the microscope's lamp. On the microscope stage, when there is no sample that scatters the incident light, the entire field of view appears dark. However, when a sample is placed on the microscope stage, the objective lens only collects the scattered light. As a result, the sample image appears bright against the dark background in the DF microscopy. Although DF microscopy provides much higher signal-to-noise ratios than bright field microscopy it also has several disadvantages. For example, to obtain a higher signal, the sample needs to be illuminated by a strong light source, inducing potential photodamage. Furthermore, many biological components which can scatter illumination light limited the use of DF microscopy in a biological application.

DIC microscopy is another optical microscopy technique employed to visualize individual AuNPs. A working principle of DIC microscopy that adopts a more sophisticated scheme than BF and DF microscopies is shown in **Fig. 5**. In DIC microscopy, incident light from the lamp is passed through a first polarizer located beneath the condenser. The polarized light then goes through a first Nomarski prism, which splits the entering beam of light into two beams, each oscillating perpendicular to the other and so unable to recombine to generate interference. To prevent the double images, the shear distance between the two beams should be always kept less than the resolution of the objective lens. The paths of orthogonally split beams passing through the sample depend on the thicknesses, slopes, and refractive indices of the surrounding medium. When the orthogonal beams enter the objective lens, they are focused above the rear focal plane and recombine the two beams at the Normaski prism. In this step, the shear and the original path difference between the beam pairs are removed. However, the two orthogonal beams are no longer the same length because of pathway changes caused by the sample. In order for the orthogonal beams to interfere with each other, a second polarizer that brings the vibrations of the beams of different path lengths is placed. And then, the light proceeds to the eyepiece, where it can be observed as differences in intensity and color.

1.3 Single Particle Orientation Rotation Tracking

Single particle rotational tracking with optical probes has become very important to reveal specific mechanisms of biological processes that involve rotational

motion at the nanoscale, including myosin walking,²³ self-rotation of ATPase,²⁴ etc. Recently, plasmonic AuNRs have been widely utilized as orientation probes because of their anisotropic shape-induced optical properties,^{15, 25} and large scattering and absorption cross-sections resulting from LSPR effect,²⁶ high photostability (non-photobleaching and non-blinking), and excellent biocompatibility²⁷

Second, polarization-based optical techniques, including DF polarization microscopy,²⁶ photothermal heterodyne imaging (PHI),¹⁴ DIC polarization anisotropy,^{28, 29} and total internal reflection (TIR) scattering microscopy³⁰ have been used to determine the orientation of a AuNR. Furthermore, defocused orientation and position imaging (DOPI) techniques have been reported to allow determining the spatial orientation of out-of-focus AuNR without angular degeneracy.^{23, 31-33} However, with the current optical techniques, only the in-plane orientation is effectively revealed. In contrast, the accurate full three-dimension (3D) orientations of single AuNRs in the four quadrants of the Cartesian plane are only partially attainable. In this regard, further systematic fundamental studies that lead to the development of enhanced methods to characterize random 3D orientations of single AuNRs are still required in far-field optical microscopy. In this study, the polar angle θ and the azimuthal angle φ of a dipole generated on the Anisotropic AuNPs surface in 3D space are defined, as shown in **Fig. 6**

1.4 References

1. Willets, K. A.; Duyne, R. P. V., Localized Surface Plasmon Resonance Spectroscopy and Sensing. *Annual Review of Physical Chemistry* **2007**, *58* (1), 267-297.
2. Haes, A. J.; Hall, W. P.; Chang, L.; Klein, W. L.; Van Duyne, R. P., A Localized Surface Plasmon Resonance Biosensor: First Steps toward an Assay for Alzheimer's Disease. *Nano Letters* **2004**, *4* (6), 1029-1034.
3. Ma, Z.; Xia, H.; Liu, Y.; Liu, B.; Chen, W.; Zhao, Y., Applications of gold nanorods in biomedical imaging and related fields. *Chinese Science Bulletin* **2013**, *58* (21), 2530-2536.
4. He, S.; Chua, J.; Tan, E. K. M.; Kah, J. C. Y., Optimizing the SERS enhancement of a facile gold nanostar immobilized paper-based SERS substrate. *RSC Advances* **2017**, *7* (27), 16264-16272.
5. Shi, J.; Chan, C.; Pang, Y.; Ye, W.; Tian, F.; Lyu, J.; Zhang, Y.; Yang, M., A fluorescence resonance energy transfer (FRET) biosensor based on graphene quantum dots (GQDs) and gold nanoparticles (AuNPs) for the detection of mecA gene sequence of *Staphylococcus aureus*. *Biosensors and Bioelectronics* **2015**, *67*, 595-600.
6. Zhu, G.; Peng, B.; Chen, J.; Jing, Q.; Lin Wang, Z., Triboelectric nanogenerators as a new energy technology: From fundamentals, devices, to applications. *Nano Energy* **2015**, *14*, 126-138.
7. Sharma, G.; Kumar, A.; Sharma, S.; Naushad, M.; Prakash Dwivedi,

R.; Alothman, Z. A.; Mola, G. T., Novel development of nanoparticles to bimetallic nanoparticles and their composites: A review. *Journal of King Saud University - Science* **2019**, *31* (2), 257-269.

8. Ali, M. R. K.; Wu, Y.; El-Sayed, M. A., Gold-Nanoparticle-Assisted Plasmonic Photothermal Therapy Advances Toward Clinical Application. *The Journal of Physical Chemistry C* **2019**, *123* (25), 15375-15393.

9. Pérez-Juste, J.; Pastoriza-Santos, I.; Liz-Marzán, L. M.; Mulvaney, P., Gold nanorods: Synthesis, characterization and applications. *Coordination Chemistry Reviews* **2005**, *249* (17), 1870-1901.

10. Lee, S. Y.; Tsalu, P. V.; Kim, G. W.; Seo, M. J.; Hong, J. W.; Ha, J. W., Tuning Chemical Interface Damping: Interfacial Electronic Effects of Adsorbate Molecules and Sharp Tips of Single Gold Bipyramids. *Nano Letters* **2019**, *19* (4), 2568-2574.

11. Thapliyal, N. B.; Chiwunze, T. E.; Karpoormath, R.; Cherukupalli, S., Fabrication of highly sensitive gold nanourchins based electrochemical sensor for nanomolar determination of primaquine. *Materials Science and Engineering: C* **2017**, *74*, 27-35.

12. Senthil Kumar, P.; Pastoriza-Santos, I.; Rodríguez-González, B.; Javier García de Abajo, F.; Liz-Marzán, L. M., High-yield synthesis and optical response of gold nanostars. *Nanotechnology* **2007**, *19* (1), 015606.

13. Smith, K. W.; Yang, J.; Hernandez, T.; Swearer, D. F.; Scarabelli, L.; Zhang, H.; Zhao, H.; Moringo, N. A.; Chang, W.-S.; Liz-Marzán, L. M.;

Ringe, E.; Nordlander, P.; Link, S., Environmental Symmetry Breaking Promotes Plasmon Mode Splitting in Gold Nanotriangles. *The Journal of Physical Chemistry C* **2018**, *122* (25), 13259-13266.

14. Chang, W.-S.; Ha, J. W.; Slaughter, L. S.; Link, S., Plasmonic nanorod absorbers as orientation sensors. *Proceedings of the National Academy of Sciences* **2010**, *107* (7), 2781-2786.

15. Sönnichsen, C.; Alivisatos, A. P., Gold Nanorods as Novel Nonbleaching Plasmon-Based Orientation Sensors for Polarized Single-Particle Microscopy. *Nano Lett.* **2005**, *5* (2), 301.

16. Beversluis, M. R.; Bouhelier, A.; Novotny, L., Continuum generation from single gold nanostructures through near-field mediated intraband transitions. *Physical Review B* **2003**, *68* (11), 115433.

17. Hu, M.; Novo, C.; Funston, A.; Wang, H.; Staleva, H.; Zou, S.; Mulvaney, P.; Xia, Y.; Hartland, G. V., Dark-field microscopy studies of single metal nanoparticles: understanding the factors that influence the linewidth of the localized surface plasmon resonance. *Journal of Materials Chemistry* **2008**, *18* (17), 1949-1960.

18. Link, S.; Mohamed, M. B.; El-Sayed, M. A., Simulation of the Optical Absorption Spectra of Gold Nanorods as a Function of Their Aspect Ratio and the Effect of the Medium Dielectric Constant. *The Journal of Physical Chemistry B* **1999**, *103* (16), 3073-3077.

19. van Dijk, M. A.; Tchegotareva, A. L.; Orrit, M.; Lippitz, M.; Berciaud, S.; Lasne, D.; Cognet, L.; Lounis, B., Absorption and scattering microscopy of

single metal nanoparticles. *Physical Chemistry Chemical Physics* **2006**, *8* (30), 3486-3495.

20. Boyer, D.; Tamarat, P.; Maali, A.; Lounis, B.; Orrit, M., Photothermal imaging of nanometer-sized metal particles among scatterers. *Science* **2002**, *297* (5584), 1160-3.

21. Berciaud, S.; Lasne, D.; Blab, G. A.; Cognet, L.; Lounis, B., Photothermal heterodyne imaging of individual metallic nanoparticles: Theory versus experiment. *Physical Review B* **2006**, *73* (4), 045424.

22. Sun, W.; Wang, G.; Fang, N.; Yeung, E. S., Wavelength-Dependent Differential Interference Contrast Microscopy: Selectively Imaging Nanoparticle Probes in Live Cells. *Analytical Chemistry* **2009**, *81* (22), 9203-9208.

23. Toprak, E.; Enderlein, J.; Syed, S.; McKinney, S. A.; Petschek, R. G.; Ha, T.; Goldman, Y. E.; Selvin, P. R., Defocused orientation and position imaging (DOPI) of myosin V. *Proc. Natl. Acad. Sci. U. S. A.* **2006**, *103* (17), 6495.

24. Nishizaka, T.; Oiwa, K.; Noji, H.; Kimura, S.; Muneyuki, E.; Yoshida, M.; Kinosita, K., Chemomechanical coupling in F1-ATPase revealed by simultaneous observation of nucleotide kinetics and rotation. *Nature Structural & Molecular Biology* **2004**, *11* (2), 142-148.

25. Xiao, L.; Qiao, Y.; He, Y.; Yeung, E. S., Imaging Translational and Rotational Diffusion of Single Anisotropic Nanoparticles with Planar Illumination Microscopy. *Journal of the American Chemical Society* **2011**, *133* (27), 10638-10645.

26. Link, S.; El-Sayed, M. A., Spectral Properties and Relaxation Dynamics of

Surface Plasmon Electronic Oscillations in Gold and Silver Nanodots and Nanorods.

J. Phys. Chem. B **1999**, *103* (40), 8410.

27. Murphy, C. J.; Gole, A. M.; Stone, J. W.; Sisco, P. N.; Alkilany, A. M.; Goldsmith, E. C.; Baxter, S. C., Gold Nanoparticles in Biology: Beyond Toxicity to Cellular Imaging. *Accounts of Chemical Research* **2008**, *41* (12), 1721-1730.

28. Won Ha, J.; Sun, W.; Wang, G.; Fang, N., Differential interference contrast polarization anisotropy for tracking rotational dynamics of gold nanorods. *Chemical Communications* **2011**, *47* (27), 7743-7745.

29. Ha, J. W.; Sun, W.; Stender, A. S.; Fang, N., Dual-Wavelength Detection of Rotational Diffusion of Single Anisotropic Nanocarriers on Live Cell Membranes. *The Journal of Physical Chemistry C* **2012**, *116* (4), 2766-2771.

30. Marchuk, K.; Ha, J. W.; Fang, N., Three-Dimensional High-Resolution Rotational Tracking with Superlocalization Reveals Conformations of Surface-Bound Anisotropic Nanoparticles. *Nano Letters* **2013**, *13* (3), 1245-1250.

31. Xiao, L.; Qiao, Y.; He, Y.; Yeung, E. S., Three Dimensional Orientational Imaging of Nanoparticles with Darkfield Microscopy. *Anal. Chem.* **2010**, *82* (12), 5268.

32. Ha, J. W., Characteristic image patterns of single anisotropic plasmonic nanoparticles embedded in a gel matrix. *Nanoscale* **2015**, *7* (31), 13159.

33. Li, T.; Li, Q.; Xu, Y.; Chen, X.-J.; Dai, Q.-F.; Liu, H.; Lan, S.; Tie, S.; Wu, L.-J., Three-Dimensional Orientation Sensors by Defocused Imaging of Gold Nanorods through an Ordinary Wide-Field Microscope. *ACS Nano* **2012**, *6* (2), 1268-1277.

1.5 Figures and Captions

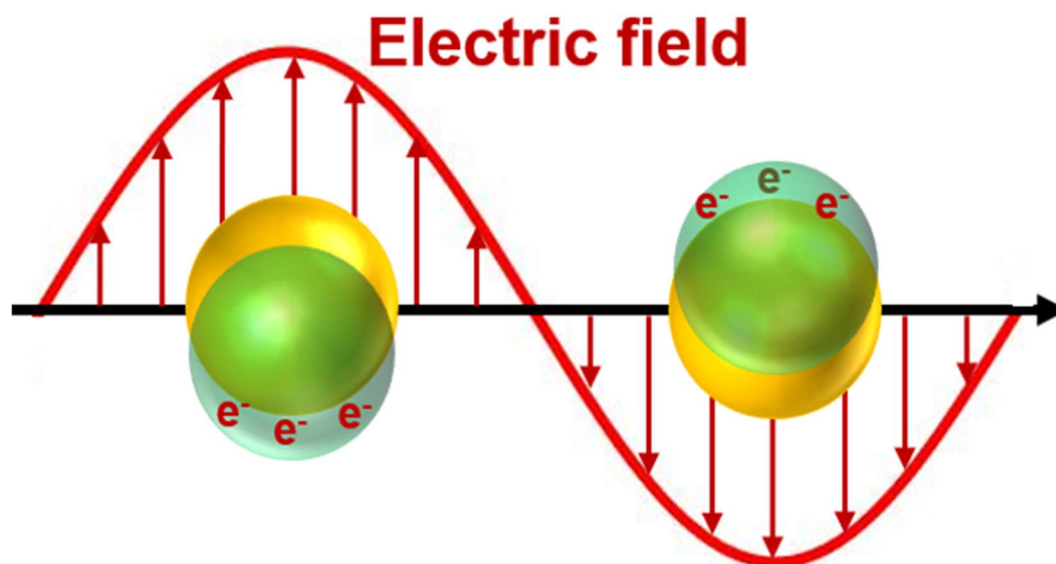


Figure 1. Schematic image of localized surface plasmon resonance.

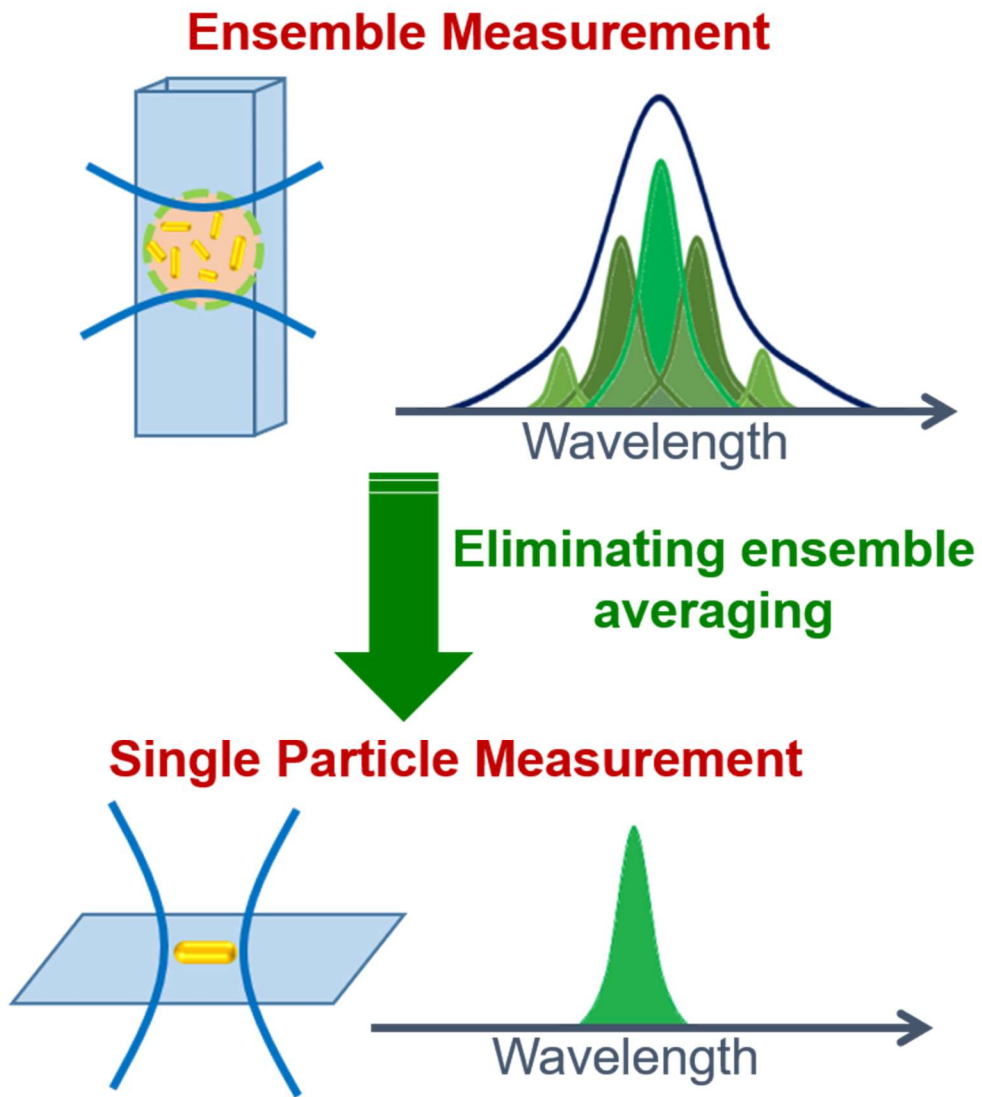


Figure 2. Scheme of advantage of single particle measurement.

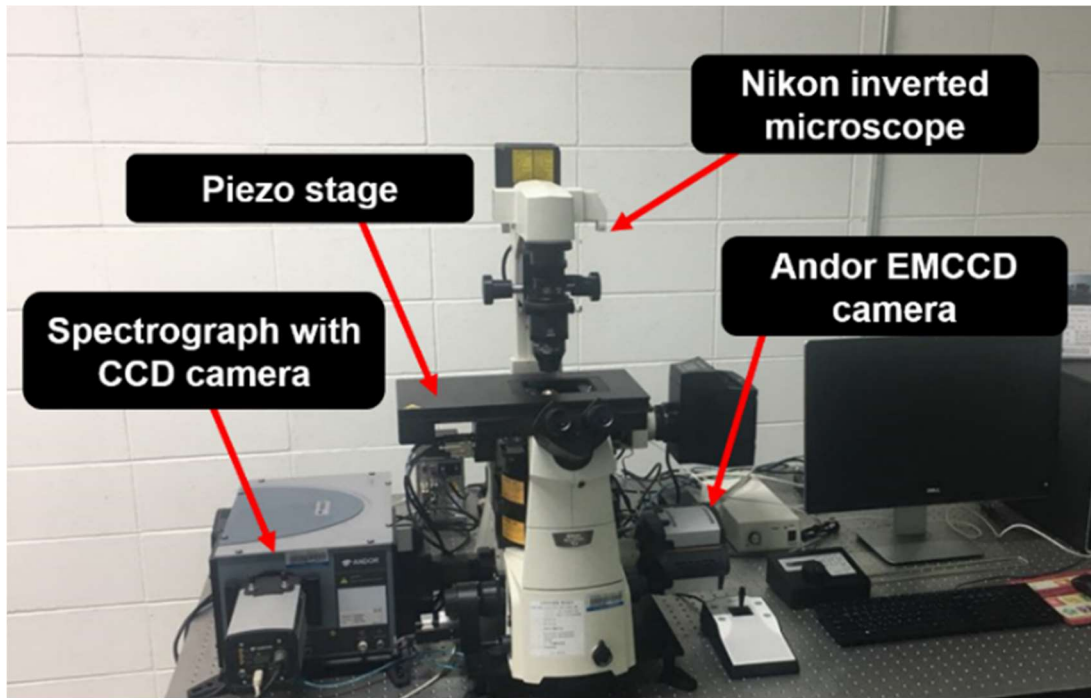


Figure 3. Photograph to show the experimental setup for single particle spectroscopy.

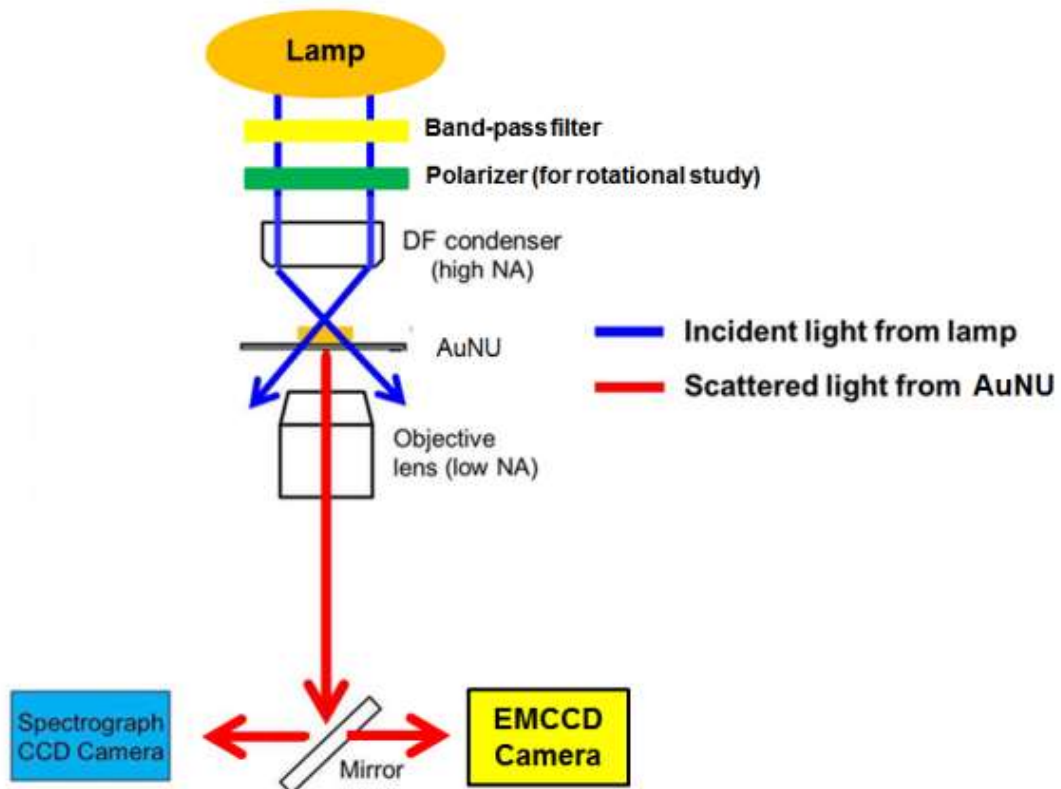


Figure 4. The working principle of dark-field (DF) microscopy and spectroscopy.

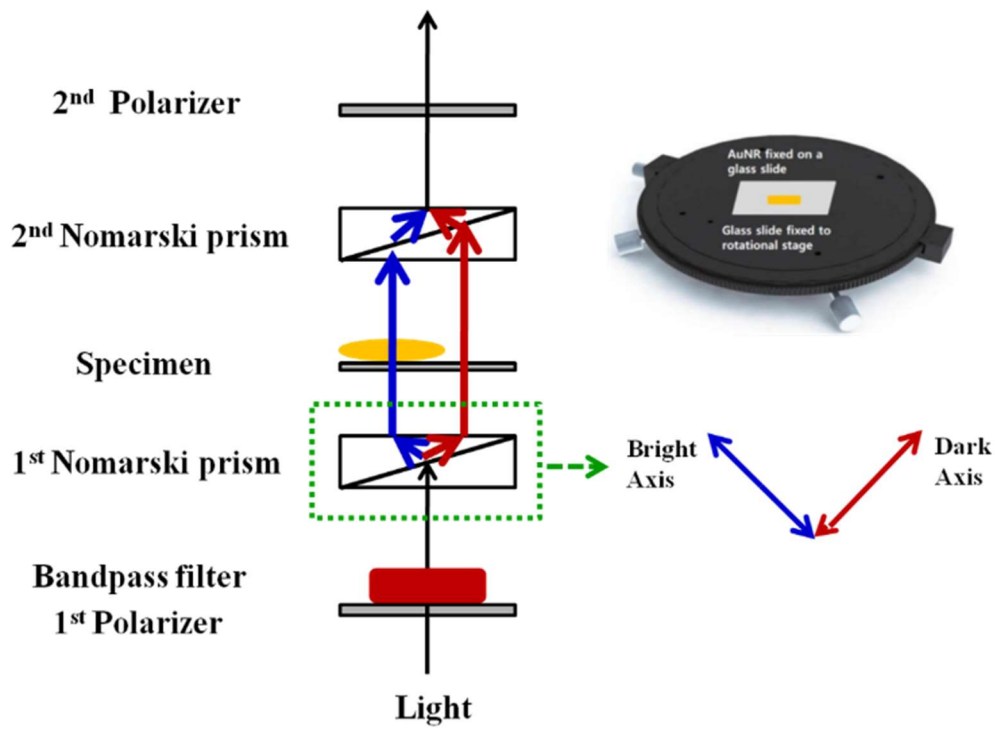


Figure 5. The working principle of DIC microscopy. The incident light is split into two orthogonally linearly polarized beams by the first Nomarski prism. Two beams pass through the sample and are recombined by the second Nomarski prism to create an interference pattern.

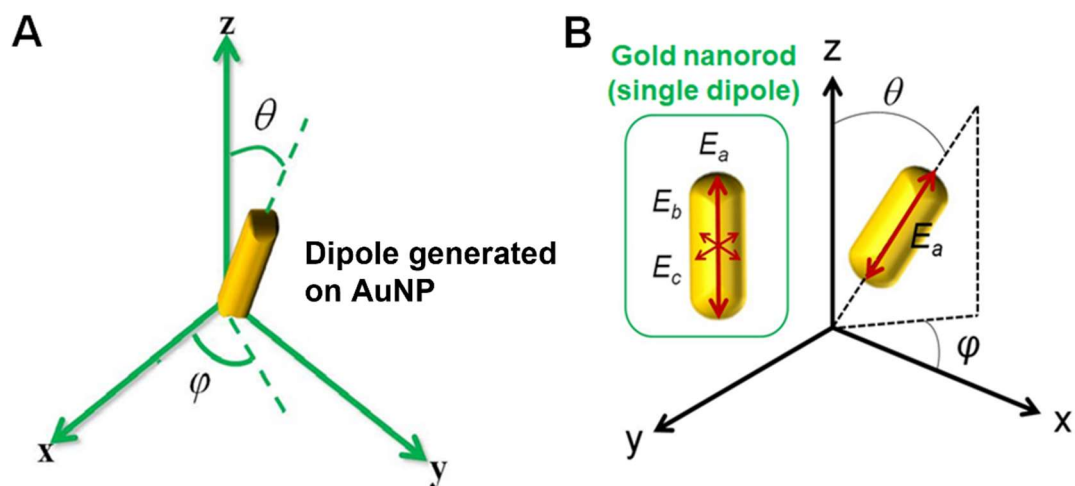


Figure 6. (A) Schematic diagram to show the definitions of the polar angle θ and azimuthal angle φ of single dipole generated on the AuNP surface in 3D space. (B) Schematic diagram depicting three-perpendicular dipoles along the three axes. E_a denotes the scattering electric field of the nanorod along the main long axis.

Chapter 2. Wavelength- and Polarization-Dependence of Multiple Branch Gold Nanoparticle

2.1 Direct Visualization of Wavelength-Dependent Single Dipoles Generated on Single Gold Nanourchins with Sharp Branches

Geun Wan Kim and Ji Won Ha*

A paper published in *Nanoscale Research Letters*, **2018**, 13, 256.

Reproduced by permission of the Springer nature

*Corresponding author

2.1.1 Abstract

We present the optical properties of single gold nanourchins (AuNUs) with sharp branches on their surfaces under dark-field (DF) microscopy and spectroscopy. The DF intensities of the single AuNUs were changed periodically as a function of the rotation angle at three localized surface plasmon resonance (LSPR) wavelengths. Furthermore, we demonstrate the generation of single dipoles with different LSPR wavelengths in multiple directions on the same AuNU surface. The multiple LSPR dipoles generated on the AuNU surface were further visualized under defocused DF microscopy and verified by characteristic doughnut-shaped defocused scattering field distributions.

2.1.2 Introduction

In recent years, plasmonic gold nanoparticles with unique optical properties have been widely employed as optical sensors,¹ active surface-enhanced Raman scattering (SERS) substrates,²⁻⁷ biological and chemical sensors,⁸⁻¹⁰ and near-infrared absorbers for photothermal therapy.^{11, 12} The unique size- and shape-dependent optical properties of gold nanoparticles are caused by the localized surface plasmon resonance (LSPR), which is a collective oscillation of conduction electrons on their surface with the incident light^{13, 14} Furthermore, their optical property is also dependent on the refractive index of surrounding medium.^{15, 16} In particular, gold nanoparticles with multiple sharp branches are highly sensitive to changes in the dielectric constant compared to simple gold nanospheres.^{8, 17} In addition, Au nanoparticles with uneven surfaces and sharp tips exhibit strong enhancement of an electromagnetic field as described by both experimental measurements and theoretical calculations.^{3, 18-26}

With the recent development of synthesis techniques of gold nanoparticles,²⁷ it became possible to achieve the controlled synthesis of a range of shapes of gold nanoparticles in high yield. For example, anisotropic gold nanoparticles, such as nanourchins, nanostars,^{3, 8, 12, 19} nanorods,²⁸⁻³⁰ nanoplates,³¹ and bipyramids³² have been synthesized and investigated on a range of applications. In particular, branched gold nanoparticles have been widely used in SERS^{33, 34} and LSPR biosensors^{8, 17} because of the generation of strong hot spots in the sharp branches. To date, there have been many studies to understand the optical properties of single gold nanoparticles with sharp branches. Furthermore, theoretical calculation and experimental

measurements have been used to gain a deeper insight into their size- and shape-dependent optical properties.^{17, 33, 35, 36} For instance, confocal Raman imaging was employed to reveal the spatial distribution of hot spots produced in micrometer-scale single silver nanoflowers.³⁷ The angular distribution of a SERS imaging pattern depending on the incident wavelength has also been utilized for characterizing the particle dimers from aggregates.³⁸ Despite the recent studies on branched gold nanoparticles, their optical properties are not completely revealed and understood.

Very recently, to better understand the scattering properties of single gold nanourchins (AuNUs) with sharp and short branches, the polarization-dependent dark-field (DF) scattering properties of single AuNUs were investigated at their LSPR wavelength of 700 nm.³⁹ Single dipoles in multiple directions were found to be generated on the Au nanourchin surface at the LSPR wavelength of 700 nm. However, the effects of the incident wavelength on the change in the scattering intensity of a single AuNU have remained unanswered. In this respect, it is necessary to have a better understanding of their optical properties at the single particle level and to obtain a deeper insight into the wavelength- and polarization-dependent properties of single branched AuNUs. Furthermore, it is required to verify the generation of single dipole modes at multiple wavelengths in single AuNUs and their wavelength- and polarization-dependence on the same AuNU surface. In the present study, we characterized the wavelength- and polarization-dependent scattering properties of single AuNUs at three different LSPR wavelengths under single-particle DF microscopy and spectroscopy. A rotational study enabled us to find polarization-

dependent optical properties of the 90-nm single AuNUs at their LSPR wavelengths. Furthermore, the phase of a DF intensity trace was changed according to the incident wavelengths, which supports the generation of single dipoles with multiple LSPR wavelengths on the surface of a single AuNU with sharp tips. The generation of multiple LSPR dipoles was further visualized and verified by defocused scattering image patterns of single AuNU at the LSPR wavelengths.

2.1.3 Experimental Section

Materials and Sample Preparation

AuNUs with an average diameter of 90 nm were obtained from Sigma-Aldrich (St. Louis, MO, USA). The AuNU colloid solution was first diluted with 18.2-M Ω pure water to the appropriate concentration. The diluted solution was then sonicated for 15 min at room temperature. The samples were prepared by spin-casting an AuNU solution onto a pre-cleaned glass slide. Subsequently, a 22 mm \times 22 mm no. 1.5 coverslip (Corning, NY) was placed on the glass slide. In this study, the concentration of AuNUs on the glass surface was controlled to approximately 1 μm^{-2} to facilitate single-particle characterization and to minimize interparticle LSPR coupling, which can result in a spectral shift.

Characterization

Structural characterizations of citrate-stabilized AuURs were carried out using a transmission electron microscope (TEM) (H-8100, Hitachi, Japan) and a scanning

electron microscope (SEM) (JSM6500F, JEOL, Japan). Furthermore, the heterogeneous LSPR ensemble absorption spectrum of AuNUs dispersed in water was recorded with a Varian Carry 300 UV-Vis spectrometer.

Scattering-Based Dark-Field Microscopy

DF microscopy imaging was performed under a Nikon inverted microscope (ECLIPSE Ti-U). In DF mode, the microscope utilized a Nikon Plan Fluor 100×0.5 –1.3 oil iris objective and a Nikon DF condenser. An Andor iXonEM+ CCD camera (iXon Ultra 897) was used to record the DF images of the AuNUs. In this study, wavelength- and polarization-dependent DF scattering imaging of single AuNUs was carried out by linearly polarizing the excitation beam and changing the polarization in 10° increments. A polarizer was placed in the beam path to measure the polarization dependence of scattered light. The wavelength-dependent single particle DF studies were carried out by using the bandpass filters with a central range of 600 nm (full width at half-maximum, ± 14 nm), 640 nm (full width at half-maximum, ± 14 nm), and 700 nm (full width at half-maximum, ± 13 nm). The bandpass filters were obtained from Thorlabs (Newton, NJ) and inserted into the beam path of the microscope to illuminate the samples. A rotational study was carried out for single AuNUs at three excitation wavelengths by rotating the rotational stage at 10° intervals. As the stage was rotated, the fixed AuNUs were positioned at different orientations. An Andor iXonEM+ CCD camera (iXon Ultra 897) was used to record highly detailed DF scattering images of AuNUs. The collected images were analyzed using ImageJ.

Single Particle Scattering Spectroscopy

DF scattering spectra were acquired with an Andor spectrophotometer (SHAMROCK 303i, SR-303I-A) connected with an Andor CCD camera (Newton DU920P-OE). When obtaining a spectrum, the scanning stage moved the sample to the desired location so that only scattered light from the selected location was collected by the objective. The scattered light was directed to the entrance of the spectrophotometer, dispersed by a grating (300 l/mm), and detected by the Newton CCD camera. The background was measured at a region without any particles. Data analysis was performed with specially designed MATLAB programs.

2.1.4 Result and Discussion

The structures of the 90 nm AuNUs were initially characterized by scanning electron microscopy (SEM). The AuNUs have a diameter of 90 nm with short branches. The three-dimensional (3D) structure of the AuNUs with sharp branches was observed clearly in the SEM image (**Fig. 7A**). As shown in **Fig. 7A**, the AuNUs have uneven and spiky surfaces because of the multiple short and sharp branches on their surface. The UV-Vis absorption spectra of AuNUs dispersed in water was then obtained (**Fig. 7B**). As shown in **Fig. 7B**, the 90 nm AuNUs showed a single broad LSPR peak at approximately 634 nm.

To better understand the scattering properties of AuNUs, we performed single-particle measurements under DF microscopy and spectroscopy, which allowed us to

eliminate the ensemble averaging. A sample was prepared by spin casting a solution containing AuNUs on a pre-cleaned glass slide. In this study, we used a glass slide as a substrate because the optical properties of AuNUs are strongly dependent on the dielectric constant of substrate. The AuNUs were then measured by illuminating them with randomly polarized white light focused tightly by a high-numerical aperture (NA) oil condenser under DF microscopy. Fig. 8A shows a DF scattering image of the 90 nm AuNUs deposited on a glass slide. The single particle scattering spectra of the AuNUs were obtained, as highlighted by squares in **Fig. 8A**. **Fig. 8B** shows a single particle total scattering spectrum of AuNU1 in **Fig. 8A**. A single LSPR peak was observed at ~ 650 nm for AuNU1, which is consistent with the results obtained by the ensemble experiment in **Fig. 7B**

In a recent study, the polarization-dependent DF scattering intensities of single AuNUs were observed at the LSPR wavelength of 700 nm.³⁹ Furthermore, the single AuNUs with sharp and short branches could generate single dipoles in multiple directions on the nanourchin surface at 700 nm. On the other hand, the wavelength-dependent DF scattering intensities of single AuNUs were not investigated and largely unanswered. Therefore, in this paper, we made efforts to gain deeper insight into the wavelength- and polarization-dependent scattering properties of single AuNUs with spiky and uneven surfaces. As shown in the yellow-dotted lines in Fig. 2b, three different LSPR incident wavelengths of 600 nm, 640 nm, and 700 nm were chosen and used to measure single AuNUs.

A rotational study was carried out for single 90 nm AuNUs at the three

excitation wavelengths by rotating a polarizer at intervals of 10° . A polarizer and three bandpass filters were placed on the path of light to elucidate the polarization- and wavelength-dependent scattering properties of single AuNUs. **Fig. 9A** presents the changes in the normalized scattering intensities of AuNU1 at the three different wavelengths (600 nm, 640 nm, and 700 nm) as a function of the rotational angle. The periodically changed DF scattering intensity was found according to the rotation angle for the three different LSPR wavelengths. On the other hand, slight fluctuations (up and down) of the DF intensities were observed, which clearly differs from the periodic changes in the DF intensities of a single gold nanorod (AuNR), behaving as a single dipole. These fluctuations can be explained by the spatial distributions of sharp and short branches.

In addition to the polarization dependence, it should be noted that AuNU1 had a different phase of DF scattering intensities depending on the excitation LSPR wavelengths, as shown in **Fig. 9A**. The results support the generation of single dipoles with different LSPR wavelengths produced in multiple directions on the same AuNU1 with short branches (**Fig. 9B, C**). To further support the generation of single dipoles in multiple directions on the AuNU surface, we attempted to measure single AuNUs under defocused DF scattering microscopy. Defocused orientation and position imaging (DOPI) technique is a direct and simple method with the capability of visualizing and determining three-dimensional (3D) dipole orientation of anisotropic single gold nanorods (AuNRs).⁴⁰⁻⁴² The core idea is that the direct detection of the spatial distribution of the scattered or emitted field of single dipoles becomes possible

when the imaging system is defocused deliberately by $\sim 1 \mu\text{m}$. In this study, the polar angle θ and the azimuthal angle φ of a dipole generated on the AuNU surface in 3D space are defined, as shown in **Fig. 6A** (please see the supplementary materials for more details in the DOPI technique). Therefore, it is possible to resolve the 3D orientation of single dipoles generated on the AuNU surface by characterizing the characteristic scattering intensity distributions.

We therefore tested if the spatial scattering field distribution of single AuNUs can be resolved directly from their defocused scattering image patterns. The AuNUs were measured at their LSPR wavelengths under defocused DF scattering microscopy. When the AuNU1 was measured at the LSPR wavelengths (600 nm and 700 nm) and positioned at $\sim 1 \mu\text{m}$ away from the focal plane, characteristic doughnut-shaped scattering patterns were observed with two lobes in the peripheral area (**Fig. 10A, B**). Furthermore, the spatial intensity distribution on the CCD camera was no longer circularly symmetrical because single dipoles generated on the AuNU surface were tilted with the respect to a glass surface. We then tried to obtain detailed information on the 3D orientation of single dipoles generated on the surface of AuNU1 (**Fig. 10A, B**). The in-plane orientation angle φ can be extracted readily from the lobe scattering pattern exhibiting angular anisotropy as seen in the white-dotted line in (**Fig. 10A, B**), which is consistent with the result to show the phase difference of $\sim 90^\circ$ in **Fig. 9A**. The out-of-plane polar angle θ was estimated using the program developed by Enderlein and Böhmer for simulating the characteristic intensity distribution from an emitter with three perpendicular emission dipoles of different emission strengths. The

3D orientation of single dipoles on a glass substrate can be estimated by referring to their corresponding field map and the best-fit simulated scattering pattern. **Fig 10C, D** shows the best-fit simulated patterns at the two LSPR wavelengths of 600 nm and 700 nm. The polar angles of the generated dipoles on the AuNU1 at 600 nm and 700 nm were estimated to be about 75° and 73° , respectively. Therefore, we successfully visualized the single dipoles generated in multiple directions with different LSPR wavelengths on the same AuNU surface under defocused DF microscopy.

Last, the DF scattering intensities of single AuNUs measured at the same excitation wavelength were then compared, as shown in **Fig. 8A**. **Fig 11A** shows the DF scattering intensities of three AuNUs (AuNU2 to AuNU4) at an excitation wavelength of 640 nm. Each AuNU has a different phase as a function of the rotational angle, which indicates a different dipole orientation at 640 nm on the particle surface for the three AuNUs (AuNU2 to AuNU4). The experimental results were observed at the LSPR wavelength of 700 nm for the same AuNUs (**Fig. 11B**). Therefore, this paper provides a deeper understanding of the wavelength- and polarization-sensitive optical properties of short and sharp branches on the AuNU surface under focused and defocused DF microscopy at the single particle level.

2.1.5 Conclusion

The optical properties of single AuNUs with sharp and short tips on their surfaces were examined by DF microscopy and spectroscopy. The DF intensities of

single AuNUs were investigated with linearly polarized light at three different LSPR wavelengths, 600 nm, 640 nm, and 700 nm, as a function of the rotation angle. The DF intensities were changed as a function of the rotational angle at three different wavelengths. More interestingly, the phase of a DF intensity trace differed according to the incident wavelengths, which can be attributed to the generation of single dipoles with different LSPR wavelengths in multiple directions on the same AuNU surface. Furthermore, we directly visualized single dipoles generated in multiple directions at the different incident wavelengths on the same AuNU surface under defocused DF microscopy. Therefore, this paper offers a deeper insight into the scattering properties of highly branched AuNUs under focused and defocused DF microscopy at the single particle level. Moreover, the knowledge gained from this study will be beneficial for various uses of branched AuNUs in SERS, LSPR biosensors, optical imaging probes, etc.

2.1.6 References

1. Jiang, Y.; Wu, X.-J.; Li, Q.; Li, J.; Xu, D., Facile synthesis of gold nanoflowers with high surface-enhanced Raman scattering activity. *Nanotechnology* **2011**, *22* (38), 385601.
2. Wang, H.; Halas, N. J., Mesoscopic Au “Meatball” Particles. *Advanced Materials* **2008**, *20* (4), 820-825.
3. He, S.; Chua, J.; Tan, E. K. M.; Kah, J. C. Y., Optimizing the SERS enhancement of a facile gold nanostar immobilized paper-based SERS substrate. *RSC Advances* **2017**, *7* (27), 16264-16272.
4. Xie, J.; Zhang, Q.; Lee, J. Y.; Wang, D. I. C., The Synthesis of SERS-Active Gold Nanoflower Tags for In Vivo Applications. *ACS Nano* **2008**, *2* (12), 2473-2480.
5. Chirumamilla, M.; Gopalakrishnan, A.; Toma, A.; Proietti Zaccaria, R.; Krahne, R., Plasmon resonance tuning in metal nanostars for surface enhanced Raman scattering. *Nanotechnology* **2014**, *25* (23), 235303.
6. Jimenez de Aberasturi, D.; Serrano-Montes, A. B.; Langer, J.; Henriksen-Lacey, M.; Parak, W. J.; Liz-Marzán, L. M., Surface Enhanced Raman Scattering Encoded Gold Nanostars for Multiplexed Cell Discrimination. *Chemistry of Materials* **2016**, *28* (18), 6779-6790.
7. Lu, G.; Forbes, T. Z.; Haes, A. J., SERS detection of uranyl using functionalized gold nanostars promoted by nanoparticle shape and size. *Analyst* **2016**, *141* (17), 5137-5143.

8. Dondapati, S. K.; Sau, T. K.; Hrelescu, C.; Klar, T. A.; Stefani, F. D.; Feldmann, J., Label-free Biosensing Based on Single Gold Nanostars as Plasmonic Transducers. *ACS Nano* **2010**, *4* (11), 6318-6322.
9. Wang, W.; Cui, H., Chitosan-Luminol Reduced Gold Nanoflowers: From One-Pot Synthesis to Morphology-Dependent SPR and Chemiluminescence Sensing. *The Journal of Physical Chemistry C* **2008**, *112* (29), 10759-10766.
10. Thapliyal, N. B.; Chiwunze, T. E.; Karpoormath, R.; Cherukupalli, S., Fabrication of highly sensitive gold nanourchins based electrochemical sensor for nanomolar determination of primaquine. *Materials Science and Engineering: C* **2017**, *74*, 27-35.
11. Park, J.; Estrada, A.; Sharp, K.; Sang, K.; Schwartz, J. A.; Smith, D. K.; Coleman, C.; Payne, J. D.; Korgel, B. A.; Dunn, A. K.; Tunnell, J. W., Two-photon-induced photoluminescence imaging of tumors using near-infrared excited gold nanoshells. *Opt. Express* **2008**, *16* (3), 1590-1599.
12. Chen, H.; Zhang, X.; Dai, S.; Ma, Y.; Cui, S.; Achilefu, S.; Gu, Y., Multifunctional Gold Nanostar Conjugates for Tumor Imaging and Combined Photothermal and Chemo-therapy. *Theranostics* **2013**, *3* (9), 633-649.
13. Schuller, J. A.; Barnard, E. S.; Cai, W.; Jun, Y. C.; White, J. S.; Brongersma, M. L., Plasmonics for extreme light concentration and manipulation. *Nature Materials* **2010**, *9* (3), 193-204.
14. Novotny, L.; van Hulst, N., Antennas for light. *Nature Photonics* **2011**, *5* (2), 83-90.

15. Link, S.; El-Sayed, M. A., Spectral Properties and Relaxation Dynamics of Surface Plasmon Electronic Oscillations in Gold and Silver Nanodots and Nanorods. *The Journal of Physical Chemistry B* **1999**, *103* (40), 8410-8426.
16. and, S. L.; El-Sayed, M. A., Optical Properties and Ultrafast Dynamics of Metallic Nanocrystals. *Annual Review of Physical Chemistry* **2003**, *54* (1), 331-366.
17. Nehl, C. L.; Liao, H.; Hafner, J. H., Optical Properties of Star-Shaped Gold Nanoparticles. *Nano Letters* **2006**, *6* (4), 683-688.
18. Hao, E.; Bailey, R. C.; Schatz, G. C.; Hupp, J. T.; Li, S., Synthesis and Optical Properties of “Branched” Gold Nanocrystals. *Nano Letters* **2004**, *4* (2), 327-330.
19. Senthil Kumar, P.; Pastoriza-Santos, I.; Rodríguez-González, B.; Javier García de Abajo, F.; Liz-Marzán, L. M., High-yield synthesis and optical response of gold nanostars. *Nanotechnology* **2007**, *19* (1), 015606.
20. Heo, K. C.; Gwag, J. S., Shape-modification of patterned nanoparticles by an ion beam treatment. *Scientific Reports* **2015**, *5* (1), 8523.
21. Chiu, N.-F.; Chen, C.-C.; Yang, C.-D.; Kao, Y.-S.; Wu, W.-R., Enhanced Plasmonic Biosensors of Hybrid Gold Nanoparticle-Graphene Oxide-Based Label-Free Immunoassay. *Nanoscale Research Letters* **2018**, *13* (1), 152.
22. Wu, J.; Yu, P.; Susha, A. S.; Sablon, K. A.; Chen, H.; Zhou, Z.; Li, H.; Ji, H.; Niu, X.; Govorov, A. O.; Rogach, A. L.; Wang, Z. M., Broadband efficiency enhancement in quantum dot solar cells coupled with multispiked plasmonic nanostars. *Nano Energy* **2015**, *13*, 827-835.

23. Yu, P.; Zhang, F.; Li, Z.; Zhong, Z.; Govorov, A.; Fu, L.; Tan, H.; Jagadish, C.; Wang, Z., Giant optical pathlength enhancement in plasmonic thin film solar cells using core-shell nanoparticles. *Journal of Physics D: Applied Physics* **2018**, *51* (29), 295106.
24. Wang, W.; Yu, P.; Zhong, Z.; Tong, X.; Liu, T.; Li, Y.; Ashalley, E.; Chen, H.; Wu, J.; Wang, Z., Size-dependent longitudinal plasmon resonance wavelength and extraordinary scattering properties of Au nanobipyramids. *Nanotechnology* **2018**, *29* (35), 355402.
25. Wu, C.; Tong, X.; Ai, Y.; Liu, D.-S.; Yu, P.; Wu, J.; Wang, Z. M., A Review: Enhanced Anodes of Li/Na-Ion Batteries Based on Yolk–Shell Structured Nanomaterials. *Nano-Micro Letters* **2018**, *10* (3), 40.
26. Wang, J.; Jia, S.; Cao, Y.; Wang, W.; Yu, P., Design Principles for Nanoparticle Plasmon-Enhanced Organic Solar Cells. *Nanoscale Research Letters* **2018**, *13* (1), 211.
27. Grzelczak, M.; Pérez-Juste, J.; Mulvaney, P.; Liz-Marzán, L. M., Shape control in gold nanoparticle synthesis. *Chemical Society Reviews* **2008**, *37* (9), 1783-1791.
28. Won Ha, J.; Sun, W.; Wang, G.; Fang, N., Differential interference contrast polarization anisotropy for tracking rotational dynamics of gold nanorods. *Chemical Communications* **2011**, *47* (27), 7743-7745.
29. Tcherniak, A.; Dominguez-Medina, S.; Chang, W.-S.; Swanglap, P.; Slaughter, L. S.; Landes, C. F.; Link, S., One-Photon Plasmon Luminescence and Its

Application to Correlation Spectroscopy as a Probe for Rotational and Translational Dynamics of Gold Nanorods. *The Journal of Physical Chemistry C* **2011**, *115* (32), 15938-15949.

30. Cao, J.; Galbraith, E. K.; Sun, T.; Grattan, K. T. V., Cross-Comparison of Surface Plasmon Resonance-Based Optical Fiber Sensors With Different Coating Structures. *IEEE Sensors Journal* **2012**, *12* (7), 2355-2361.

31. Smith, K. W.; Yang, J.; Hernandez, T.; Swearer, D. F.; Scarabelli, L.; Zhang, H.; Zhao, H.; Moringo, N. A.; Chang, W.-S.; Liz-Marzán, L. M.; Ringe, E.; Nordlander, P.; Link, S., Environmental Symmetry Breaking Promotes Plasmon Mode Splitting in Gold Nanotriangles. *The Journal of Physical Chemistry C* **2018**, *122* (25), 13259-13266.

32. Zhang, T.; Shen, H.; Lu, G.; Liu, J.; He, Y.; Wang, Y.; Gong, Q., Single Bipyramid Plasmonic Antenna Orientation Determined by Direct Photoluminescence Pattern Imaging. *Advanced Optical Materials* **2013**, *1* (4), 335-342.

33. Hao, F.; Nehl, C. L.; Hafner, J. H.; Nordlander, P., Plasmon Resonances of a Gold Nanostar. *Nano Letters* **2007**, *7* (3), 729-732.

34. Sánchez-Iglesias, A.; Pastoriza-Santos, I.; Pérez-Juste, J.; Rodríguez-González, B.; García de Abajo, F. J.; Liz-Marzán, L. M., Synthesis and Optical Properties of Gold Nanodecahedra with Size Control. *Advanced Materials* **2006**, *18* (19), 2529-2534.

35. Shao, L.; Susha, A. S.; Cheung, L. S.; Sau, T. K.; Rogach, A. L.; Wang,

- J., Plasmonic Properties of Single Multispiked Gold Nanostars: Correlating Modeling with Experiments. *Langmuir* **2012**, *28* (24), 8979-8984.
36. Shegai, T.; Chen, S.; Miljković, V. D.; Zengin, G.; Johansson, P.; Käll, M., A bimetallic nanoantenna for directional colour routing. *Nature Communications* **2011**, *2* (1), 481.
37. Liang, H.; Li, Z.; Wang, W.; Wu, Y.; Xu, H., Highly Surface-roughened “Flower-like” Silver Nanoparticles for Extremely Sensitive Substrates of Surface-enhanced Raman Scattering. *Advanced Materials* **2009**, *21* (45), 4614-4618.
38. Stranahan, S. M.; Titus, E. J.; Willets, K. A., Discriminating Nanoparticle Dimers from Higher Order Aggregates through Wavelength-Dependent SERS Orientational Imaging. *ACS Nano* **2012**, *6* (2), 1806-1813.
39. Kim, G. W.; Ha, J. W., Polarization-Sensitive Single Dipoles Generated from Multiple Sharp Branches on the Surfaces of Single Gold Nanourchins. *The Journal of Physical Chemistry C* **2017**, *121* (36), 19975-19982.
40. Xiao, L.; Qiao, Y.; He, Y.; Yeung, E. S., Three Dimensional Orientational Imaging of Nanoparticles with Darkfield Microscopy. *Analytical Chemistry* **2010**, *82* (12), 5268-5274.
41. Lieb, M. A.; Zavislan, J. M.; Novotny, L., Single-molecule orientations determined by direct emission pattern imaging. *J. Opt. Soc. Am. B* **2004**, *21* (6), 1210-1215.
42. Böhmer, M.; Enderlein, J., Orientation imaging of single molecules by wide-field epifluorescence microscopy. *J. Opt. Soc. Am. B* **2003**, *20* (3), 554-559.

2.1.7 Figures and Captions

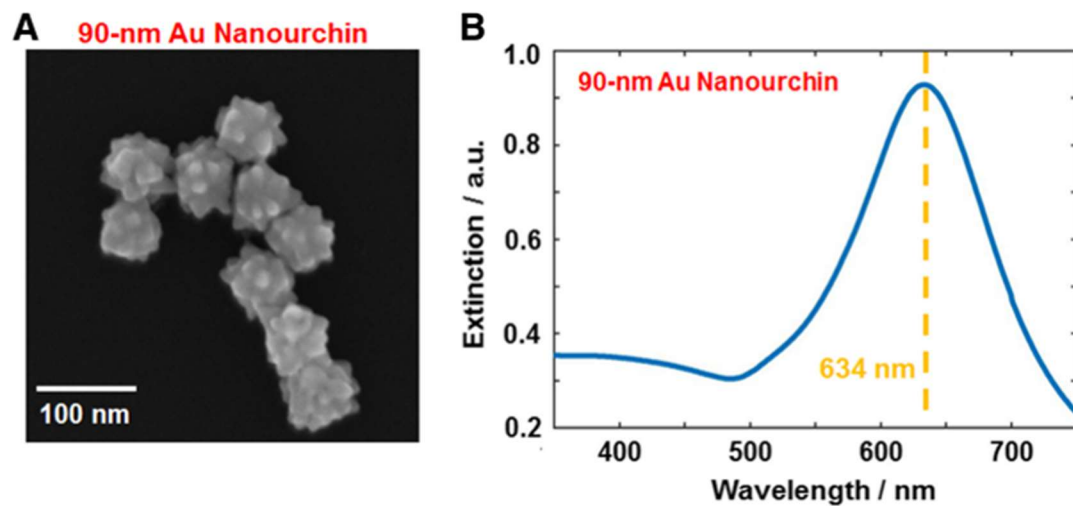


Figure 7. (A) SEM image of 90 nm AuNUs with sharp and short branches. (B) UV-Vis absorption spectrum of 90 nm AuNUs dispersed in water. A single broad peak is observed at approximately 634 nm indicated by the yellow-dotted line.

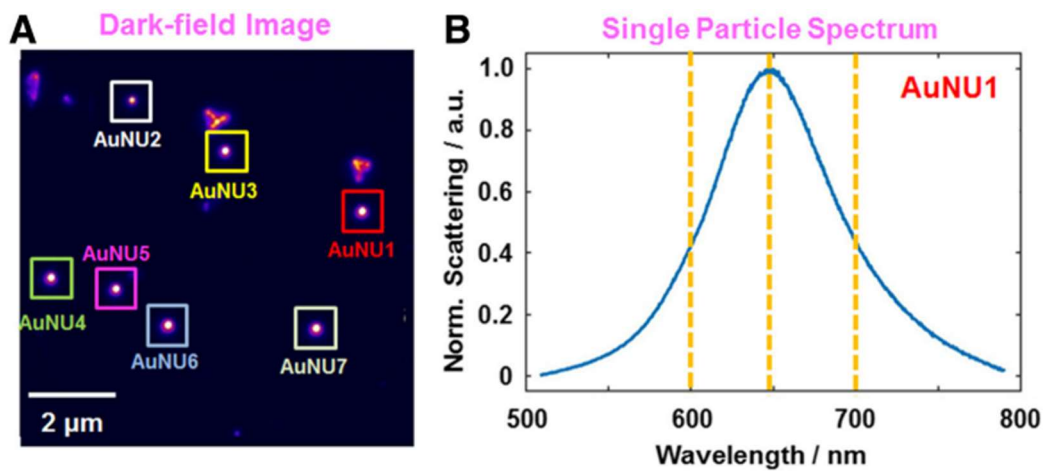


Figure 8. (A) DF scattering image of 90 nm AuNUs deposited on a glass slide. (B) Single particle scattering spectrum of AuNU1 highlighted with a red square in (A). A single LSPR peak was observed around 650 nm for the AuNU1. The yellow-dotted lines indicate the incident LSPR wavelengths (600 nm, 640 nm, 700 nm) used in this study.

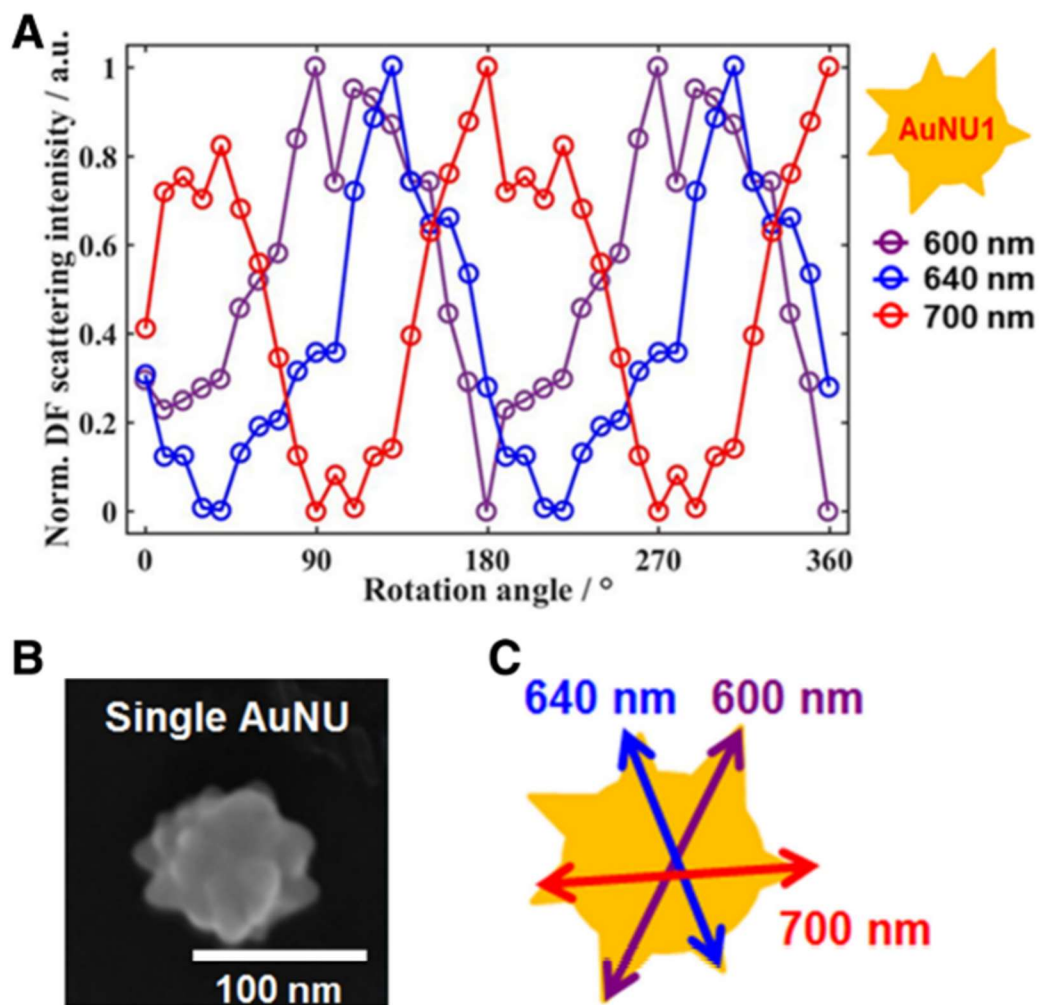


Figure 9. (A) Normalized DF intensities for AuNU1 at the three different LSPR wavelengths as a function of the rotational angle. (B) Enlarged SEM image of a single AuNU with a spiky uneven surface. (C) Schematic diagram showing the generation of single dipoles with different wavelengths in multiple directions on the same AuNU surface.

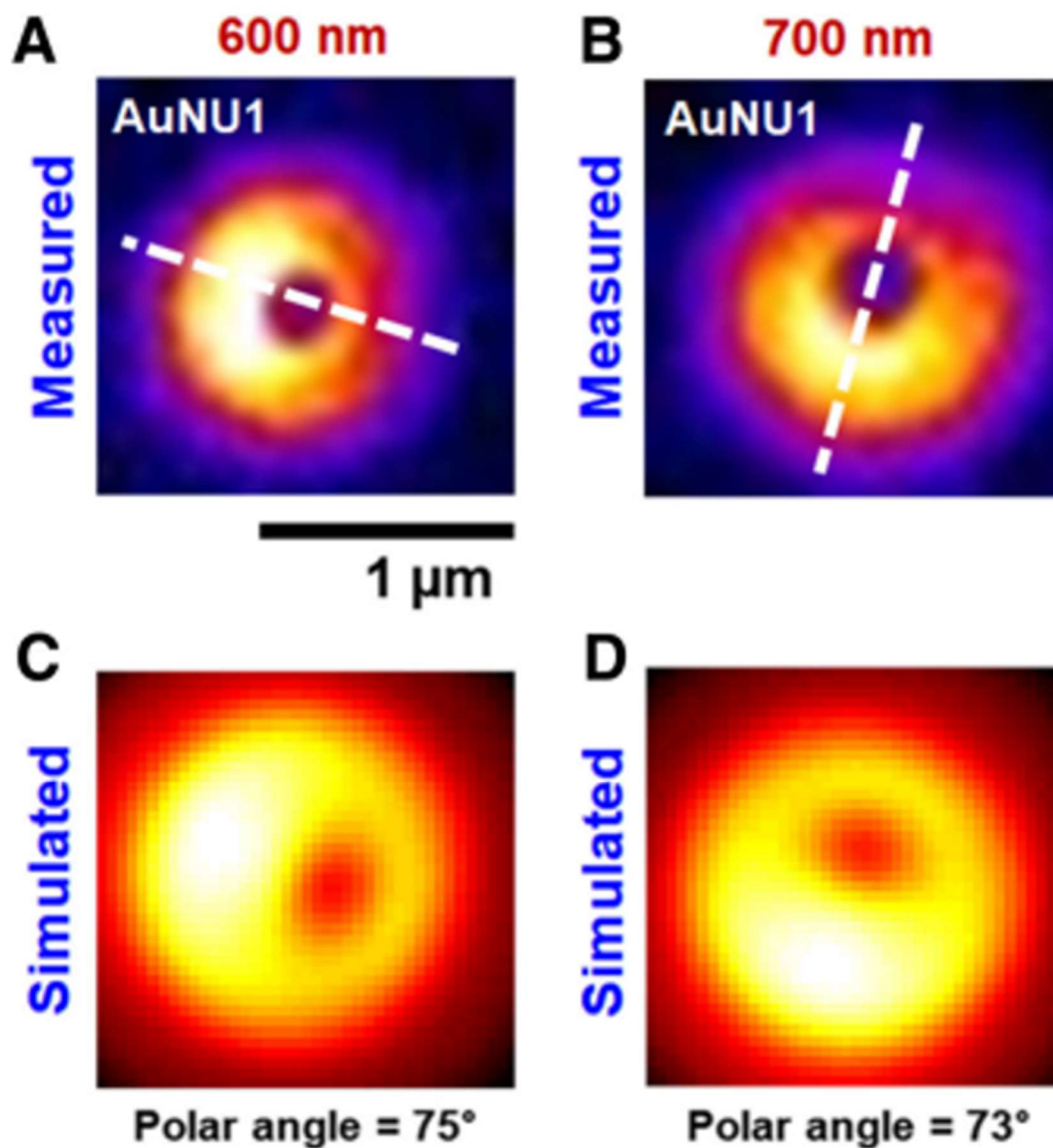


Figure 10. (A, C) Measured and best-matched simulation patterns of single AuNU1 on a glass slide at 600 nm. (B, D) Measured and best-matched simulation patterns of single AuNU1 at 700 nm. The white-dotted line shows the single dipole orientation generated on the AuNU surface at the LSPR wavelength. The scale bar represents 1 μm .

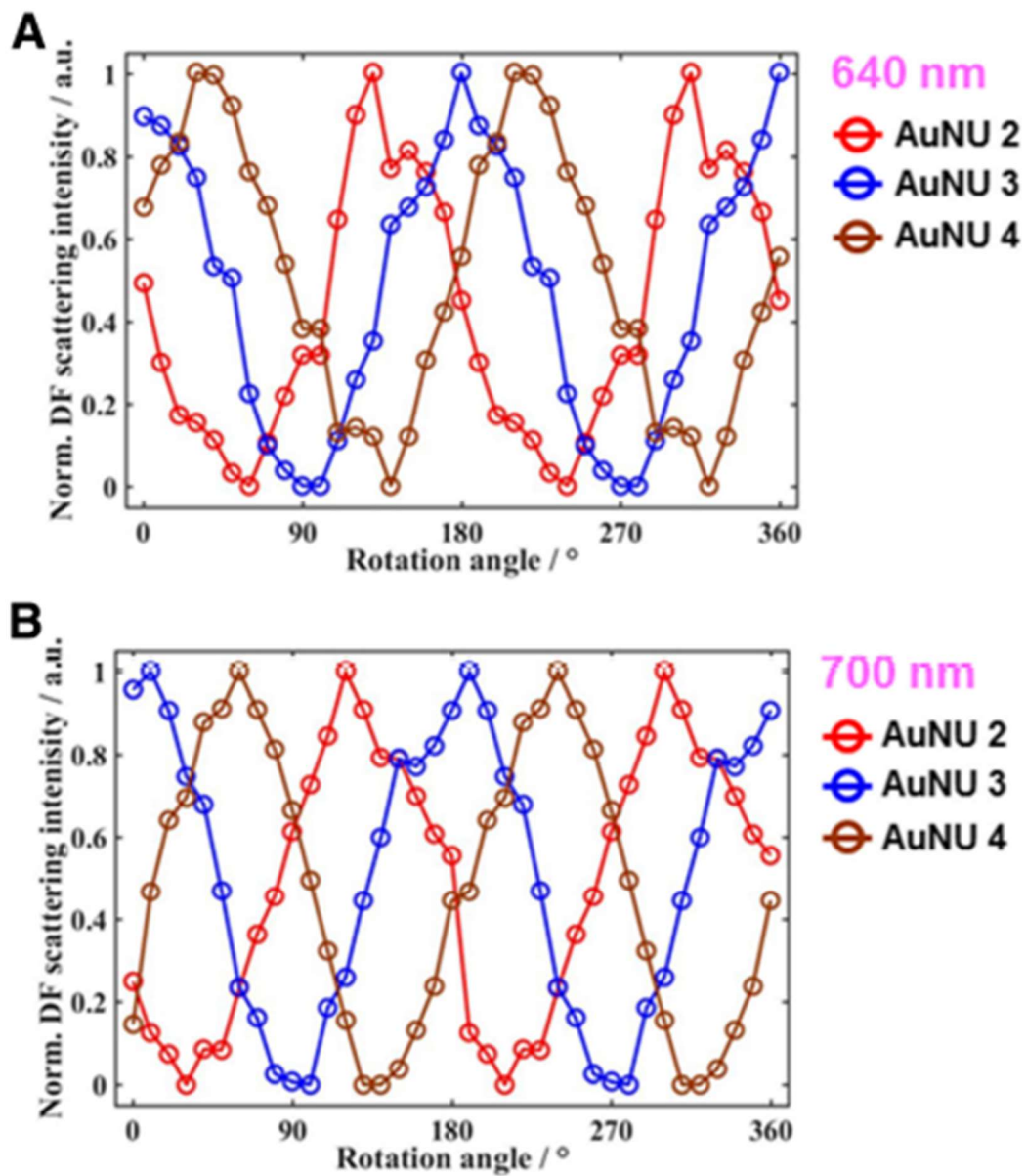


Figure 11. (A) Changes in the normalized scattering intensities for three AuNUs (AuNU2 to AuNU4) at 640 nm as a function of the rotational angle. (B) Changes in the normalized scattering intensities for three AuNUs (AuNU2 to AuNU4) at 700 nm as a function of the rotational angle.

2.1.8 Supplementary Materials

Defocused Orientation and Position Imaging Technique

AuNRs that are much smaller than the wavelength of incident light can be considered electric point dipoles. According to an electrostatic approximation, plasmon oscillations from anisotropic AuNR can be simplified as three-perpendicular independent dipoles along the three axes (**Fig. 6B**). Oscillation along the long principal axis (a-axis) is defined as a longitudinal mode and the other perpendicular oscillations are defined as transverse modes vibrating along the short axes (b and c axes). E_a indicates the scattering electric field of the nanorod along the main long axis, while E_b and E_c are the scattering electric fields along the short transverse axes, b and c. The overall scattering electrical field from a AuNR can be quantified through a linear superposition of three independent scattering electric fields associated with three mutually orthogonal dipoles, as shown in Eq. (1):

$$E_{(scat)} = \sum_{a,b,c} E_{(scat)j} = E_{(scat)a} + E_{(scat)b} + E_{(scat)c} \quad (1)$$

However, E_a the scattering electric field of the nanorod along the main long axis (or the longitudinal dipole) is much more dominant than the two transverse dipoles. Therefore, a AuNR behaves as a single dipole character.

Defocused orientation and position imaging (DOPI) technique is a direct and simple method with the capability of visualizing and determining three-dimensional (3D) dipole orientation of anisotropic single AuNRs. The core idea is that the direct

detection of the spatial distribution of the scattered or emitted field of single dipoles becomes possible when the imaging system is defocused deliberately by $\sim 1 \mu\text{m}$.

Simulation of Scattering Image Patterns of AuNRs

We used the simulation program developed by Enderlein and Böhmer. The program is designed to calculate the characteristic intensity distribution from an emitter with three perpendicular emission dipoles of different emission strength. It has been widely used to determine the spatial orientation of single dye molecules. The simulation program is a special Matlab based utility with a graphics user interface (GUI) for easy calculation. This program allows us to calculate exactly the defocused (or focused) images of single molecules. For using the GUI, one should download the files from the website.

(<http://www.joerg-enderlein.de/imagingOfSingleMolecules.html>)

The parameters that can be input are: the numerical aperture of the objective lens, magnification of imaging, extent of defocusing (or defocusing distance in micrometers), κ and R . Therefore, in this simulation, we adjusted the numerical aperture of the objective lens and magnification of imaging and defocusing. Furthermore, we adjusted the parameters κ and R into the program to define the emission strength ratios of the three independent dipoles (**Fig. 6B**). The ratio κ defines the ratio of the emission strength of the b- to the c-dipole (transverse dipoles, **Fig. 6B**) as shown below.

$$I_b / I_c = (1 - \kappa) / (1 + \kappa) \quad (2)$$

In addition, the ratio R defines the emission strength of the a-dipole (or longitudinal dipole) to the combined b and c dipoles (or transverse dipoles) as shown below.

$$R \times I_a + (1 - R) \times (I_b + I_c) \quad (3)$$

When R is 1, we only have the contribution from a-dipole (longitudinal dipole) to the image patterns. In the present study, we used a R value of 1 to simulate the scattering patterns of single dipoles generated on the AuNU surface at different LSPR excitation wavelengths.

2.2 Polarization- and wavelength-dependent defocused scattering imaging of single gold nanostars with multiple long branches

Geun Wan Kim and Ji Won Ha*

A paper published in Photochemical & Photobiological Sciences, **2019**, 18, 1430.

Reproduced by permission of the Royal Society of Chemistry (RSC)

*Corresponding author

2.2.1 Abstract

The scattering properties of gold nanostars (AuNSs) are not completely understood. Furthermore, there have been no studies on the dark-field (DF) scattering patterns of a AuNS in defocused DF microscopy. Herein, we demonstrate the polarization- and wavelength-dependent defocused scattering properties at the localized surface plasmon resonance (LSPR) wavelengths of single AuNSs with multiple long branches protruding from their surfaces. The defocused scattering intensities of single AuNSs at two LSPR excitation wavelengths changed periodically as a function of the rotational angle of a polarizer, whereas the doughnut-shaped scattering pattern remained unaltered. Furthermore, the characteristic doughnut-shaped defocused scattering pattern enabled the resolution of the spatial field distributions of single dipoles on the same AuNS surface at two LSPR wavelengths. Finally, we tracked the real-time rotational dynamics of a AuNS rotating on a glass slide using defocused microscopy. These results provide a deeper understanding of the defocused scattering properties of single AuNSs with multiple sharp, long branches randomly protruding from their surfaces.

2.2.2 Introduction

Plasmonic metal nanoparticles have attracted growing interest over the last few decades because of their unique optical properties that are attributable to localized surface plasmon resonance (LSPR), i.e., the resonant oscillations of free electrons in the conduction band induced by specific frequencies of light.^{1, 2} Owing to their high chemical and photostability, excellent biocompatibility, and easy surface functionalization, gold nanoparticles have been extensively used as surface-enhanced Raman scattering substrates,³⁻⁸ bio- and chemical sensors,⁹⁻¹² and photosensitizers in photothermal therapy.¹³⁻¹⁵

Increasing the particle size of isotropic gold nanospheres produces a limited range of the red-shift of the LSPR wavelength from 510 nm to 550 nm.¹⁵⁻¹⁷ Isotropic gold nanospheres have a relatively narrow area of applications due to the limited tuning range of the LSPR wavelength and weak enhancement of the electromagnetic field.¹⁸ However, anisotropic gold nanoparticles, such as nanostars,^{4, 9, 14, 19, 20} nanourchins,¹¹ nanorods,²¹⁻²³ nanoplates,²⁴ and bipyramids²⁵ have been investigated for a variety of applications because they exhibit a broad range of LSPR wavelengths, i.e., visible near infrared, and strong electromagnetic field enhancement,^{16, 26, 27} which have been reported by both experimental and computational studies. In particular, gold nanoparticles with rough surfaces that generate strong hot spots have been widely employed in SERS^{28, 29} and LSPR-based biosensors.^{9, 30} In addition, gold nanostars (AuNSs) have been used for single nanoparticle label-free LSPR biosensing with high sensitivity.^{9, 31}

With the recent progress in single particle spectroscopy, it became possible to study the characteristic optical properties of gold nanoparticles without ensemble averaging. To date, the optical properties of branched gold nanoparticles have been mainly investigated by scattering-based dark-field (DF) microscopy and spectroscopy.³²⁻³⁴ Furthermore, computational calculation has been used to reveal their shape induced, characteristic optical properties.^{28, 30, 35, 36} For example, the polarization-sensitive scattering properties of single gold nanourchins (AuNUs) with short branches were studied under a DF microscope at the LSPR wavelength of 700 nm;³⁷ single dipoles in multiple directions were generated on the surface of a single AuNU. However, the scattering properties of AuNSs, which have longer and fewer branches than that of AuNUs, are not completely understood. Furthermore, there have been no studies on the DF scattering patterns of a AuNS in defocused DF microscopy. The defocused DF imaging of a AuNS would provide valuable information such as spatial field distributions that cannot be obtained from the measurements at the focal plane. In the present study, we use a defocused DF microscope to verify the polarization- and wavelength-dependent defocused scattering properties of single AuNS with multiple long branches. Furthermore, we demonstrated that the three-dimensional (3D) orientation of a AuNS can be directly resolved from the characteristic spatial scattering field distribution at the LSPR wavelength under defocused microscopy

2.2.3 Experimental Section

Materials and Sample Preparation

AuNSs with an average size of 100 nm were purchased from Nanopartz (Loveland, CO, USA). The samples for single particles studies were prepared as follows: the colloid solution with the initial concentration of 0.24 mM was first diluted with 18.2 M Ω pure water to a proper concentration (10 μ M). The diluted solution was then sonicated for 10 min at room temperature. Samples were prepared by spin casting AuNSs on pre-cleaned glass slides. Subsequently, a 22 mm \times 22 mm no. 1.5 coverslip (Corning, NY, USA) was placed on the glass slide. Throughout all of the experiments, the concentration of AuNSs on the glass slide surface was maintained at about 1 μ m⁻² to facilitate single-AuNS characterization without inter-particle interaction.

Characterization

We used a scanning electron microscope (SEM, JSM6500F, JEOL, Japan) to characterize citrate-stabilized AuNSs. Furthermore, a Varian Carry 300 UV–Vis spectrometer was used to characterize the ensemble extinction spectrum of AuNSs in water.

Dark-Field Microscopy and Spectroscopy

Using an in-house system, DF microscopy imaging was carried out using a Nikon inverted microscope (ECLIPSE Ti-U). In DF mode, we utilized a Nikon Plan Fluor 100 \times 0.5–1.3 oil iris objective and a Nikon DF condenser. The Andor iXon^{EM+}

CCD camera (iXon Ultra 897, UK) was applied to obtain DF scattering images of the AuNPs. The collected images were analyzed with the software Image J. Furthermore, we obtained DF scattering spectra with an Andor spectrometer (SHAMROCK 303i, SR-303I-A, UK) and an Andor CCD camera (Newton DU920P-OE, UK). For analysis, the scanning stage was positioned such that the sample was at the desired location. Therefore, only the scattered light from the selected location was collected by the objective. The scattered light was directed to the spectrometer, dispersed by a grating (300 lines per mm, center wavelength of 700 nm), and detected by a Newton CCD camera (Andor, UK). The background spectrum was obtained at a region without particles.

Polarization-Dependent DF Scattering Measurement

In this study, we performed polarization-dependent DF scattering imaging of single AuNS by linearly polarizing the excitation beam and changing the polarization in 10° increments. We placed a polarizer in the light path to detect the polarization-dependent scattering light from the samples. Then, we performed the wavelength-dependent single particle DF studies by using two bandpass filters (Thorlabs, Newton, NJ, USA) with center wavelengths of 640 nm (± 5 nm) and 700 nm (± 5 nm). The bandpass filters were inserted into the light path of the microscope to illuminate the samples. We carried out a study on the rotation of single AuNSs at two excitation wavelengths by rotating the stage at 10° intervals. When the polarizer was rotated, AuNSs fixed on the glass slide were positioned in different orientations.

2.2.4 Result and Discussion

The 3D structures of the 100 nm AuNSs were characterized by SEM. As shown in **Fig. 12A**, the branches on the surface of the AuNSs had different lengths and extended in random directions from the 50 nm diameter core. The UV–Vis extinction spectrum of AuNSs dispersed in 18.2 M Ω pure water is shown in **Fig. 12B**. The branched AuNSs exhibited a single, broad LSPR spectrum, and the LSPR wavelength appeared at around 640 nm.

We then investigated the optical properties of single AuNSs under scattering-based DF microscopy, which enabled us to eliminate the ensemble averaging. For single particle characterization, a sample was prepared by spin casting a solution containing AuNSs on a glass slide. The scattering of the AuNSs was then measured by illuminating them with white light focused by a high numerical aperture oil condenser under the DF microscope. Here a vertical scan in the z-direction with a step size of 40 nm allowed for obtaining both focused and defocused DF scattering images of the AuNSs (**Fig. 13A, B**). **Fig. 13A and B** show enlarged focused and defocused DF scattering images of single AuNSs, respectively. As shown in **Fig. 13B**, the characteristic doughnut-shaped scattering pattern was observed under defocused microscopy for single AuNSs at a defocusing distance of $\sim 1 \mu\text{m}$. We then obtained single particle scattering spectra of AuNSs having branches protruding in random directions from the particle surfaces. As shown in **Fig. S1**, single AuNSs showed characteristic and different LSPR spectra that contained multiple peaks due to the heterogeneity of the number of branches, spatial orientations, and sizes of the sharp

branches, etc. Therefore, it was important to confirm the LSPR wavelengths of single AuNSs to be measured and studied. We checked the LSPR peaks of AuNS1 and AuNS2 from their single particle scattering spectra (**Fig. 13C and D**). Two LSPR peaks appeared at 651 nm (as measured on the shoulder) and 689 nm for the AuNS1 labeled in **Fig. 13A**. Furthermore, two LSPR wavelengths for the AuNS2 were determined to be 662 nm and 697 nm by fitting. We thus used two excitation wavelengths of 640 and 700 nm, as indicated by the red, dashed lines in **Fig. 13C and D**, to investigate the characteristic scattering properties of two AuNSs (AuNS1 and AuNS2). In our previous study, we reported that single dipoles can be generated on branched AuNUs.³⁷ Therefore, the two LSPR peaks found for each single AuNS, as shown in **Fig. 13C and D**, can be explained by the generation of multiple single dipoles on the AuNS surface that are caused by the long branches protruding in random directions.

To verify the characteristic scattering properties of single AuNSs and the generation of multiple single dipoles on the AuNS, we implemented defocused DF scattering microscopy. There are two reasons to employ the defocused DF scattering imaging technique in this study. First, it allows for the detection of the spatial scattering distribution of the emitted field of single dipole when an aberration is deliberately applied to the imaging system³⁸⁻⁴⁰. Second, there have been no studies to report the defocused scattering properties of single AuNSs with sharp, long branches.

We first conducted the rotational study at the two LSPR excitation wavelengths of 640 and 700 nm by rotating a polarizer at 10° increments under a

defocused DF microscope. **Fig. 14A** shows defocused DF scattering images of AuNS1 with 30° intervals, which were extracted from complete set of images. As shown in **Fig. 14A**, the single AuNS1 showed characteristic doughnut-shaped scattering patterns at both LSPR excitation wavelengths. Furthermore, according to the rotation of the polarizer, the brightness (or scattering intensities) of the defocused image patterns of AuNS1 changed periodically without changing in the open direction of the characteristic scattering pattern (**Fig. 14C**). Therefore, we found that single dipoles are generated on the AuNS surface at two LSPR excitation wavelengths and that single dipoles have polarization-dependent scattering properties. More importantly, the difference of the phase of the two wavelengths, as shown in **Fig. 14C**, indicates that the single dipole excited at 700 nm has a different spatial orientation from that of the single dipole excited at 640 nm, as depicted in **Fig. 14D**.

To further elucidate the difference in the orientation of single dipoles generated on the AuNS surface at two LSPR excitation wavelengths, we took a closer look at the doughnut-shaped, defocused DF scattering image patterns of the single AuNS1 at the two LSPR wavelengths (**Fig. 15**). Note that the defocused imaging technique has the capability to resolve 3D spatial field distributions (or dipole orientations). More specifically, when a single dipole on the AuNS is tilted away from the glass surface, the asymmetric doughnut-shaped scattering image pattern is observed, which would allow the spatial field distributions of a gold nanorod to be deciphered.⁴⁰⁻⁴² **Fig. 15A and B** show enlarged DF scattering image patterns of AuNS1 at two different wavelengths (640 nm and 700 nm). In **Fig. 15A and C**, the ring of the

doughnut-shaped scattering image patterns is observed to be open, and the location of the opening can be used to estimate the orientation of the single dipole according to the two excitation wavelengths. The definitions of the out-of-plane polar angle θ and the in-plane azimuthal angle ϕ of a dipole axis of AuNS in 3D space are provided in **Fig. 6B**. We can readily extract the in plane orientation angle ϕ from the two-lobe scattering pattern exhibiting angular anisotropy, as indicated by the white dotted line in **Fig. 15A and C**. However, the polar angle θ was estimated by using the program developed by Enderlein and Böhmer for simulating the characteristic intensity distribution from an emitter with three perpendicular emission dipoles of different emission strengths.^{38,39} The orientation of a single dipole generated on the AuNS1 on a glass substrate was estimated by referring to the corresponding field map at both LSPR wavelengths. The best-fit simulated scattering pattern is shown in **Fig. 15B and D**, and the simulated images match the measured patterns well. The 3D spatial orientations of two single dipoles generated on the AuNS surface at two LSPR wavelengths and determined through the pattern match analysis are illustrated in **Fig. 15E and F**. The red line shows the determined 3D orientation, and the blue dotted line is the corresponding in-plane projection. Therefore, the characterization of the scattering intensity distribution from each dipole on the AuNS surface allows the detection and visualization of its spatial orientation at the two LSPR wavelengths.

We also tested if each dipole generated on the AuNS surface can be tracked in real time during a dynamic process under a defocused DF microscope. We chose a AuNS rotating on a glass slide as a model system and found, by chance, that some

AuNSs were rotating on the glass slide, though a majority of the AuNSs were fixed on the substrate. We therefore recorded a movie to show the real-time dynamics of a AuNS rotating on a glass slide with a temporal resolution of 100 ms under a defocused DF microscope. **Fig. S2** shows consecutive defocused DF images of an AuNS excited at 700 nm. As clearly shown in **Fig. 16A**, the characteristic doughnut-shaped scattering patterns were observed and changed as a function of time. We determined the 3D orientation angles of the AuNS for the 30 consecutive images in **Fig. S2** through a pattern matching analysis. As seen in **Fig. 16B**, slight movement of the AuNS on the glass slide was observed at 700 nm. Therefore, we were able to track real-time rotational dynamics of a single dipole on the AuNS surface using defocused DF microscopy.

2.2.5 Conclusion

In summary, we characterized polarization- and wavelength-dependent defocused scattering properties of AuNSs having long branches protruding from their surfaces. Characteristic doughnut-shaped defocused scattering patterns were observed for single AuNSs at their LSPR wavelengths, and the defocused scattering intensities changed periodically as a function of the incident light polarization. Furthermore, we resolved the 3D orientations of single dipoles generated on the AuNS surface at the LSPR wavelengths by using defocused DF microscopy. Finally, we demonstrated that the real-time 3D orientation angles of a AuNS rotating on the glass slide can be deciphered at the LSPR wavelength. The results of this investigation provide new

insight into the characteristic defocused scattering properties and image patterns of single AuNSs at their LSPR wavelengths.

2.2.6 References

1. Novotny, L.; van Hulst, N., Antennas for light. *Nature Photonics* **2011**, *5* (2), 83-90.
2. Schuller, J. A.; Barnard, E. S.; Cai, W.; Jun, Y. C.; White, J. S.; Brongersma, M. L., Plasmonics for extreme light concentration and manipulation. *Nature Materials* **2010**, *9* (3), 193-204.
3. Wang, H.; Halas, N. J., Mesoscopic Au “Meatball” Particles. *Advanced Materials* **2008**, *20* (4), 820-825.
4. He, S.; Chua, J.; Tan, E. K. M.; Kah, J. C. Y., Optimizing the SERS enhancement of a facile gold nanostar immobilized paper-based SERS substrate. *RSC Advances* **2017**, *7* (27), 16264-16272.
5. Xie, J.; Zhang, Q.; Lee, J. Y.; Wang, D. I. C., The Synthesis of SERS-Active Gold Nanoflower Tags for In Vivo Applications. *ACS Nano* **2008**, *2* (12), 2473-2480.
6. Chirumamilla, M.; Gopalakrishnan, A.; Toma, A.; Proietti Zaccaria, R.; Krahne, R., Plasmon resonance tuning in metal nanostars for surface enhanced Raman scattering. *Nanotechnology* **2014**, *25* (23), 235303.
7. Jimenez de Aberasturi, D.; Serrano-Montes, A. B.; Langer, J.; Henriksen-Lacey, M.; Parak, W. J.; Liz-Marzán, L. M., Surface Enhanced Raman Scattering Encoded Gold Nanostars for Multiplexed Cell Discrimination. *Chemistry of Materials* **2016**, *28* (18), 6779-6790.
8. Lu, G.; Forbes, T. Z.; Haes, A. J., SERS detection of uranyl using

functionalized gold nanostars promoted by nanoparticle shape and size. *Analyst* **2016**, *141* (17), 5137-5143.

9. Dondapati, S. K.; Sau, T. K.; Hrelescu, C.; Klar, T. A.; Stefani, F. D.; Feldmann, J., Label-free Biosensing Based on Single Gold Nanostars as Plasmonic Transducers. *ACS Nano* **2010**, *4* (11), 6318-6322.

10. Wang, W.; Cui, H., Chitosan-Luminol Reduced Gold Nanoflowers: From One-Pot Synthesis to Morphology-Dependent SPR and Chemiluminescence Sensing. *The Journal of Physical Chemistry C* **2008**, *112* (29), 10759-10766.

11. Thapliyal, N. B.; Chiwunze, T. E.; Karpoormath, R.; Cherukupalli, S., Fabrication of highly sensitive gold nanourchins based electrochemical sensor for nanomolar determination of primaquine. *Materials Science and Engineering: C* **2017**, *74*, 27-35.

12. Haes, A. J.; Hall, W. P.; Chang, L.; Klein, W. L.; Van Duyne, R. P., A Localized Surface Plasmon Resonance Biosensor: First Steps toward an Assay for Alzheimer's Disease. *Nano Letters* **2004**, *4* (6), 1029-1034.

13. Park, J.; Estrada, A.; Sharp, K.; Sang, K.; Schwartz, J. A.; Smith, D. K.; Coleman, C.; Payne, J. D.; Korgel, B. A.; Dunn, A. K.; Tunnell, J. W., Two-photon-induced photoluminescence imaging of tumors using near-infrared excited gold nanoshells. *Opt. Express* **2008**, *16* (3), 1590-1599.

14. Chen, H.; Zhang, X.; Dai, S.; Ma, Y.; Cui, S.; Achilefu, S.; Gu, Y., Multifunctional Gold Nanostar Conjugates for Tumor Imaging and Combined Photothermal and Chemo-therapy. *Theranostics* **2013**, *3* (9), 633-649.

15. Khlebtsov, B.; Zharov, V.; Melnikov, A.; Tuchin, V.; Khlebtsov, N., Optical amplification of photothermal therapy with gold nanoparticles and nanoclusters. *Nanotechnology* **2006**, *17* (20), 5167-5179.
16. Li, M.; Cushing, S. K.; Wu, N., Plasmon-enhanced optical sensors: a review. *Analyst* **2015**, *140* (2), 386-406.
17. Li, M.; Cushing, S. K.; Wang, Q.; Shi, X.; Hornak, L. A.; Hong, Z.; Wu, N., Size-Dependent Energy Transfer between CdSe/ZnS Quantum Dots and Gold Nanoparticles. *The Journal of Physical Chemistry Letters* **2011**, *2* (17), 2125-2129.
18. Li, M.; Cushing, S. K.; Zhang, J.; Lankford, J.; Aguilar, Z. P.; Ma, D.; Wu, N., Shape-dependent surface-enhanced Raman scattering in gold–Raman-probe–silica sandwiched nanoparticles for biocompatible applications. *Nanotechnology* **2012**, *23* (11), 115501.
19. Pu, Y.; Zhao, Y.; Zheng, P.; Li, M., Elucidating the Growth Mechanism of Plasmonic Gold Nanostars with Tunable Optical and Photothermal Properties. *Inorganic Chemistry* **2018**, *57* (14), 8599-8607.
20. Senthil Kumar, P.; Pastoriza-Santos, I.; Rodríguez-González, B.; Javier García de Abajo, F.; Liz-Marzán, L. M., High-yield synthesis and optical response of gold nanostars. *Nanotechnology* **2007**, *19* (1), 015606.
21. Won Ha, J.; Sun, W.; Wang, G.; Fang, N., Differential interference contrast polarization anisotropy for tracking rotational dynamics of gold nanorods. *Chemical Communications* **2011**, *47* (27), 7743-7745.
22. Tcherniak, A.; Dominguez-Medina, S.; Chang, W.-S.; Swanglap, P.;

Slaughter, L. S.; Landes, C. F.; Link, S., One-Photon Plasmon Luminescence and Its Application to Correlation Spectroscopy as a Probe for Rotational and Translational Dynamics of Gold Nanorods. *The Journal of Physical Chemistry C* **2011**, *115* (32), 15938-15949.

23. Cao, J.; Galbraith, E. K.; Sun, T.; Grattan, K. T. V., Cross-Comparison of Surface Plasmon Resonance-Based Optical Fiber Sensors With Different Coating Structures. *IEEE Sensors Journal* **2012**, *12* (7), 2355-2361.

24. Smith, K. W.; Yang, J.; Hernandez, T.; Swearer, D. F.; Scarabelli, L.; Zhang, H.; Zhao, H.; Moringo, N. A.; Chang, W.-S.; Liz-Marzán, L. M.; Ringe, E.; Nordlander, P.; Link, S., Environmental Symmetry Breaking Promotes Plasmon Mode Splitting in Gold Nanotriangles. *The Journal of Physical Chemistry C* **2018**, *122* (25), 13259-13266.

25. Zhang, T.; Shen, H.; Lu, G.; Liu, J.; He, Y.; Wang, Y.; Gong, Q., Single Bipyramid Plasmonic Antenna Orientation Determined by Direct Photoluminescence Pattern Imaging. *Advanced Optical Materials* **2013**, *1* (4), 335-342.

26. Gole, A.; Murphy, C. J., Seed-Mediated Synthesis of Gold Nanorods: Role of the Size and Nature of the Seed. *Chemistry of Materials* **2004**, *16* (19), 3633-3640.

27. Jena, B. K.; Raj, C. R., Seedless, Surfactantless Room Temperature Synthesis of Single Crystalline Fluorescent Gold Nanoflowers with Pronounced SERS and Electrocatalytic Activity. *Chemistry of Materials* **2008**, *20* (11), 3546-3548.

28. Hao, F.; Nehl, C. L.; Hafner, J. H.; Nordlander, P., Plasmon Resonances of

a Gold Nanostar. *Nano Letters* **2007**, 7 (3), 729-732.

29. Sánchez-Iglesias, A.; Pastoriza-Santos, I.; Pérez-Juste, J.; Rodríguez-González, B.; García de Abajo, F. J.; Liz-Marzán, L. M., Synthesis and Optical Properties of Gold Nanodecahedra with Size Control. *Advanced Materials* **2006**, 18 (19), 2529-2534.

30. Nehl, C. L.; Liao, H.; Hafner, J. H., Optical Properties of Star-Shaped Gold Nanoparticles. *Nano Letters* **2006**, 6 (4), 683-688.

31. Phiri, M. M.; Mulder, D. W.; Vorster, B. C., Seedless gold nanostars with seed-like advantages for biosensing applications. *Royal Society Open Science* **2019**, 6 (2), 181971.

32. Qi, F.; Han, Y.; Ye, Z.; Liu, H.; Wei, L.; Xiao, L., Color-Coded Single-Particle Pyrophosphate Assay with Dark-Field Optical Microscopy. *Analytical Chemistry* **2018**, 90 (18), 11146-11153.

33. Poon, C.-Y.; Wei, L.; Xu, Y.; Chen, B.; Xiao, L.; Li, H.-W., Quantification of Cancer Biomarkers in Serum Using Scattering-Based Quantitative Single Particle Intensity Measurement with a Dark-Field Microscope. *Analytical Chemistry* **2016**, 88 (17), 8849-8856.

34. Ye, Z.; Weng, R.; Ma, Y.; Wang, F.; Liu, H.; Wei, L.; Xiao, L., Label-Free, Single-Particle, Colorimetric Detection of Permanganate by GNPs@Ag Core-Shell Nanoparticles with Dark-Field Optical Microscopy. *Analytical Chemistry* **2018**, 90 (21), 13044-13050.

35. Shao, L.; Susha, A. S.; Cheung, L. S.; Sau, T. K.; Rogach, A. L.; Wang,

- J., Plasmonic Properties of Single Multispiked Gold Nanostars: Correlating Modeling with Experiments. *Langmuir* **2012**, *28* (24), 8979-8984.
36. Shegai, T.; Chen, S.; Miljković, V. D.; Zengin, G.; Johansson, P.; Käll, M., A bimetallic nanoantenna for directional colour routing. *Nature Communications* **2011**, *2* (1), 481.
37. Kim, G. W.; Ha, J. W., Polarization-Sensitive Single Dipoles Generated from Multiple Sharp Branches on the Surfaces of Single Gold Nanourchins. *The Journal of Physical Chemistry C* **2017**, *121* (36), 19975-19982.
38. Böhmer, M.; Enderlein, J., Orientation imaging of single molecules by wide-field epifluorescence microscopy. *J. Opt. Soc. Am. B* **2003**, *20* (3), 554-559.
39. Lieb, M. A.; Zavislan, J. M.; Novotny, L., Single-molecule orientations determined by direct emission pattern imaging. *J. Opt. Soc. Am. B* **2004**, *21* (6), 1210-1215.
40. Xiao, L.; Ha, J. W.; Wei, L.; Wang, G.; Fang, N., Determining the Full Three-Dimensional Orientation of Single Anisotropic Nanoparticles by Differential Interference Contrast Microscopy. *Angewandte Chemie International Edition* **2012**, *51* (31), 7734-7738.
41. Kim, G. W.; Ha, J. W., Direct Visualization of Wavelength-Dependent Single Dipoles Generated on Single Gold Nanourchins with Sharp Branches. *Nanoscale Research Letters* **2018**, *13* (1), 256.
42. Xiao, L.; Qiao, Y.; He, Y.; Yeung, E. S., Three Dimensional Orientational Imaging of Nanoparticles with Darkfield Microscopy. *Analytical Chemistry* **2010**, *82*

(12), 5268-5274.

2.2.7 Figures and Captions

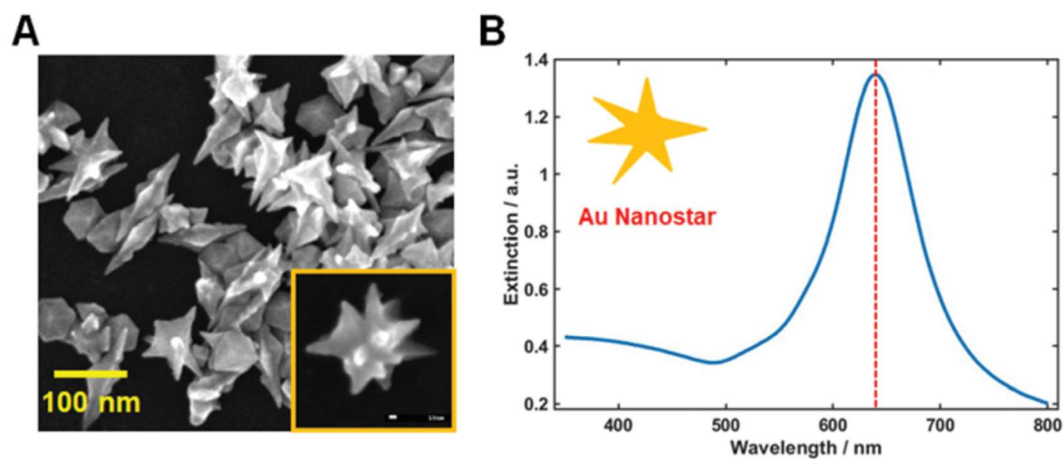


Figure 12. (A) SEM image of AuNSs with sharp and long branches. The scale bar in the inset is 10 nm. (B) UV-Vis extinction spectrum of AuNSs dispersed in water. A single broad peak is observed at approximately 634 nm, as indicated by the red dashed line.

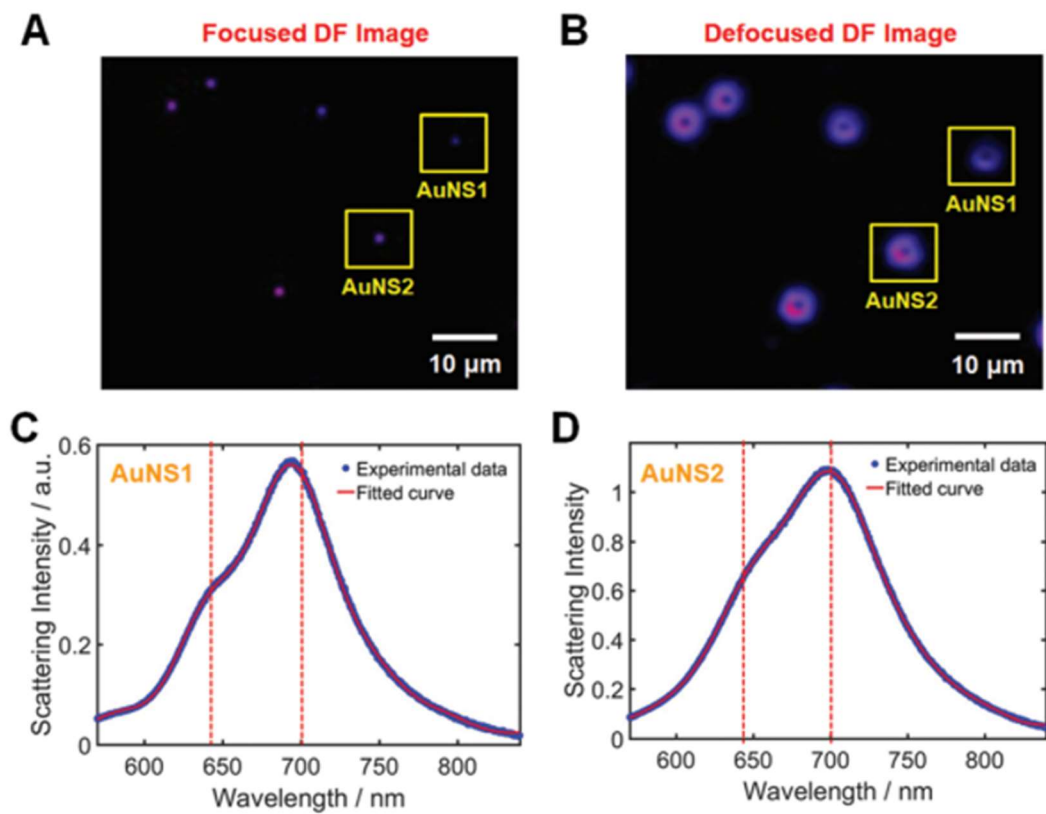


Figure 13. (A) Focused DF scattering image of single AuNSs. (B) Defocused DF scattering image of the same AuNSs. (C) Scattering spectrum of AuNS1 in (A), a single AuNS. (D) Scattering spectrum of AuNS2 in (A). The red dashed lines indicate the incident LSPR wavelengths (640 nm, 700 nm) used in this study.

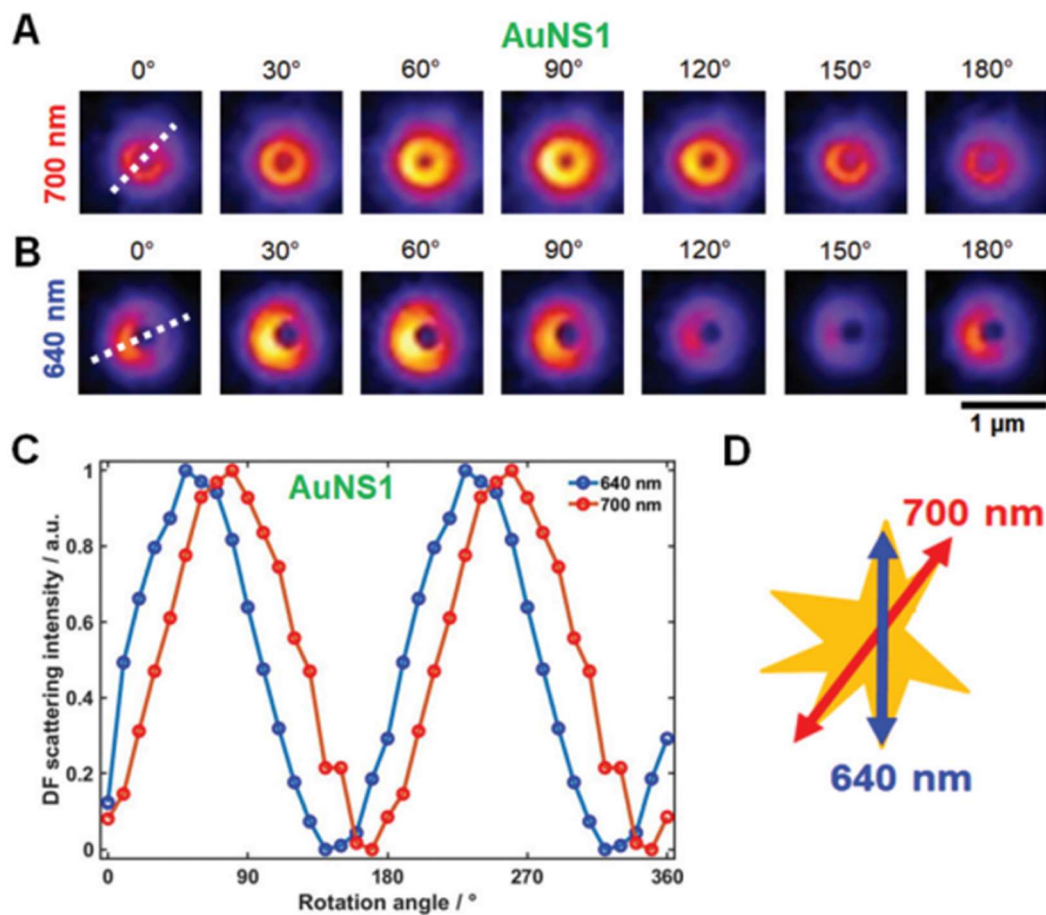


Figure 14. (A) Consecutive, defocused DF scattering image patterns of AuNS1 measured at 700 nm at 30° intervals. (B) Consecutive defocused DF scattering image patterns of AuNS1 measured at 640 nm at 30° intervals. (C) Changes in the DF scattering intensities of AuNS1 at two different LSPR wavelengths of 640 nm (blue curve) and 700 nm (red curve). (D) Schematic diagram depicting the generation of single dipoles on the AuNS surface at two different LSPR excitation wavelengths.

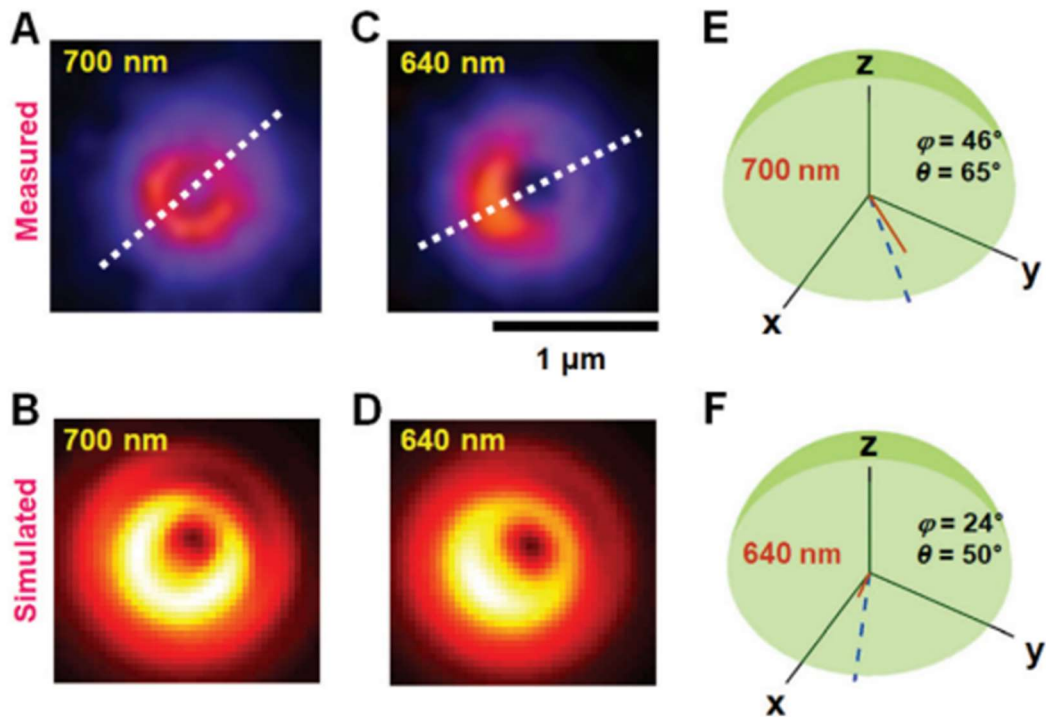


Figure 15. (A, C) Measured defocused scattering image patterns of the single AuNS1 at two LSPR wavelengths, 640 nm and 700 nm. The white dashed line indicates the single dipole orientation generated on the AuNS surface. The scale bar represents 1 μm . (B, D) The corresponding best-fit simulated scattering patterns of AuNS1 at both wavelengths. (E, F) The 3D spatial orientations of AuNS1 determined through the pattern match analysis are illustrated. The red line shows the determined 3D orientation, and the blue dotted line is the corresponding in-plane projection.

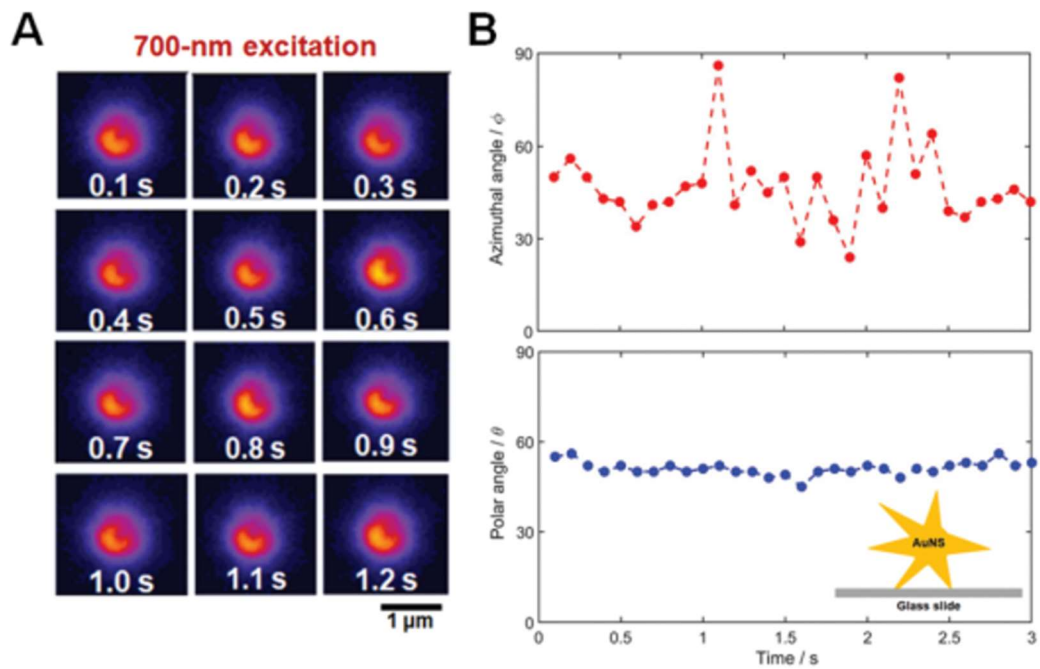


Figure 16. (A) Consecutive defocused image patterns of AuNS rotating on a glass slide measured at 700 nm. (B) 3D orientation angles (the in-plane azimuthal angle φ and the out-of-plane polar angle θ) of the AuNS for 30 frames during the dynamic process.

2.2.8 Supplementary Materials

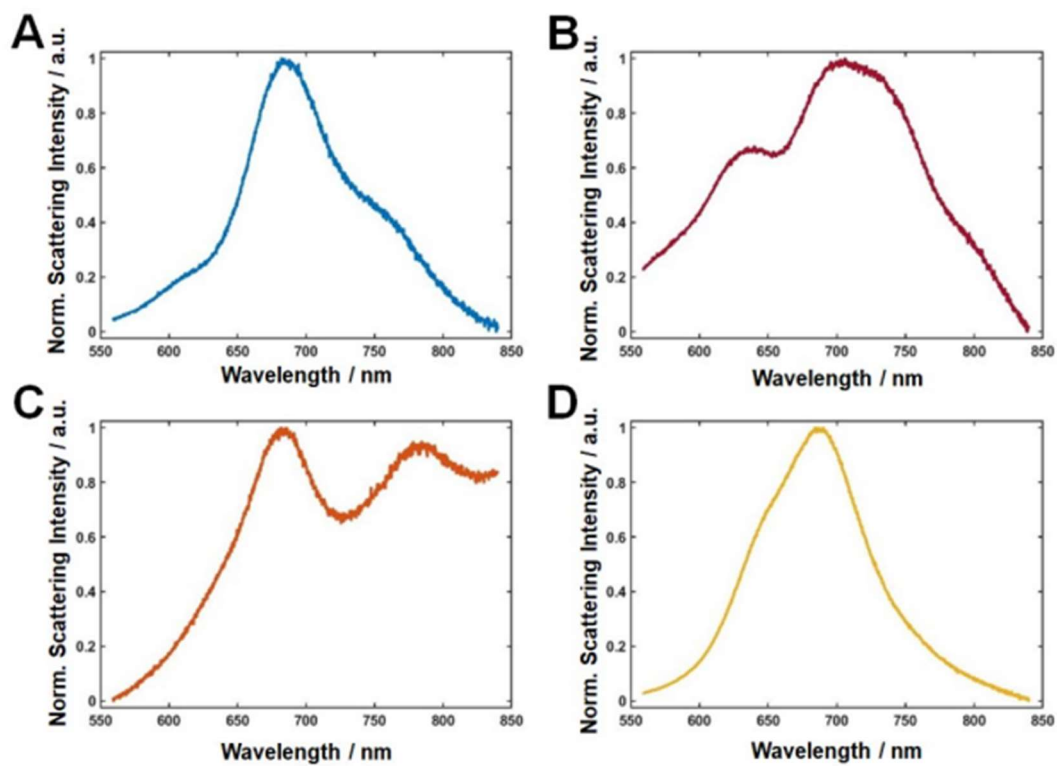


Figure S1. Normalized scattering spectra of single AuNSs with multiple LSPR peaks.

Defocused DF Images at 700-nm excitation

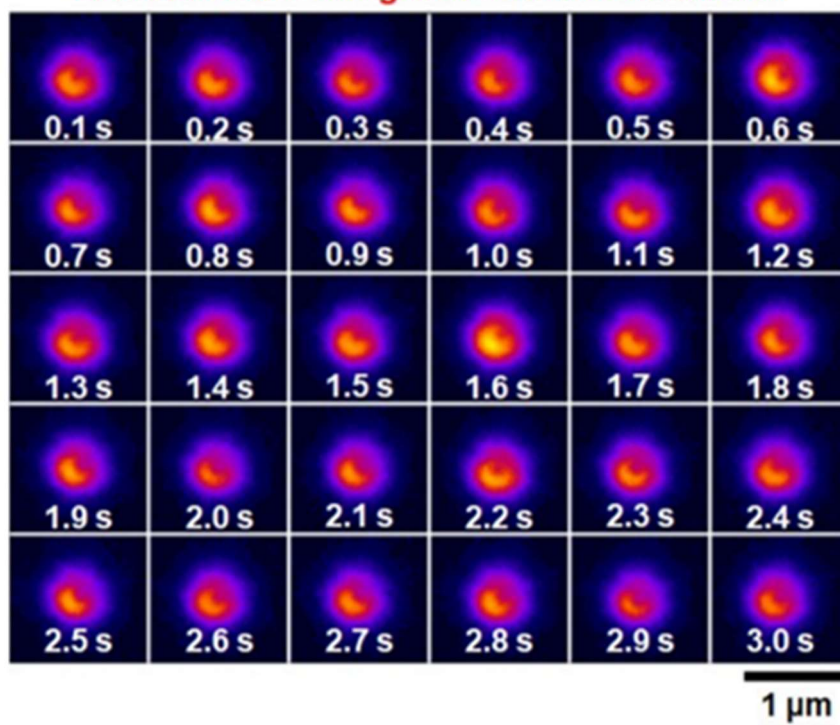


Figure S2 30 consecutive defocused image patterns of single AuNS rotating on a glass slide, detected at 700 nm with a temporal resolution of 100 ms.

Chapter 3. High-Throughput Characterization and In Situ Control of 3D Orientations of Single AuNR@mSiO₂

3.1 High-throughput in-focus differential interference contrast imaging of three-dimensional orientations of single gold nanorods coated with a mesoporous silica shell

Geun Wan Kim,^{ab} Seokyoung Yoon,^c Jung Heon Lee^{*cd} and Ji Won Ha^{*ab}

A paper published in RSC Advances, **2020**, 10, 29868.

Reproduced by permission of the Royal Society of Chemistry (RSC)

*Corresponding author

3.1.1 Abstract

Plasmonic gold nanorods (AuNRs) have been widely applied as optical orientation probes in many biophysical studies. However, characterizing the various three-dimensional (3D) orientations of AuNRs in the same focal plane of the objective lens is a challenging task. To overcome this challenge, we fabricated single AuNRs (10 nm × 30 nm) coated with either an elliptical or spherical mesoporous silica shell (AuNRs@mSiO₂). Unlike bare AuNRs and elliptical AuNRs@mSiO₂, spherical AuNRs@mSiO₂ contained randomly oriented AuNR cores in 3D space, which could be observed on the same focal plane within a single frame by differential interference contrast (DIC) microscopy. The spherical AuNRs@mSiO₂ thus achieved high-throughput detection. The proposed approach can overcome the limitations of the current gel-matrix method, which requires vertical scanning of the embedded AuNRs

to capture different focal planes.

3.1.2 Introduction

Direct visualization and tracking with optical probes at high spatial and temporal resolution can reveal the complex dynamics and interactions in chemical and biological processes.¹⁻³ By investigating the rotational dynamics of nanoprobes, we can uncover a new dimension of information that is hidden in conventional three-dimensional (3D) single particle tracking. Recently, plasmonic anisotropic gold nanorods (AuNRs) have been popularized as orientation probes in single-particle rotational tracking because their shapes induce anisotropic optical properties,⁴⁻⁶ large scattering and absorption cross-sections,⁷ high photostability,⁸ and excellent biocompatibility.⁹⁻¹¹

Using polarization-based in-focus and defocused orientation imaging methods, researchers have determined the 3D orientations of individual AuNRs under dark-field (DF) microscopy,^{5, 12, 13} differential interference contrast (DIC) microscopy,^{6, 14, 15} and total internal reflection scattering (TIRS) microscopy.^{16, 17} Recently, interference-based DIC microscopy has detected the fast rotational motions of AuNRs with high temporal and spatial resolution in dynamic environments, such as complicated living cells. DIC microscopy is insensitive to the light scattered from the surrounding cellular components and maintains its high-throughput capability in live cell imaging. Sensitivity to scattered light is the main drawback of scattering-based DF and TIRS microscopes.^{4, 6}

Despite the recent advances in single-particle rotational tracking techniques, depositing and characterizing AuNRs with random 3D orientations on a glass slide on the same focal plane for DIC microscopy is a challenging task. Vertical scanning by the agarose gel-matrix method (or polyvinyl alcohol-matrix method) has characterized the out-of-plane spatial orientations of single AuNRs embedded with random 3D spatial distributions in a gel matrix.⁴ However, DIC microscopy can determine only the 3D orientations of the AuNRs on different focal planes as the sample is scanned along the z-axis.

In this study, we demonstrate that when deposited on a glass slide, single AuNRs (10 nm × 30 nm) inside a spherical mesoporous silica shell (AuNRs@mSiO₂) randomly orient on the same focal plane in 3D space.^{11, 18} Therefore, DIC microscopy can characterize the random orientations of single AuNRs@mSiO₂ with high-throughput on the same focal plane within a single frame. We demonstrate that DIC polarization anisotropy can effectively resolve the azimuthal angle φ of the AuNR cores inside the spherical silica shell. In comparison to the previous work using defocused DF microscopy based on a pattern matching method, DIC microscopy can provide faster and more accurate angular information of spherical AuNRs@mSiO₂ without sacrificing the much reduced signal intensity.¹⁸

3.1.3 Experimental Section

Materials and Chemicals

L-Ascorbic acid, silver nitrate (AgNO₃), sodium borohydride (NaBH₄),

sodium hydroxide (NaOH), 2,6-dihydroxybenzoic acid, tetraethyl orthosilicate (TEOS), gold chloride trihydrate ($\text{HAuCl}_4 \cdot 3\text{H}_2\text{O}$), cetyltrimethylammonium bromide (CTAB) were obtained from Sigma-Aldrich (St Louis, MO, USA). Gold nanorods (AuNRs, $25 \text{ nm} \times 73 \text{ nm}$) were purchased from Nanopartz (Loveland, CO, USA). Deionized water ($18.2 \text{ M}\Omega \text{ cm}$) was prepared by a Sartorius Arium®Pro Ultrapure water system. All glassware was cleaned using aqua regia. Special care has to be taken when researchers handle aqua regia.

Characterization of the Synthesized AuNRs@mSiO₂

We used transmission electron microscope (TEM, JEL-2100F, JEOL, Japan) and scanning electron microscope (SEM, JSM6500, JEOL, Japan) to characterize the AuNRs@mSiO₂. The TEM images were analyzed based on a custom MATLAB script previously reported with some subroutine implemented in the image processing toolbox of MATLAB. Furthermore, a Varian Carry 300 UV-vis spectrometer (Agilent Technologies) was used to characterize the ensemble extinction spectrum of the AuNRs@mSiO₂.

Sample Preparation for Single Particle Study

The samples for single particles studies were prepared as follows: the colloid solution was first diluted with 18.2 MU pure water to a proper concentration. The diluted solution was then sonicated for 10 min at room temperature. Samples were prepared by drop casting the diluted AuNRs@mSiO₂ solution on pre-cleaned glass

slides. Subsequently, a 22 mm × 22 mm No. 1.5 coverslip (Corning, NY, USA) was placed on the glass slide. Throughout all of the experiments, the concentration of AuNRs@mSiO₂ deposited on the glass slide surface was maintained at about 1 mm⁻² to facilitate single particle characterization without inter-particle interaction and LSPR coupling.

Differential Interference Contrast Microscopy

We performed DIC microscopy using a Nikon inverted microscope (ECLIPSE Ti-U, JAPAN). DIC microscopy consists of a set of two Nomarski prisms, two polarizers, and a quarter-waveplate. We illuminated the samples by an oil immersion condenser with a NA of 1.4. The DIC signals coming from the sample were collected by a Plan Apo oil-immersion objective (100× NA = 1.4). To obtain DIC images with high quality, we used an Andor EMCCD camera (iXon Ultra 897, UK). We then used Image J and Matlab to analyze the collected DIC images.

3.1.4 Result and Discussion

Elliptical and spherical AuNRs@mSiO₂ particles were fabricated by a slightly modified literature protocol,^{19,20} and were structurally characterized by TEM and SEM. **Fig. 17A** is a TEM image of the synthesized AuNRs with an average length and diameter of 30 nm and 10 nm, respectively. Elliptical (thin shell) or spherical (thick shell) mesoporous silica was coated on the AuNRs by the above-mentioned modified method (**Fig. 17B and C**).^{19,20} The elliptical mesoporous silica shell was 31.7(±4.8)

nm thick, while the spherical mesoporous silica shell was $52.7(\pm 5.7)$ nm thick (**Fig. 17B and C**). We then obtained the UV-vis absorption spectra of the AuNRs and AuNRs@mSiO₂ (elliptical and spherical) dispersed in water (**Fig. 17D**). The longitudinal surface plasmon resonance (LSPR) peaks of the naked AuNRs and the spherical AuNRs@mSiO₂ appeared at 769 and 794 nm, respectively. The red shift in the latter LSPR peak was caused by the mesoporous silica shell coating.

Thus far, AuNRs have been randomly oriented in 3D space by embedding them in agarose gel matrix. The 3D orientations must then be determined on successive focal planes by scanning along the z-axis (Fig. S3). However, the gel-matrix method is time consuming, cumbersome, and inconvenient for a 360° rotational study. Furthermore, LSPR coupling can occur among adjacent AuNRs, causing a spectral shift in single-particle characterization.

In our spherical AuNRs@mSiO₂ fabrication, LSPR coupling between two adjacent AuNRs is prevented by the outer shell, which is advantageous for single-particle spectroscopic characterization (**Fig. 17C**). However, the silica shell can block the interaction of AuNRs with the medium. Furthermore, during the drop-casting for sample preparation, the naked AuNRs were deposited parallel to the glass slide, so were tilted by almost the same angle from the glass surface (**see Fig. 18A**). The elliptical AuNRs@mSiO₂ with the thin silica shell were also tilted at very similar angles, with low degrees of freedom in the z-direction (**Fig. 18B**). In contrast, within the silica shells of the spherical AuNRs@mSiO₂ deposited on the glass slide, the AuNR cores were randomly oriented on the same focal plane (**Fig. 18C**), with different

projected lengths. As shown in **Fig. 17C and 19A**, the 3D orientations of the AuNRs in the shells influenced the projected lengths of the AuNRs. This situation completely differed from that of bare AuNRs (**Fig. 17A**). The random 3D orientations of many AuNRs in the silica shell were further verified by TEM (**see Fig. 19B**).

We then investigated the spatial orientations of single AuNR (10 nm × 30 nm) cores in the silica shell by DIC microscopy. As an interferometry-based technique, DIC microscopy resolves the optical path difference between two orthogonally polarized beams (B1 and B2, designating the bright and dark axes, respectively) separated by a Nomarski prism (**Fig. 3**). The azimuthal angle (φ) and polar angle (θ) of the AuNR core are defined in **Fig. 6B**. The DIC captured single spherical AuNRs@mSiO₂ particles in the same focal plane at their LSPR wavelength (i.e., at 750 nm) (**Fig. 19C**). It should be noted that in DIC microscopy, the different bright and dark patterns correspond to different in-plane orientations of the AuNR cores deposited on the glass slide. Therefore, we could achieve high-throughput, high-contrast DIC imaging of spherical AuNRs@mSiO₂ particles with various orientations within a single image frame.

The polarization dependency of the spherical AuNRs@mSiO₂ imaging was measured at their LSPR wavelength (750 nm) on a rotational stage moved from 0° to 360° at 10° increments. **Fig. 20A** is a DIC image of two spherical AuNRs@mSiO₂ particles labeled AuNR1@mSiO₂ and AuNR2@mSiO₂ measured at 750 nm. As shown in **Fig. 20B**, the DIC images of AuNR1@mSiO₂ periodically changed as the rotation angle increased. In addition, the bright and dark intensities of AuNR1@mSiO₂

were periodic functions of rotation angle and were anti-correlated at both LSPR wavelengths (769 and 794 nm), informing that when the dark intensity decreases, the bright intensity increases (**Fig. 20C**). In this study, the measured dark and bright values consist of the darkest and brightest pixels within a region around a particle, respectively. The bright and dark intensities at each LSPR wavelength were well fitted to $\sin^4(\varphi)$ and $\cos^4(\varphi)$ functions, respectively. More specifically, the orthogonally polarized bright and dark intensities of AuNR@mSiO₂ are given by^{12, 18}

$$\begin{aligned} I_B &\propto \sin^4(\varphi)\sin^2(\theta) \\ I_D &\propto \cos^4(\varphi)\cos^2(\theta) \end{aligned} \quad (4)$$

According to Eq. (4), the AuNR orientations are directly determinable from the bright and dark intensities of the polarized DIC images. In practice, however, the precision might be affected by intensity fluctuations of the light source, focus-drift in the vertical direction, and other disturbances. This limitation can be overcome by the DIC polarization anisotropy P , defined by Eq. (5).^{6, 14} The DIC polarization anisotropy P can be conveniently computed from the bright and dark intensities of AuNR@mSiO₂:

$$P = \frac{I_{B,N} - I_{D,N}}{I_{B,N} + I_{D,N}} \quad (5)$$

Here, $I_{B,N}$ and $I_{D,N}$ are the normalized bright and dark intensities at the LSPR wavelengths, respectively. As the polarization direction increased from 0 to 360, the DIC polarization anisotropy of the AuNR1@mSiO₂ varied between -1.0 (AuNRs alignment along the dark axis, $\varphi = 0^\circ$ or 180°) and 1.0 (AuNR alignment along the bright axis, $\varphi = 90^\circ$ or 270°) (**see Fig. 20D**). Being based on the intensity ratio rather

than the absolute intensities, the DIC polarization anisotropy is resistant to intensity instabilities and provides reliable and accurate angle measurements.¹⁴ Moreover, the DIC polarization anisotropy depends only on the azimuthal angle φ , and not on the polar angle θ of the AuNRs.⁶ After determining the azimuthal angle φ of AuNRs@mSiO₂ by DIC polarization anisotropy, we can determine their polar angles θ by Eq. (4).

Next, we compared the polarization angles of the spherical AuNRs@mSiO₂ and the elliptical AuNRs@mSiO₂ with the thin silica shell. The polarization angles of the elliptical AuNRs@mSiO₂ particles were measured at their LSPR wavelength (750 nm) on a rotational stage shifted at 10° increments from 0° to 360°. **Fig. S4** shows the DIC images of the elliptical AuNR1@mSiO₂ measured at their LSPR wavelength at different rotation angles. Again, the bright and dark intensities of the elliptical AuNR1@mSiO₂ were periodic functions of rotational angle (**Fig. S5A**), and the measured DIC polarization anisotropy values well agreed with the calculated values (**Fig. S5B**). After determining the azimuthal angle φ of the elliptical AuNRs@mSiO₂ by DIC polarization anisotropy, we determined their polar angles θ . As shown in **Fig. 21A**, the polar angles θ of the AuNR cores inside the elliptical silica shell varied between 60° and 90°. In addition, the polar angles θ of bare AuNRs without the shell also varied between 60° and 90°. However, the AuNR cores inside the spherical silica shells were distributed over a wider range (0°–90°, see **Fig. 21B**) because more degrees of freedom, especially in the vertical direction, were available to the AuNRs in the spherical shells.

Finally, to clearly demonstrate the advantage of the spherical AuNRs@mSiO₂ fabrication over the conventional gel-matrix method, we imaged tilted AuNRs (of average size 25 nm × 73 nm) embedded in a 2% agarose gel matrix. DIC images of AuNRs were obtained by scanning along the z-direction with a vertical step size of 40 nm (**Fig S6**). **Fig. S6** shows consecutive DIC images of the AuNRs with random 3D orientations in the gel matrix, obtained on different focal planes. The different focal planes of the AuNRs in the gel matrix are clarified in **Fig. S6**. This result confirms that without vertical scanning, DIC microscopy cannot observe the random spatial orientations of the AuNRs in the standard gel-matrix embedding. In contrast, the spherical AuNRs@mSiO₂ enables a high-throughput determination of the 3D orientations of the AuNR cores in the silica shell on a single focal plane of the objective; moreover, it prevents LSPR coupling among the nanoparticles.

3.1.5 Conclusion

In summary, the spatial orientations of single AuNRs (10 nm × 30 nm) coated with mesoporous silica shell (AuNRs@mSiO₂) were observed by DIC microscopy. The silica shell prevented LSPR coupling among the AuNR cores. Unlike the bare AuNRs and elliptical AuNRs@mSiO₂, spherical AuNRs@mSiO₂ deposited on a glass slide allowed random 3D orientations of the AuNR cores on the same focal plane. These orientations were detected with high-throughput and high-contrast efficacy within a single frame. Our approach newly characterizes the 3D random orientations and polarization dependences of AuNRs on the same focal plane by DIC microscopy.

The main limitation of the gel-matrix method, namely, the need for observing many focal planes along the z-direction, is thereby removed.

3.1.6 References

1. Zhuang, X.; Bartley, L. E.; Babcock, H. P.; Russell, R.; Ha, T.; Herschlag, D.; Chu, S., A single-molecule study of RNA catalysis and folding. *Science* **2000**, 288 (5473), 2048-51.
2. Nishizaka, T.; Oiwa, K.; Noji, H.; Kimura, S.; Muneyuki, E.; Yoshida, M.; Kinosita, K., Chemomechanical coupling in F1-ATPase revealed by simultaneous observation of nucleotide kinetics and rotation. *Nature Structural & Molecular Biology* **2004**, 11 (2), 142-148.
3. Toprak, E.; Enderlein, J.; Syed, S.; McKinney, S. A.; Petschek, R. G.; Ha, T.; Goldman, Y. E.; Selvin, P. R., Defocused orientation and position imaging (DOPI) of myosin V. *Proceedings of the National Academy of Sciences* **2006**, 103 (17), 6495-6499.
4. Xiao, L.; Ha, J. W.; Wei, L.; Wang, G.; Fang, N., Determining the Full Three-Dimensional Orientation of Single Anisotropic Nanoparticles by Differential Interference Contrast Microscopy. *Angewandte Chemie International Edition* **2012**, 51 (31), 7734-7738.
5. Sönnichsen, C.; Alivisatos, A. P., Gold Nanorods as Novel Nonbleaching Plasmon-Based Orientation Sensors for Polarized Single-Particle Microscopy. *Nano Letters* **2005**, 5 (2), 301-304.
6. Ha, J. W.; Sun, W.; Stender, A. S.; Fang, N., Dual-Wavelength Detection of Rotational Diffusion of Single Anisotropic Nanocarriers on Live Cell Membranes. *The Journal of Physical Chemistry C* **2012**, 116 (4), 2766-2771.

7. and, S. L.; El-Sayed, M. A., Optical Properties and Ultrafast Dynamics of Metallic Nanocrystals. *Annual Review of Physical Chemistry* **2003**, *54* (1), 331-366.
8. Chang, W.-S.; Ha, J. W.; Slaughter, L. S.; Link, S., Plasmonic nanorod absorbers as orientation sensors. *Proceedings of the National Academy of Sciences* **2010**, *107* (7), 2781-2786.
9. Murphy, C. J.; Gole, A. M.; Stone, J. W.; Sisco, P. N.; Alkilany, A. M.; Goldsmith, E. C.; Baxter, S. C., Gold Nanoparticles in Biology: Beyond Toxicity to Cellular Imaging. *Accounts of Chemical Research* **2008**, *41* (12), 1721-1730.
10. Yoon, S.; Chang, J.; Kwon, N.; Moon, S.; Park, Y.; Han, K. H.; Lim, B.; Lee, J. H., Multifunctional Nanomaterial-alginate Drug Delivery and Imaging System for Cancer Therapy. *BioChip Journal* **2019**, *13* (3), 236-242.
11. Yoon, S.; Chung, Y.; Lee, J. W.; Chang, J.; Han, J. G.; Lee, J. H., Biologically Benign Multi-functional Mesoporous Silica Encapsulated Gold/Silver Nanorods for Anti-bacterial Applications by On-demand Release of Silver Ions. *BioChip Journal* **2019**, *13* (4), 362-369.
12. Xiao, L.; Qiao, Y.; He, Y.; Yeung, E. S., Three Dimensional Orientational Imaging of Nanoparticles with Darkfield Microscopy. *Analytical Chemistry* **2010**, *82* (12), 5268-5274.
13. Lee, S. Y.; Tsalu, P. V.; Kim, G. W.; Seo, M. J.; Hong, J. W.; Ha, J. W., Tuning Chemical Interface Damping: Interfacial Electronic Effects of Adsorbate Molecules and Sharp Tips of Single Gold Bipyramids. *Nano Letters* **2019**, *19* (4), 2568-2574.

14. Won Ha, J.; Sun, W.; Wang, G.; Fang, N., Differential interference contrast polarization anisotropy for tracking rotational dynamics of gold nanorods. *Chemical Communications* **2011**, *47* (27), 7743-7745.
15. Lee, S. Y.; Han, Y.; Hong, J. W.; Ha, J. W., Single gold bipyramids with sharp tips as sensitive single particle orientation sensors in biological studies. *Nanoscale* **2017**, *9* (33), 12060-12067.
16. Ha, J. W.; Marchuk, K.; Fang, N., Focused Orientation and Position Imaging (FOPI) of Single Anisotropic Plasmonic Nanoparticles by Total Internal Reflection Scattering Microscopy. *Nano Letters* **2012**, *12* (8), 4282-4288.
17. Marchuk, K.; Fang, N., Three-Dimensional Orientation Determination of Stationary Anisotropic Nanoparticles with Sub-Degree Precision under Total Internal Reflection Scattering Microscopy. *Nano Letters* **2013**, *13* (11), 5414-5419.
18. Kim, G. W.; Yoon, S.; Lee, J.; Lee, J. H.; Ha, J. W., High-Throughput Characterization and In Situ Control of Three-Dimensional Orientations of Single Gold Nanorods Coated with Spherical Mesoporous Silica Shell. *The Journal of Physical Chemistry C* **2020**, *124* (26), 14279-14286.
19. Yoon, S.; Lee, B.; Kim, C.; Lee, J. H., Controlled Heterogeneous Nucleation for Synthesis of Uniform Mesoporous Silica-Coated Gold Nanorods with Tailorable Rotational Diffusion and 1 nm-Scale Size Tunability. *Crystal Growth & Design* **2018**, *18* (8), 4731-4736.
20. Gorelikov, I.; Matsuura, N., Single-Step Coating of Mesoporous Silica on Cetyltrimethyl Ammonium Bromide-Capped Nanoparticles. *Nano Letters* **2008**, *8* (1),

369-373.

3.1.7 Figures and Captions

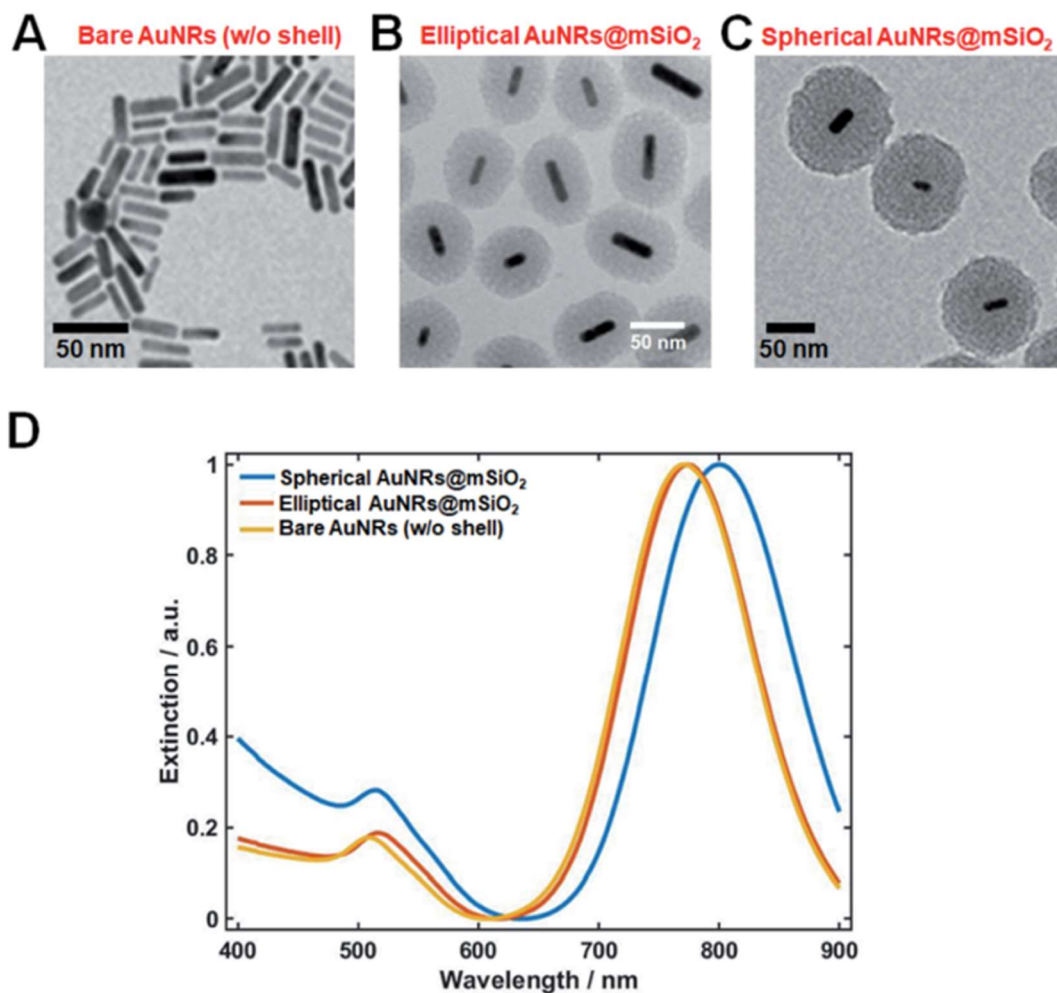


Figure 17. (A–C) TEM images of (A) bare AuNRs, (B) elliptical AuNRs@mSiO₂ (red curve), and (C) spherical AuNRs@mSiO₂ (blue curve). (D) Overlaid UV-vis extinction spectra of bare AuNRs (yellow curve), elliptical AuNRs@mSiO₂ (red curve), and spherical AuNRs@mSiO₂ (blue curve). The anisotropic AuNRs yielded two distinct LSPR peaks.

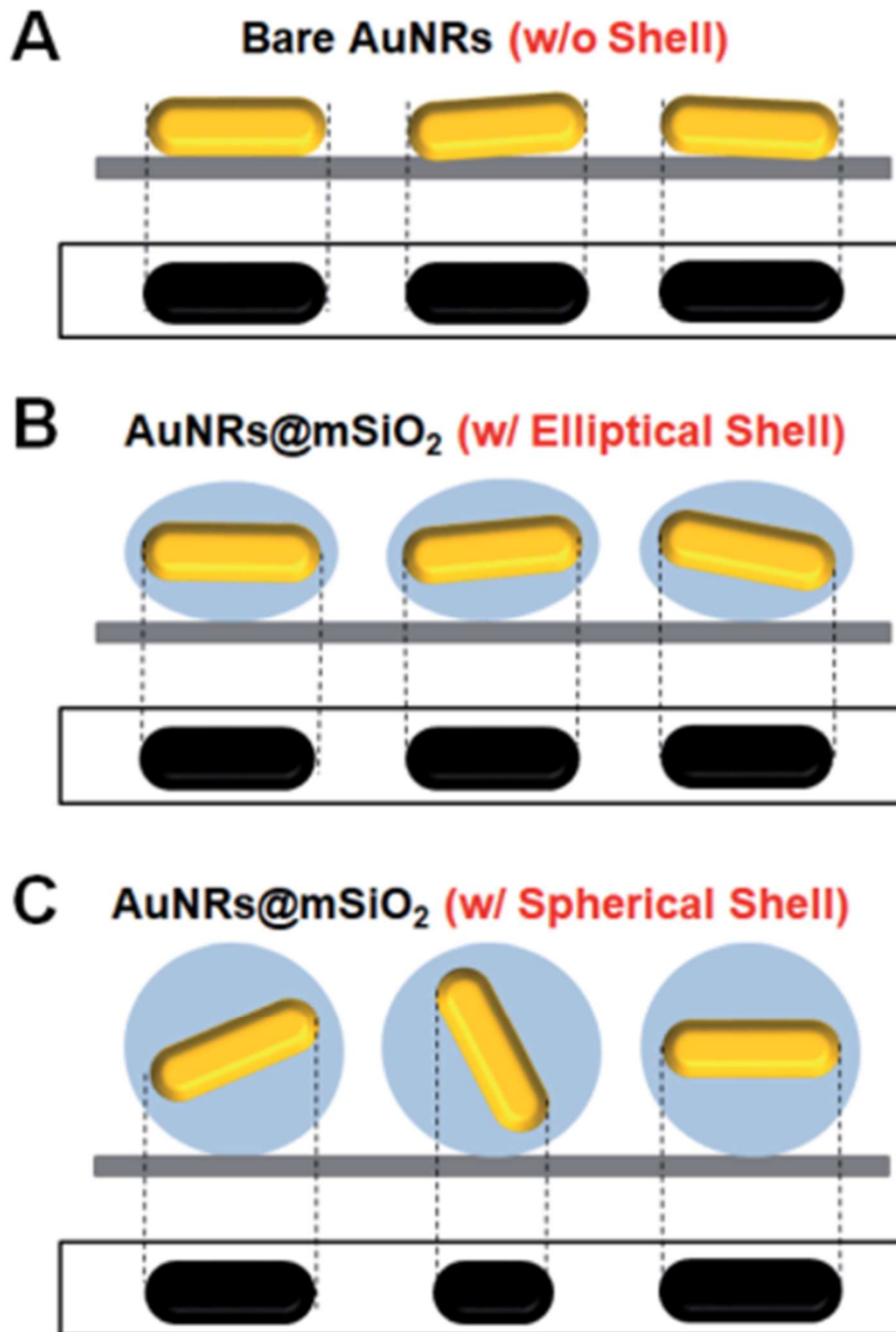


Figure 18. (A) Schematic of bare AuNRs deposited on a glass slide. Their projected lengths are almost the same. (B) Schematic of elliptical AuNRs@mSiO₂ particles and their projections on a glass slide. (C) Schematic of spherical AuNRs@mSiO₂ particles with their AuNR cores randomly oriented in the shell. Their projected lengths depend on their spatial orientations, which are freely available in 3D space.

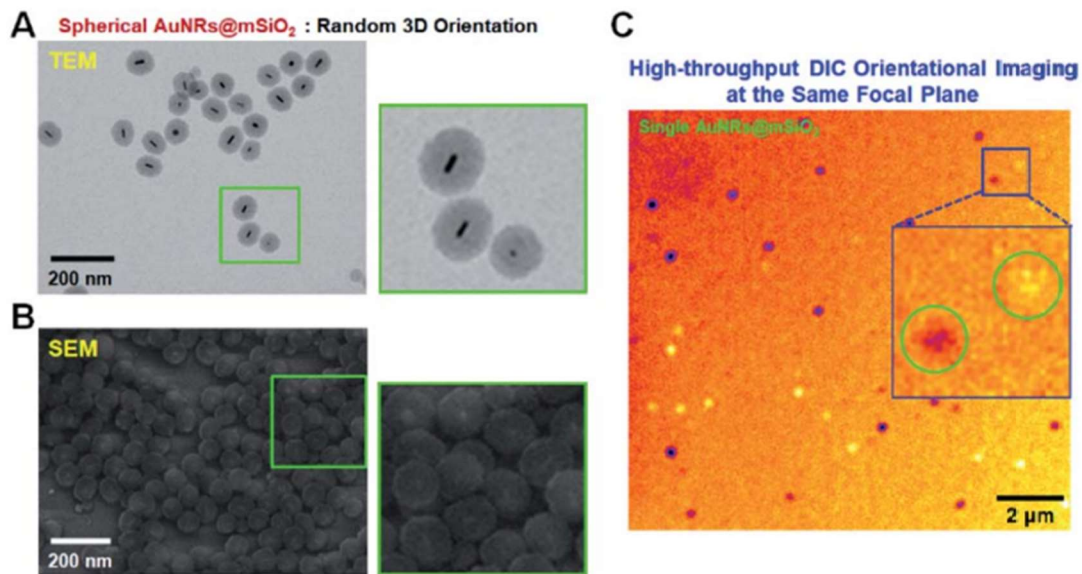


Figure 19. (A) TEM image of spherical AuNRs@mSiO₂ with randomly oriented AuNR cores inside the silica shell. (B) SEM image of spherical AuNRs₂ particles, and (C) DIC image of AuNRs@mSiO₂ particles, showing their different orientations on the same focal plane. The color image was generated in ImageJ for better demonstration of bright and dark DIC images of AuNRs@mSiO₂. Note that high-throughput detection is possible.

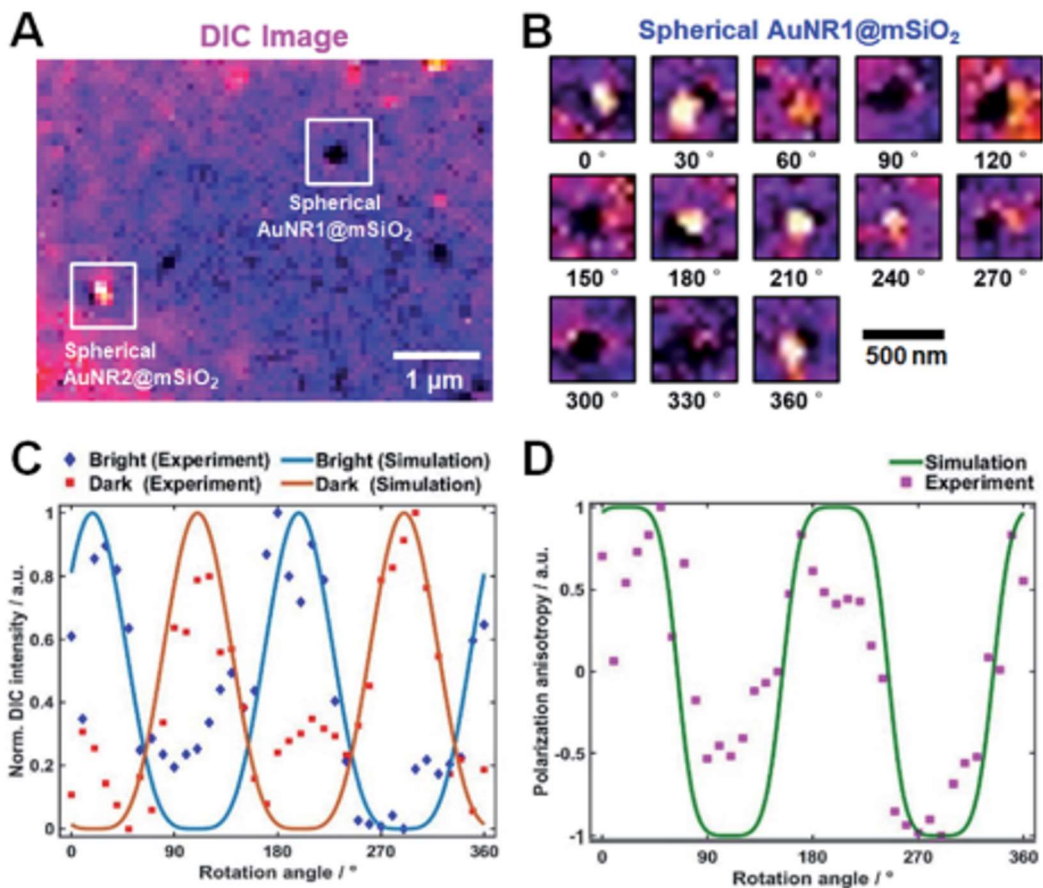


Figure 20. (A) DIC image of spherical AuNRs@mSiO₂. (B) DIC images of spherical AuNR1@mSiO₂ captured at different rotational angles (interval $\frac{1}{4}$ 30°). (C) Dark and bright intensities of spherical AuNR1@mSiO₂ as functions of rotation angle. (D) DIC polarization anisotropy computed from the dark and bright intensities of the spherical AuNR1@mSiO₂.

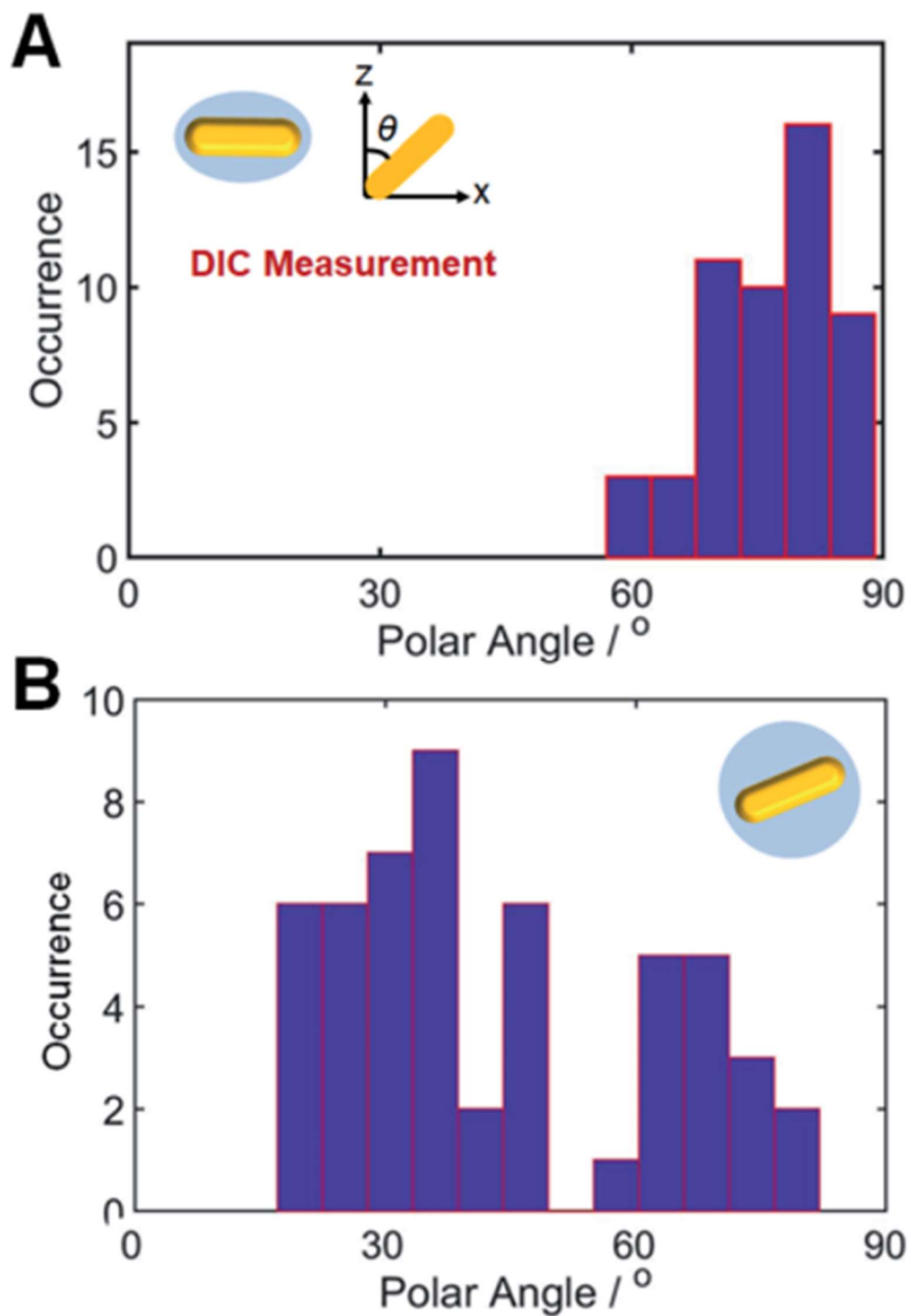


Figure 21. Histograms showing the polar angle (θ) distributions of (A) elliptical AuNRs@mSiO₂ and (B) spherical AuNRs@mSiO₂, determined from the DIC measurements.

3.1.7 Supplementary Materials

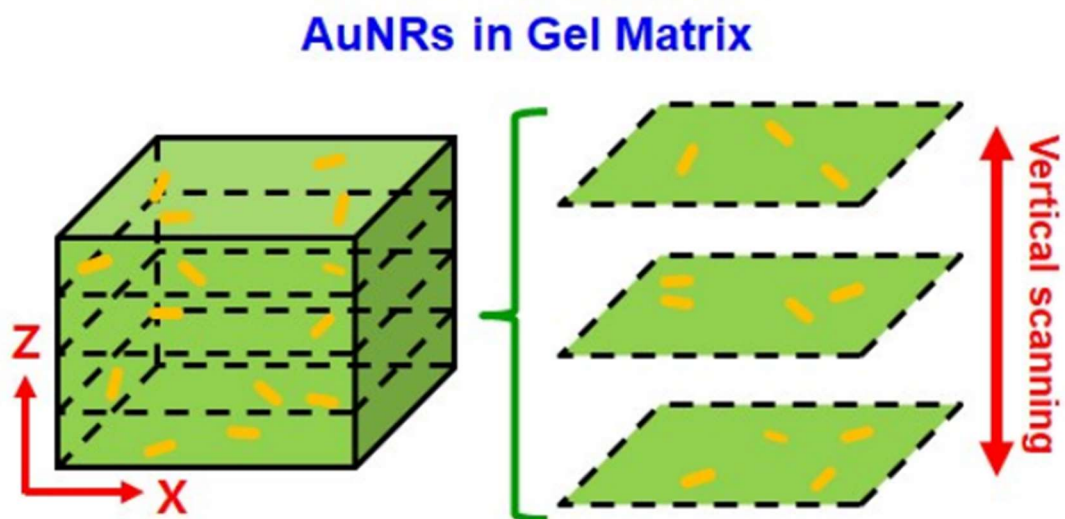


Figure S3. Schematic to show AuNRs embedded in a gel matrix at the different focal planes. The embedded AuNRs are measured by vertical scanning in the z-axis under DIC microscopy.

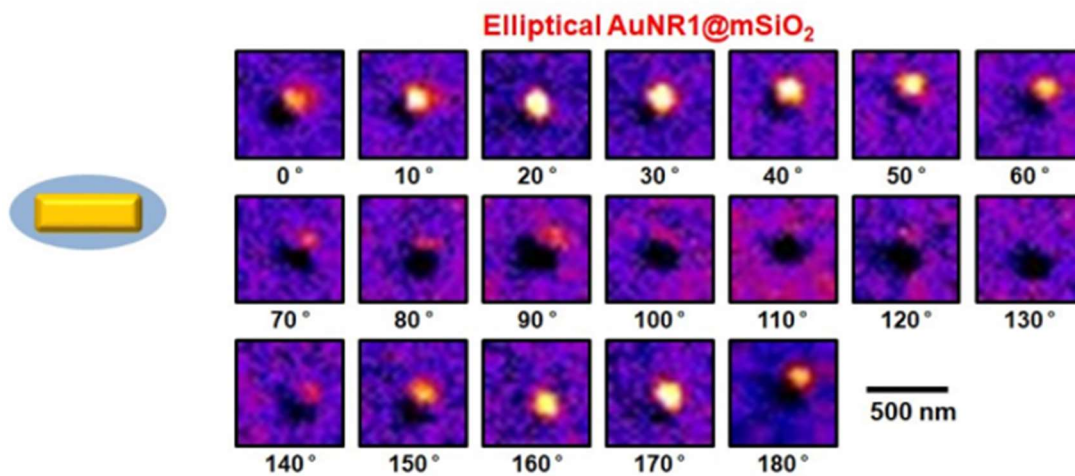


Figure S4. DIC images of elliptical AuNR1@mSiO₂ as a function of rotational angle with 10° increment from 0° to 180°.

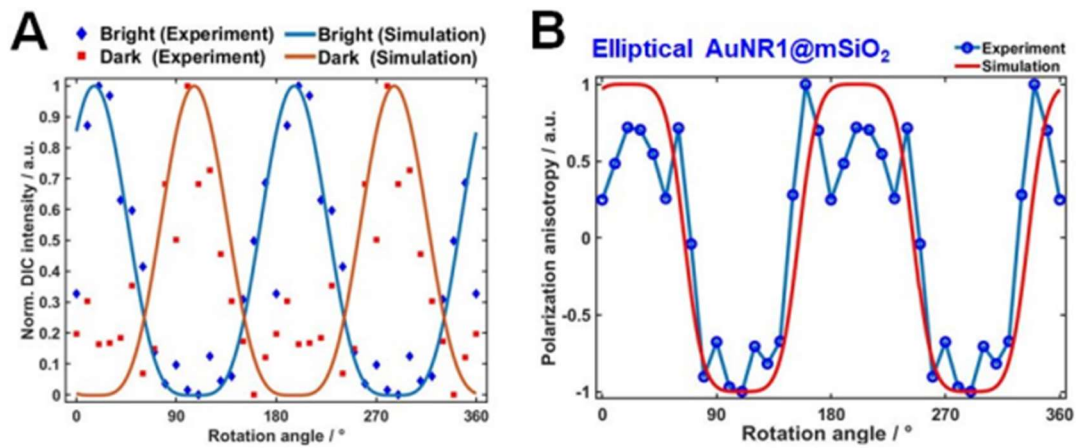


Figure S5. (A) Normalized DIC intensities of elliptical AuNR1@mSiO₂ in Fig. S4 as a function of rotational angle. (B) Change in the DIC polarization anisotropy calculated from two dark and bright intensities in (A) for the elliptical AuNR1@mSiO₂.

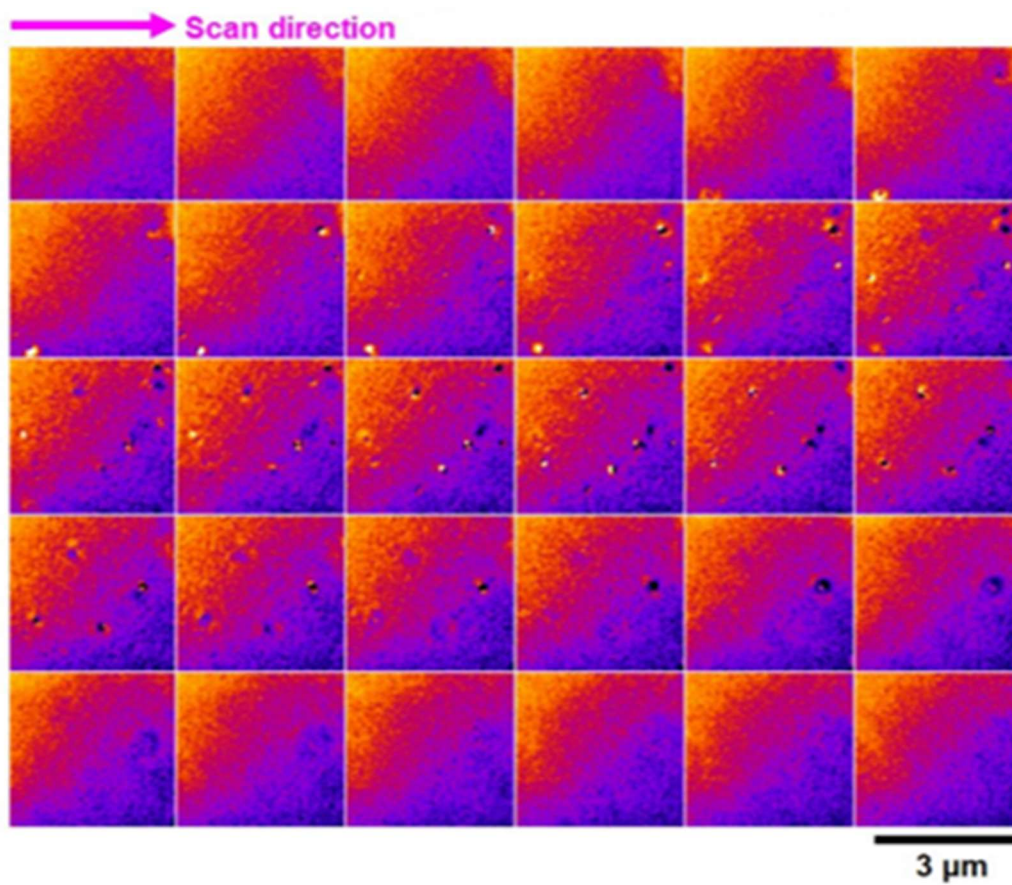


Figure S6. Consecutive DIC images of the embedded AuNRs ($25 \text{ nm} \times 73 \text{ nm}$) measured by z-axis scanning with a vertical step size of 40 nm. The AuNRs in gel matrix have random 3D orientations at the different focal planes.

3.2 High-Throughput Characterization and In Situ Control of Three-Dimensional Orientations of Single Gold Nanorods Coated with Spherical Mesoporous Silica Shell

Geun Wan Kim, Seokyoung Yoon, Jaeran Lee, Jung Heon Lee* and Ji Won Ha*

A paper published in The Journal of Physical Chemistry C, **2020**, 124, 14279-14286.

Reproduced by permission of the American Chemical Society (ACS)

*Corresponding author

3.2.1 Abstract

Anisotropic gold nanorods (AuNRs) are widely used as orientation probes in many biological and physical studies. However, the in-situ control of the spatial orientation of AuNRs having various three-dimensional (3D) orientations at the same focal plane of the objective lens still remains a challenge. Herein, we employ a defocused dark-field (DF) microscope for the high-throughput determination of the random 3D orientations of core AuNRs (10 × 30 nm) coated with spherical-shaped mesoporous silica shell (AuNRs@mSiO₂) at the same focal plane within a single frame. This method overcomes the conventional gel matrix method based on vertical scanning of embedded AuNRs. Furthermore, by taking advantage of the spherical shape of the AuNRs@mSiO₂, in situ variation of the tilting angles of the core AuNRs is achieved by inducing the movement of the AuNRs@mSiO₂ through applying an external fluidic force in a flow cell. We therefore demonstrate the direct visualization and real-time tracking of the azimuthal and polar angles of tilted AuNR cores moving on a glass slide under defocused DF microscopy without angular degeneracy

3.2.2 Introduction

Plasmonic anisotropic gold nanorods (AuNRs) have unique size- and shape-induced optical properties resulting from localized surface plasmon resonance (LSPR).¹⁻³ In addition, the optical properties of AuNRs are strongly influenced by their three-dimensional (3D) orientations and interparticle distances.⁴⁻⁶ In this regard, precise control of the orientation and the position of single AuNRs by an external force is important for characterizing and tuning their optical properties and for enhancing their applicability in physical and biological sciences.^{4, 7} The external forces can be osmotic pressure, capillary,⁸ mechanical,^{9, 10} electric and magnetic,¹¹ and so forth.

Besides the manipulation of nanoparticles by external forces, it is also important to determine and monitor their spatial orientations and position under optical microscopy. So far, a few optical imaging methods have been reported to resolve the 3D orientation of individual AuNRs, including dark-field (DF) polarization microscopy,¹²⁻¹⁴ photothermal heterodyne imaging (PHI),^{15, 16} differential interference contrast (DIC) polarization anisotropy,¹⁷⁻¹⁹ and total internal reflection scattering microscopy.^{20, 21} Furthermore, defocused orientation and position imaging (DOPI) techniques have been reported to allow determining the spatial orientation of out-of-focus AuNR without angular degeneracy.^{12, 22-25} However, with the current optical techniques, only the in-plane orientation is effectively revealed, whereas the accurate full 3D orientations of single AuNRs in the four quadrants of the Cartesian plane are only partially attainable. In this regard, further systematic fundamental studies that lead to the development of enhanced methods to characterize random 3D orientations

of single AuNRs are still required in far-field optical microscopy.

To date, the agarose gel matrix method based on vertical scanning by optical imaging has been mostly used for the characterization of the out-of-plane spatial orientations and optical properties of single AuNRs with random 3D spatial distributions embedded in a gel matrix.²⁶ For example, Xiao et al. conducted a DIC rotational study that combines DIC image pattern recognition with DIC polarization anisotropy for determining the 3D orientations of AuNRs embedded in the gel matrix.²⁶ However, the gel matrix method presents a major disadvantage: z-axis scanning is required to analyze the 3D orientations and the corresponding optical properties of the AuNRs at different focal planes, which is time-consuming, cumbersome, and difficult for a rotational study. Furthermore, it is also challenging to change the 3D orientations and position of the AuNRs fixed inside the gel matrix for further in situ characterization.

In the present study, we report a novel method to analyze random 3D orientations of single AuNRs inside a spherical silica shell (AuNRs@mSiO₂) at the same focal plane, which overcomes the conventional gel matrix method. We demonstrate that the 3D orientation of a single AuNR core can be directly resolved with high throughput in the focal plane of the objective using a single frame by using a defocused DF microscope. Moreover, we present that the in-situ control and variation of the spatial orientation of the AuNR core can be achieved by inducing the rolling of the spherical AuNRs@mSiO₂ with an external fluidic force in a flow cell.

3.2.3 Experimental Section

Materials and Chemicals

L-Ascorbic acid, silver nitrate (AgNO_3), sodium borohydride (NaBH_4), sodium hydroxide (NaOH), 2,6-dihydroxybenzoic acid, tetraethyl orthosilicate (TEOS), gold chloride trihydrate ($\text{HAuCl}_4 \cdot 3\text{H}_2\text{O}$), and cetyltrimethylammonium bromide (CTAB) were obtained from Sigma-Aldrich (St. Louis, MO, USA). AuNRs (25×73 nm) were purchased from Nanopartz (Loveland, CO, USA). Deionized water ($18.2 \text{ M}\Omega \text{ cm}$) was prepared by a Sartorius Arium®Pro Ultrapure water system. All glassware was cleaned using aqua regia. Special care has to be taken when researchers handle aqua regia.

Preparation of Gold Nanorods

The AuNRs (10×30 nm) were synthesized on the basis of a previously reported method.²⁷ The stock solution as seed was synthesized by mixing 250 μL of 10 mM HAuCl_4 with 7.5 mL of 100 mM CTAB solution. Then 10 mM NaBH_4 solution was prepared as reductant with fresh ice-cold water. Six hundred microliters of reducing solution were injected into the above gold and CTAB mixture under vigorous stirring for 2 min. After that, seed solution was aged for 1 h under room temperature and undisturbed conditions. For further growth of seed, we used aromatic additives, 2,6-dihydroxybenzoic acid. The growth solution was prepared by mixing 24 mL of 100 mM CTAB solution with 2 mL of 67 mM 2,6-dihydroxybenzoic acid solution. After complete dissolution of 2,6-dihydroxybenzoic acid solution, 170 μL of 10 mM

AgNO₃ solution and 1 mL of 10 mM HAuCl₄ solution were added into the growth solution, respectively, and stirred for 10 min. Subsequently, 140 μL of 100 mM L-ascorbic acid solution were added. Finally, 600 μL of the above seed solution was added into the growth solution. The final mixture was stirred for 30 s and left undisturbed at 27 °C for 12 h. The synthesized AuNRs were washed to remove excessive surfactant and unreacted chemicals using a centrifuge.

Preparation of Gold Nanorods Encapsulated with Mesoporous Silica

Mesoporous silica coating on AuNRs was performed according to the previously reported method with slight modification.^{28,29} The proper concentration for the encapsulation is as follows: the concentrations of AuNRs and CTAB were 1.2 nM and 1.2 mM, respectively. The mesoporous silica shell coating was conducted under basic conditions to induce a sol–gel reaction. The 30 μL of 100 mM NaOH solution was added into 10 mL of the above gold nanorod solution. After 15 min, 20 μL of 20 v/v % TEOS diluted with methanol was added 10 times at 1 h intervals under magnetic stirring. Subsequently, another 30 μL of 100 mM NaOH solution was added and 20 μL of 20 v/v % TEOS diluted with methanol was added 10 times more. The mixture was aged for 24 h and washed three times with ethanol using a centrifuge. The concentration of AuNRs was measured as previously reported.³⁰

Structural Characterization and UV–Vis Extinction Measurement

Structural characterizations of AuNRs@mSiO₂ were carried out using a

transmission electron microscope (TEM) (H-8100, Hitachi, Japan) and a scanning electron microscope (SEM) (JSM6500F, JEOL, Japan). Furthermore, the heterogeneous localized surface plasmon resonance (LSPR) ensemble extinction spectra of AuNRs and AuNRs@mSiO₂ dispersed in water were recorded with a Varian Carry 300 UV–vis spectrometer (Agilent Technologies).

Sample Preparation for Single-Particle Spectroscopy

The sample for single-particle spectroscopy was prepared by drop-casting the AuNR@mSiO₂ solution onto a precleaned glass slide. The concentration of AuNRs@mSiO₂ drop-cast onto the glass surface was controlled at 1 μm⁻² to facilitate single-particle characterization. However, the spherical outer shell of the AuNRs@mSiO₂ allows us to avoid the LSPR coupling between two adjacent AuNRs, which is advantageous for single-particle spectroscopic characterization.

Single-Particle Scattering Microscopy and Spectroscopy

DF microscopy imaging was performed under a Nikon inverted microscope (ECLIPSE Ti-U). In DF mode, the microscope utilized a Nikon Plan Fluor 100× 0.5–1.3 oil iris objective and a Nikon DF condenser. An Andor iXon^{EM+} CCD camera (iXon Ultra 897) was used to record the DF images of the AuNRs@mSiO₂. The collected images were analyzed using ImageJ. DF scattering spectra were acquired with an Andor spectrophotometer (SHAMROCK 303i, SR-303I-A) connected to an Andor CCD camera (Newton DU920P-OE). When the spectrum is obtained, the

scanning stage moved the sample to the desired location so that only scattered light from the selected location was collected by the objective. The scattered light was directed to the entrance of the spectrophotometer, dispersed by grating (300 l/mm), and detected by the Newton CCD camera. The background was measured in a region without any particles. Data analysis was performed with specially designed Matlab programs

3.2.4 Result and Discussion

Spherical AuNRs@mSiO₂ were selected for the present study for two important reasons: First, the spherical outer shell of the AuNRs@mSiO₂ allows us to avoid the LSPR coupling between two adjacent AuNRs, which is advantageous for single-particle spectroscopic characterization. Second, AuNRs without the silica shell are deposited parallel to a glass slide when drop-casted for sample preparation, thus having almost the same tilting angle from the glass slide as depicted in **Fig. 22A**. In contrast, when spherical AuNRs@mSiO₂ are deposited on a glass slide, random 3D orientations of the AuNR core inside the silica shell in the same focal plane of the objective are expected (**Fig. 22B**).

In this study, spherical AuNRs@mSiO₂ were synthesized following a slightly modified literature protocol,^{28, 29} and structural characterizations were carried out by transmission electron microscopy (TEM) and scanning electron microscopy (SEM). **Fig. 22C** shows a TEM image of the synthesized AuNRs having an average length and diameter of 30 and 10 nm, respectively. Then spherical mesoporous silica was coated

on the AuNRs according to the same modified method (**Fig. 22D**).^{28, 29} The thickness of the spherical mesoporous silica shell was estimated to be about 30 nm, as shown in **Fig. 22D**. We then obtained the UV–vis absorption spectra of both AuNRs and AuNRs@mSiO₂ dispersed in water (**Fig S7**). The longitudinal LSPR peak of AuNRs without silica shell appeared at 771 nm, whereas that of the AuNRs@mSiO₂ appeared at 800 nm because the red shift in the LSPR peak of the latter resulted from the mesoporous silica shell coating.

First of all, to determine whether the AuNRs were randomly oriented in the silica shell as mentioned above, we analyzed the TEM images on the basis of a custom MATLAB script previously reported with a subroutine implemented in the image-processing toolbox of MATLAB.²⁷ As shown in **Fig. 22D**, a length of the projected AuNRs in the silica shell varied depending on their spatial 3D orientations, which contrasts with the image of bare AuNRs depicted in **Fig. 22C**. To perform a statistical TEM image analysis, we measured many AuNRs for each sample and analyzed their length and diameter with a custom MATLAB program. As clearly seen in **Fig. 23**, the projected TEM images of the spherical AuNRs@mSiO₂ showed greater variations of their length and diameter than those of the AuNRs without the shell. More specifically, the average major (or longitudinal axis) length of bare AuNRs is longer than that of AuNRs@mSiO₂. However, the average minor (or transverse axis) length is not that much different, which indicates that AuNRs inside the silica shell are more randomly oriented. We further evaluated the CV (coefficient of variation) values to compare the variation of the major length of both nanoparticles (bare AuNRs and AuNRs@mSiO₂)

in detail. As shown in the inset of **Fig. 23**, the CV of AuNRs@mSiO₂ is higher than that of bare AuNRs, which means that statistically the variation of the major axis in AuNRs@mSiO₂ is higher. Therefore, we confirmed by electron microscopy techniques that AuNRs@mSiO₂ having a spherical silica shell were successfully synthesized and that the AuNR cores in the shell exhibited random 3D orientations, as depicted in **Fig. 22B**.

There is an important point that needs to be discussed in **Fig. 22 and 23**. In the gel matrix method, the AuNRs are embedded in an agarose gel matrix to obtain random 3D orientations at different focal planes, and a z-axis scanning is conducted to determine their positions and 3D orientations under an optical microscopy (**Fig. 24A**). In comparison, it should be noted that, with the spherical AuNRs@mSiO₂, we can produce random 3D orientations of AuNR cores in the shell at the same focal plane of the objective (**Fig. 24B**). Therefore, we expect that the AuNRs@mSiO₂ can be used for the direct and high-throughput detection of the 3D orientations of AuNR cores in the same focal plane of the objective within a single frame.

To demonstrate this, we studied the 3D orientations of single AuNR (10 × 30 nm) cores in the silica shell by a scattering-based DF microscope. In DF microscopy, the light scattered from the samples is collected only by an objective lens and is directed either to a spectrograph or to an EMCCD camera. To determine the 3D orientation of the single AuNR cores, we first employed the defocused DF orientation imaging technique based on an electron transition dipole approximation, considering the fact that the dipole radiation exhibits an angular anisotropy.¹² When a nanoprobe

is defocused from the focal plane, the scattering field distribution of the blurred image provides information about the emission dipole orientation of the nanoprobe.^{12, 23} The azimuthal angle (φ) and polar angle (θ) of AuNRs are defined in **Fig. 6B**. **Fig. 25A** shows a DF scattering image of single AuNRs@mSiO₂ on a glass slide at the focal plane, whereas **Fig. 25B** presents the scattering spectra of two AuNRs@mSiO₂ (AuNR1@mSiO₂ and AuNR2@mSiO₂) squared in **Fig. 25A** embedded in water. The longitudinal LSPR peak of the two AuNRs@mSiO₂ are observed at about 746 nm, which is consistent with the ensemble spectra in **Fig. S7**.

Anisotropic AuNRs that are much smaller than the wavelength of the incident light can be considered electric point dipoles.¹² According to the electrostatic approximation, the overall scattering electrical field from a AuNR can be quantified through linear superposition of three independent scattering electric fields related to three mutually orthogonal dipoles.¹² Therefore, the orientation of a single AuNR could be resolved by characterizing the scattering intensity distribution from each dipole. We then tried to obtain defocused images of two AuNRs@mSiO₂ (AuNR1@mSiO₂ and AuNR2@mSiO₂) to estimate their azimuthal and polar angles. The defocused scattering patterns of the single AuNRs@mSiO₂ highlighted by a square in **Fig. 25A** were obtained with an exposure time of 10 s due to their weak scattering intensity. As shown in **Fig. 25A**, the light scattered from a nanorod in the focal plane of the objective was focused into a solid bright spot, which gives little information about the 3D orientation of the AuNR emission dipole. However, when the AuNR was positioned at $\sim 1 \mu\text{m}$ away from the focal plane, the intensity distribution of the blurred image

provides information about the AuNR emission dipole orientation (**Fig. 25C**). The in-plane orientation angle φ can be readily extracted from the two-lobe scattering pattern exhibiting angular anisotropy. Meanwhile, the out-of-plane polar angle θ was estimated by using the program developed by Enderlein and Böhmer for simulating the characteristic intensity distribution from an emitter with three perpendicular emission dipoles of different emission strengths.^{31, 32} The orientation of AuNRs on a glass substrate can be estimated by referring to their corresponding field map. The best-fit simulated scattering pattern (**Fig. 25C**) was obtained by adjusting the parameters defining the orientation angles and the emission strength of three mutually orthogonal oscillation dipoles of the AuNRs. The polar and azimuthal angles of AuNR1@mSiO₂ were estimated to be 69° and 136°, respectively, by comparing the measured scattering pattern with the best-fit simulated scattering pattern obtained from the simulation program (**Fig. 25C,D**).^{12, 20} In addition, the polar and azimuthal angles of AuNR2@mSiO₂ were estimated to be 80° and 160°, respectively (**Fig. 25C,D**). Therefore, by using defocused imaging, we could characterize the 3D orientations of single AuNRs (10 × 30 nm) coated with mesoporous silica shell with high throughput within a single frame at the same focal plane of the objective, which is challenging for single AuNRs embedded in a gel matrix.

Besides the defocused orientation imaging investigation, we conducted a rotational study to confirm the polarization dependency of the two AuNRs@mSiO₂ in **Fig. 25A** under DF microscopy. More specifically, we performed polarization-sensitive DF scattering imaging of the AuNRs@mSiO₂ by linearly polarizing the 760

nm wavelength light and rotating the polarizer by 10° per step from 0° to 360° . As seen in **Fig. S8**, the scattering intensity for the two AuNRs@mSiO₂ periodically changed as a function of the polarization angle and fitted well with the function of $\sin^2(\varphi)$. The DF scattering intensities were strongly affected by the 3D orientation of the AuNR cores in silica shell at the LSPR wavelength of 760 nm. We observed that the modulation depth for the intensity curve of AuNR1@mSiO₂ more tilted from the glass surface was smaller than that of AuNR2@mSiO₂. Moreover, the phase difference of $\sim 25^\circ$ between the two AuNRs@mSiO₂ supports their different in-plane orientations inside the silica shell, which is consistent with the defocused orientation imaging result depicted in **Fig. 25C, D**.

To clearly demonstrate the advantage of using AuNRs@mSiO₂ over the conventional gel matrix method, we further performed a DF imaging of tilted AuNRs with an average size of 25×73 nm embedded in a 2% agarose gel matrix. We obtained the DF images of AuNRs by scanning in the z-direction with a vertical step size of 40 nm. **Fig. S9A** shows the consecutive DIC images of the AuNRs with random 3D orientations in the gel matrix, obtained at different focal planes. It is clearly observed in **Fig. S9A** that the four AuNRs have different focal planes in the matrix. **Fig. S9B** shows defocused DF images of the AuNRs, and their random 3D orientations can be directly visualized in their characteristic doughnut-shaped defocused patterns. Therefore, the current gel matrix method requires a vertical scan to observe the random 3D orientations of the AuNRs and to investigate their orientation-dependent optical properties. In contrast, it should be noted that the spherical AuNRs@mSiO₂ enable us

to achieve the high-throughput determination of 3D spatial orientations of the AuNR cores in the silica shell at the same focal plane of the objective without LSPR coupling among nanoparticles (**Fig. 25**).

Last, we demonstrate another advantage of using spherical AuNRs@mSiO₂ in defocused DF orientation imaging and studies at the single-particle level. Currently, the 2D in-plane orientation of AuNRs can be conveniently changed with high accuracy by rotating a rotational stage. However, the precise control of the out-of-plane orientations (or tilting angles) of AuNRs in the z-direction remains a grand challenge. In this study, we aimed to overcome this challenge by taking advantage of the spherical shape of the AuNRs@mSiO₂. The idea was to roll a spherical AuNR@mSiO₂ by applying an external force, which was validated by performing a proof-of-concept experiment. More specifically, we flowed a solution through a syringe pump as an external force to move and roll the spherical AuNRs@mSiO₂ in a glass flow cell (**Fig. 26A**). We recorded movies at a temporal resolution of 100 ms (10 fps), which show the rolling and movement of the AuNRs@mSiO₂ on a microfluidic channel under a fluidic condition **Fig. S10A**. **Fig. S10A** shows 60 consecutive DF images of three AuNRs@mSiO₂s selected from recorded movie. **Fig. S10A**, the two AuNRs@mSiO₂ circled with blue in **Fig. S10B** started to move forward in the same direction when flowing the solution at an optimized flow rate of 0.5 $\mu\text{L}/\text{min}$. It is worth noting that the AuNR@mSiO₂ indicated by the yellow circle in **Fig. S10B** does not move together with the other two AuNRs@mSiO₂s, which clearly supports the theory that the movement of the two nanoparticles shown in **Fig. S10** is not caused by a sample

drifting but by the external fluidic force. However, we also noticed that some AuNRs@mSiO₂s were detached from the glass surface at the same fluidic condition (**Fig. S11**), which is clearly different from the rolling (or moving) of AuNRs@mSiO₂s on the surface shown in **Fig. S11**. This could be ascribed to the heterogeneity in size of the AuNRs@mSiO₂, which is supported by the TEM images in **Fig. 22D**. Therefore, we accomplished the in-situ movement and position change of spherical AuNRs@mSiO₂ by applying an external fluidic force, which cannot be achieved for uncoated AuNRs fixed on a glass slide or embedded in a gel matrix under the same condition.

Then to gain a deeper understanding on the movements of the AuNR cores inside the silica shell shown in **Fig. S11**, we tried to track the real-time 3D rotational motions of the AuNR cores under the defocused orientation imaging method. **Fig. S12** show a single AuNR3@mSiO₂ moving forward, measured under defocused DF microscopy. As clearly shown in **Fig. S12**, which present an enlarged AuNR3, the defocused scattering patterns changed as a function of the frames, which indicates that the 3D orientations of the AuNR cores in the shell varied with the forward movement. To clearly demonstrate this, six frames showing clear transitions between up and down in the opening direction on the patterns were selected from **Fig. S12**, as indicated by a white-dotted line in **Fig. 26B**. **Fig. 26C** shows the trajectory of tracking of the center of AuNR3@mSiO₂ as a function of frames when moving forward. To further understand the transitions among the characteristic defocused scattering patterns over time in **Fig. S12**, we determined the azimuthal and polar angles of AuNR3@mSiO₂

using defocused image patterns at each frame and tracked its orientation angles as a function of frames (**Fig. 26D**). The azimuthal angle φ changed mainly between 90° and 270° as a function of frames when moving forward as presented in **Fig. 26C**. The transitions in the azimuthal and polar angles over time suggest that AuNR3@mSiO₂ underwent both rolling and twisting motions, although not continuously, along the flow direction over time under fluidic condition (**Fig. 26D**). Therefore, we successfully changed the in-situ x-y positions and 3D orientation angles of single AuNR cores (10×30 nm) inside the silica shell by applying an external fluidic force and tracked their real-time 3D orientations and characteristic detailed motions as a function of time. In addition, we demonstrated that spherical AuNRs@mSiO₂ can be used as reference nanoparticles for systematic fundamental studies toward the development of new far-field optical imaging techniques for the determination of the full 3D orientations of single AuNRs with higher accuracy.

3.2.5 Conclusion

In summary, single AuNRs@mSiO₂ consisting of an AuNR core (10×30 nm) and a spherical-shaped outer mesoporous silica shell were synthesized. This morphology proved to be advantageous for obtaining random 3D orientations of the AuNR core inside the silica shell in the same focal plane of the objective when depositing the nanorods on a glass slide, which cannot be achieved with the conventional gel matrix method. We resolved the 3D orientations of AuNRs@mSiO₂ by defocused DF imaging within a single frame at the same focal plane of the objective

with high throughput, while avoiding the LSPR coupling that can result in a spectral shift in single-particle characterization. Furthermore, we changed the in-situ positions and 3D orientation angles of single AuNR cores inside the silica shell by applying an external force and tracked their real-time 3D orientations and characteristic motions over time. Therefore, through use of AuNRs@mSiO₂, the present method overcomes the conventional gel matrix method commonly used in single particle rotational tracking studies. Furthermore, AuNRs@mSiO₂ can be used as reference nanoparticles for systematic and fundamental studies aiming to develop more sensitive and accurate optical imaging methods for determining the full 3D orientations of AuNRs. However, AuNRs@mSiO₂ cannot be a local orientation probe because of the silica shell that can block the interaction of AuNRs with the medium. Further studies are currently underway to control the 3D orientation angles of AuNRs@mSiO₂ more accurately.

3.2.6 References

1. van der Zande, B. M. I.; Böhmer, M. R.; Fokkink, L. G. J.; Schönenberger, C., Aqueous Gold Sols of Rod-Shaped Particles. *J. Phys. Chem. B* **1997**, *101* (6), 852.
2. Link, S.; El-Sayed, M. A., Spectral Properties and Relaxation Dynamics of Surface Plasmon Electronic Oscillations in Gold and Silver Nanodots and Nanorods. *J. Phys. Chem. B* **1999**, *103* (40), 8410.
3. Jana, N. R.; Gearheart, L.; Murphy, C. J., Wet Chemical Synthesis of High Aspect Ratio Cylindrical Gold Nanorods. *J. Phys. Chem. B* **2001**, *105* (19), 4065.
4. Mahmoud, M. A., Controlling the orientations of gold nanorods inside highly packed 2D arrays. *Phys. Chem. Chem. Phys.* **2014**, *16* (47), 26153.
5. Mock, J. J.; Hill, R. T.; Degiron, A.; Zauscher, S.; Chilkoti, A.; Smith, D. R., Distance-Dependent Plasmon Resonant Coupling between a Gold Nanoparticle and Gold Film. *Nano Lett.* **2008**, *8* (8), 2245.
6. Funston, A. M.; Novo, C.; Davis, T. J.; Mulvaney, P., Plasmon Coupling of Gold Nanorods at Short Distances and in Different Geometries. *Nano Lett.* **2009**, *9* (4), 1651.
7. Huang, J.; Kim, F.; Tao, A. R.; Connor, S.; Yang, P., Spontaneous formation of nanoparticle stripe patterns through dewetting. *Nat. Mater.* **2005**, *4* (12), 896.
8. Nikoobakht, B.; Wang, Z. L.; El-Sayed, M. A., Self-Assembly of Gold Nanorods. *J. Phys. Chem. B* **2000**, *104* (36), 8635.
9. Hsieh, S.; Meltzer, S.; Wang, C. R. C.; Requicha, A. A. G.; Thompson,

M. E.; Koel, B. E., Imaging and Manipulation of Gold Nanorods with an Atomic Force Microscope. *J. Phys. Chem. B* **2002**, *106* (2), 231.

10. Darwich, S.; Mougin, K.; Rao, A.; Gnecco, E.; Jayaraman, S.; Haidara, H., Manipulation of gold colloidal nanoparticles with atomic force microscopy in dynamic mode: influence of particle-substrate chemistry and morphology, and of operating conditions. *Beilstein J. Nanotechnol.* **2011**, *2*, 85.

11. Cha, S. H.; Kang, S. H.; Lee, Y. J.; Kim, J. H.; Ahn, E. Y.; Park, Y.; Cho, S., Fabrication of nanoribbons by dielectrophoresis assisted cold welding of gold nanoparticles on mica substrate. *Sci. Rep.* **2019**, *9* (1), 3629.

12. Xiao, L.; Qiao, Y.; He, Y.; Yeung, E. S., Three Dimensional Orientational Imaging of Nanoparticles with Darkfield Microscopy. *Anal. Chem.* **2010**, *82* (12), 5268.

13. Sönnichsen, C.; Alivisatos, A. P., Gold Nanorods as Novel Nonbleaching Plasmon-Based Orientation Sensors for Polarized Single-Particle Microscopy. *Nano Lett.* **2005**, *5* (2), 301.

14. Lee, S. Y.; Tsalu, P. V.; Kim, G. W.; Seo, M. J.; Hong, J. W.; Ha, J. W., Tuning Chemical Interface Damping: Interfacial Electronic Effects of Adsorbate Molecules and Sharp Tips of Single Gold Bipyramids. *Nano Lett.* **2019**, *19* (4), 2568.

15. Berciaud, S.; Cognet, L.; Blab, G. A.; Lounis, B., Photothermal Heterodyne Imaging of Individual Nonfluorescent Nanoclusters and Nanocrystals. *Phys. Rev. Lett.* **2004**, *93* (25), 257402.

16. Chang, W. S.; Ha, J. W.; Slaughter, L. S.; Link, S., Plasmonic nanorod absorbers as orientation sensors. *Proc. Natl. Acad. Sci. U. S. A.* **2010**, *107* (7), 2781.

17. Ha, J. W.; Sun, W.; Stender, A. S.; Fang, N., Dual-Wavelength Detection of Rotational Diffusion of Single Anisotropic Nanocarriers on Live Cell Membranes. *J. Phys. Chem. C* **2012**, *116* (4), 2766.
18. Won Ha, J.; Sun, W.; Wang, G.; Fang, N., Differential interference contrast polarization anisotropy for tracking rotational dynamics of gold nanorods. *Chemical Communications* **2011**, *47* (27), 7743-7745.
19. Lee, S. Y.; Han, Y.; Hong, J. W.; Ha, J. W., Single gold bipyramids with sharp tips as sensitive single particle orientation sensors in biological studies. *Nanoscale* **2017**, *9* (33), 12060.
20. Ha, J. W.; Marchuk, K.; Fang, N., Focused Orientation and Position Imaging (FOPI) of Single Anisotropic Plasmonic Nanoparticles by Total Internal Reflection Scattering Microscopy. *Nano Lett.* **2012**, *12* (8), 4282.
21. Marchuk, K.; Fang, N., Three-Dimensional Orientation Determination of Stationary Anisotropic Nanoparticles with Sub-Degree Precision under Total Internal Reflection Scattering Microscopy. *Nano Lett.* **2013**, *13* (11), 5414.
22. Toprak, E.; Enderlein, J.; Syed, S.; McKinney, S. A.; Petschek, R. G.; Ha, T.; Goldman, Y. E.; Selvin, P. R., Defocused orientation and position imaging (DOPI) of myosin V. *Proc. Natl. Acad. Sci. U. S. A.* **2006**, *103* (17), 6495.
23. Li, T.; Li, Q.; Xu, Y.; Chen, X. J.; Dai, Q. F.; Liu, H.; Lan, S.; Tie, S.; Wu, L. J., Three-Dimensional Orientation Sensors by Defocused Imaging of Gold Nanorods through an Ordinary Wide-Field Microscope. *ACS Nano* **2012**, *6* (2), 1268.
24. Kim, G. W.; Lee, S. Y.; Ha, J. W., Three-dimensional defocused orientation

sensing of single bimetallic core–shell gold nanorods as multifunctional optical probes. *Analyst* **2017**, *142* (6), 899.

25. Ha, J. W., Characteristic image patterns of single anisotropic plasmonic nanoparticles embedded in a gel matrix. *Nanoscale* **2015**, *7* (31), 13159.

26. Xiao, L.; Ha, J. W.; Wei, L.; Wang, G.; Fang, N., Determining the Full Three-Dimensional Orientation of Single Anisotropic Nanoparticles by Differential Interference Contrast Microscopy. *Angew. Chem., Int. Ed.* **2012**, *51* (31), 7734.

27. Yoon, S.; Lee, B.; Yun, J.; Han, J. G.; Lee, J. S.; Lee, J. H., Systematic study of interdependent relationship on gold nanorod synthesis assisted by electron microscopy image analysis. *Nanoscale* **2017**, *9* (21), 7114.

28. Yoon, S.; Lee, B.; Kim, C.; Lee, J. H., Controlled Heterogeneous Nucleation for Synthesis of Uniform Mesoporous Silica-Coated Gold Nanorods with Tailorable Rotational Diffusion and 1 nm-Scale Size Tunability. *Cryst. Growth Des.* **2018**, *18* (8), 4731.

29. Gorelikov, I.; Matsuura, N., Single-Step Coating of Mesoporous Silica on Cetyltrimethyl Ammonium Bromide-Capped Nanoparticles. *Nano Lett.* **2008**, *8* (1), 369.

30. Orendorff, C. J.; Murphy, C. J., Quantitation of Metal Content in the Silver-Assisted Growth of Gold Nanorods. *J. Phys. Chem. B* **2006**, *110* (9), 3990.

31. Böhmer, M.; Enderlein, J., Orientation imaging of single molecules by wide-field epifluorescence microscopy. *J. Opt. Soc. Am. B* **2003**, *20* (3), 554.

32. Lee, J.; Ha, J. W., Defocused dark-field orientation imaging of single gold

microrods on synthetic membranes. *Phys. Chem. Chem. Phys.* **2017**, *19* (36), 24453.

3.2.7 Figures and Captions

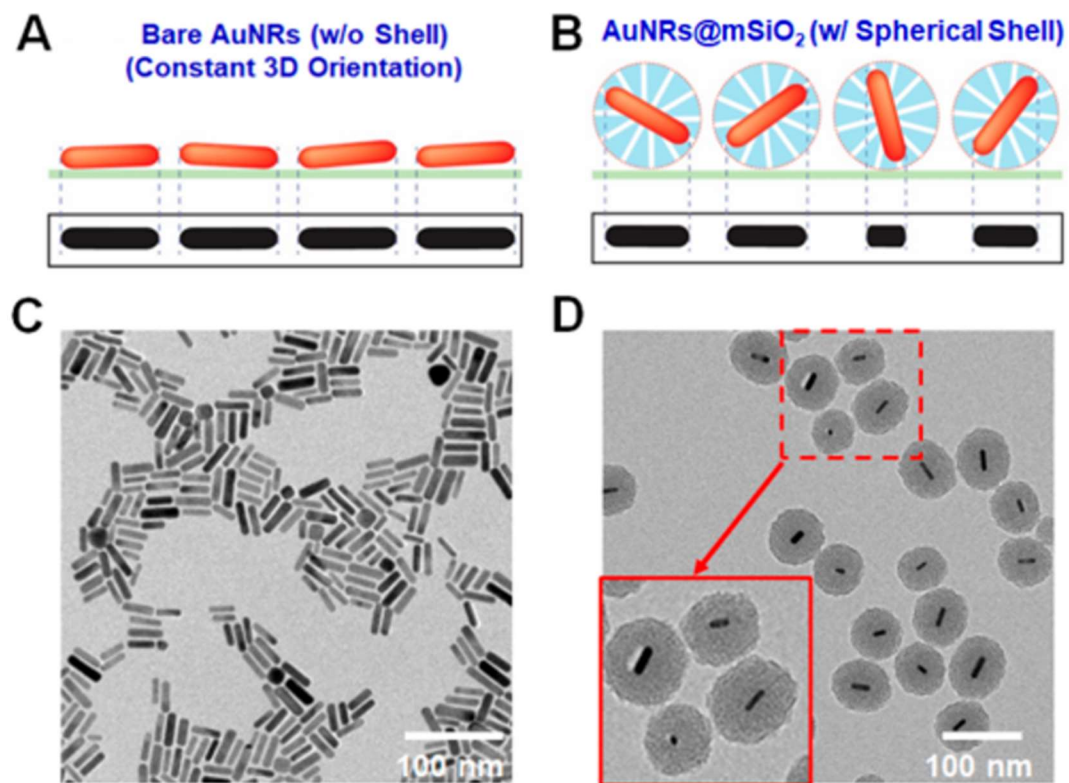


Figure 22. (A) Schematic showing bare AuNRs deposited on a glass slide, yielding projections having almost the same length. (B) Schematic depicting AuNRs@mSiO₂ with the AuNR cores exhibiting random 3D orientations in the shell. The projected length varies depending on their 3D spatial orientations in the spherical shell. (C, D) TEM images of bare AuNRs (C) and AuNRs@mSiO₂ (D), respectively.

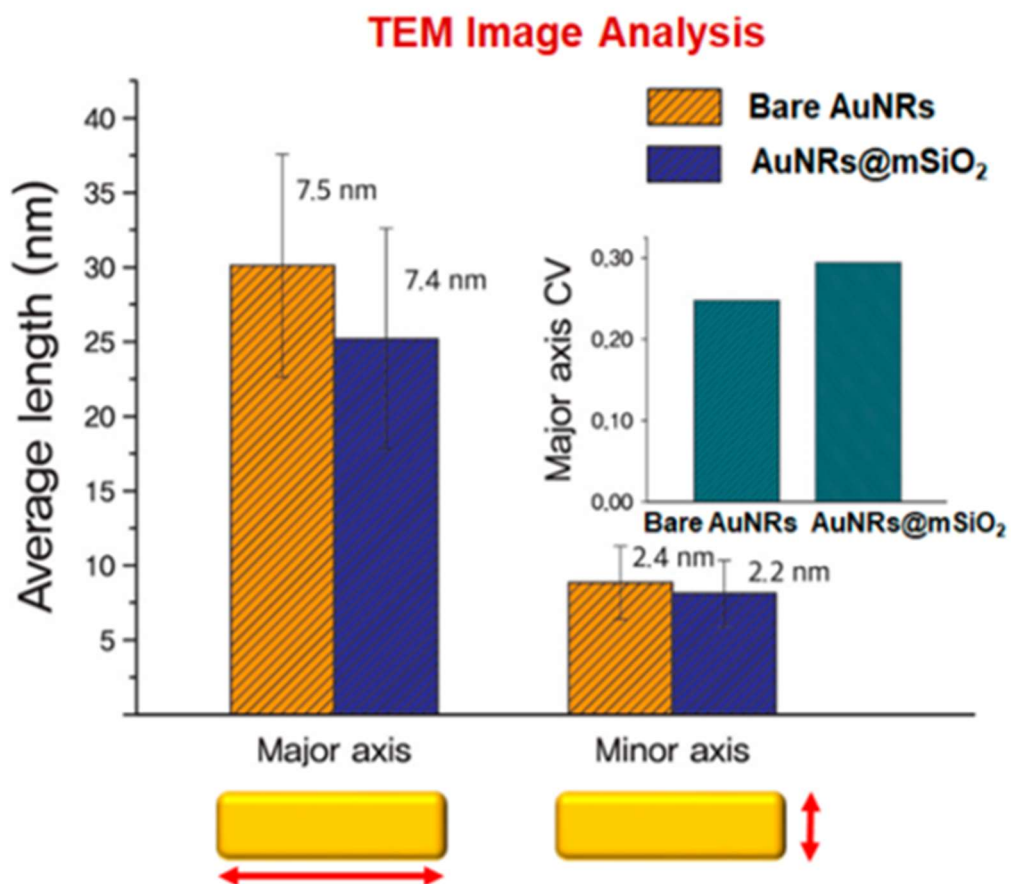


Figure 23. TEM image analysis based on a custom MATLAB script of the sizes (length and diameter) of bare AuNRs without the silica shell and AuNRs with the spherical mesoporous silica shell.

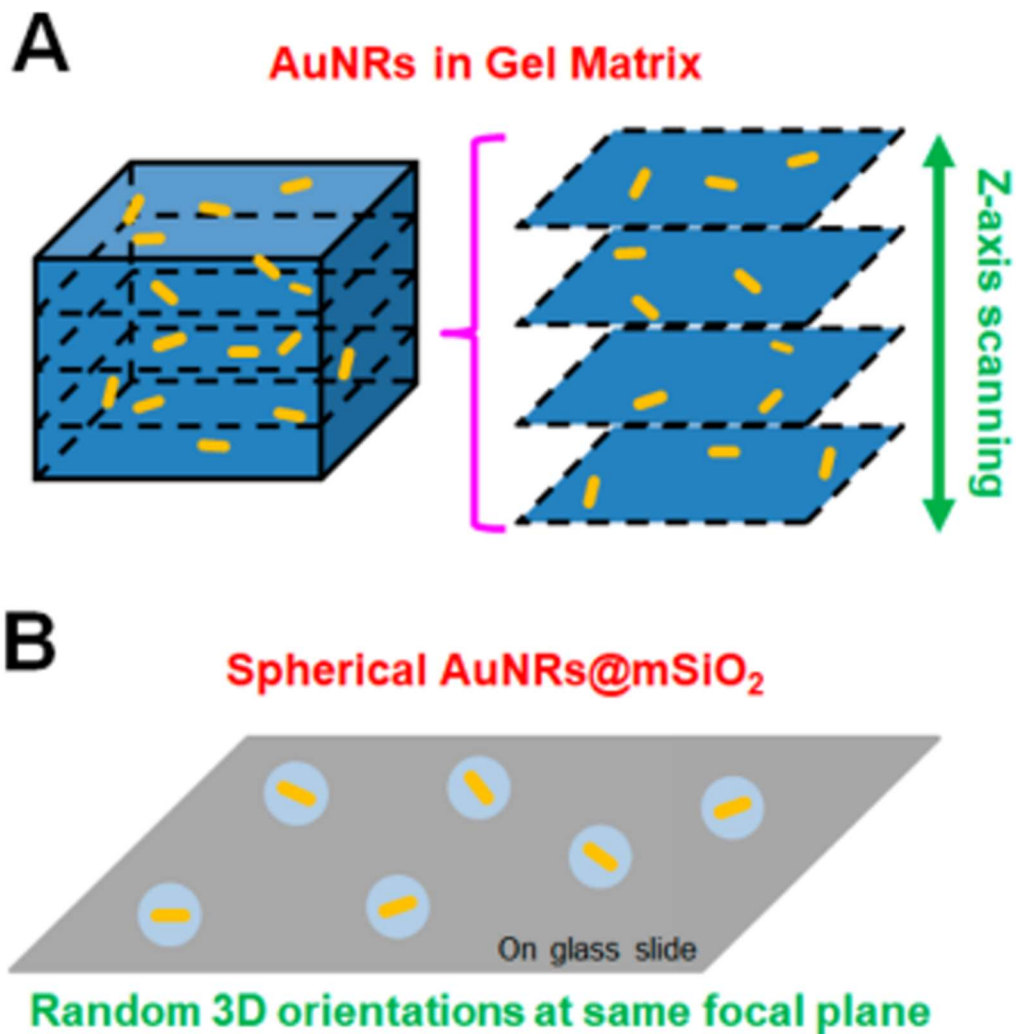


Figure 24 (A) Schematic showing AuNRs embedded in a gel matrix at different focal planes. The embedded AuNRs need to be measured by vertical scanning in the z-axis. (B) Schematic showing spherical AuNRs@mSiO₂ deposited on a glass slide at the same focal plane of the objective lens. The AuNR cores are positioned with random 3D orientations inside the silica shell.

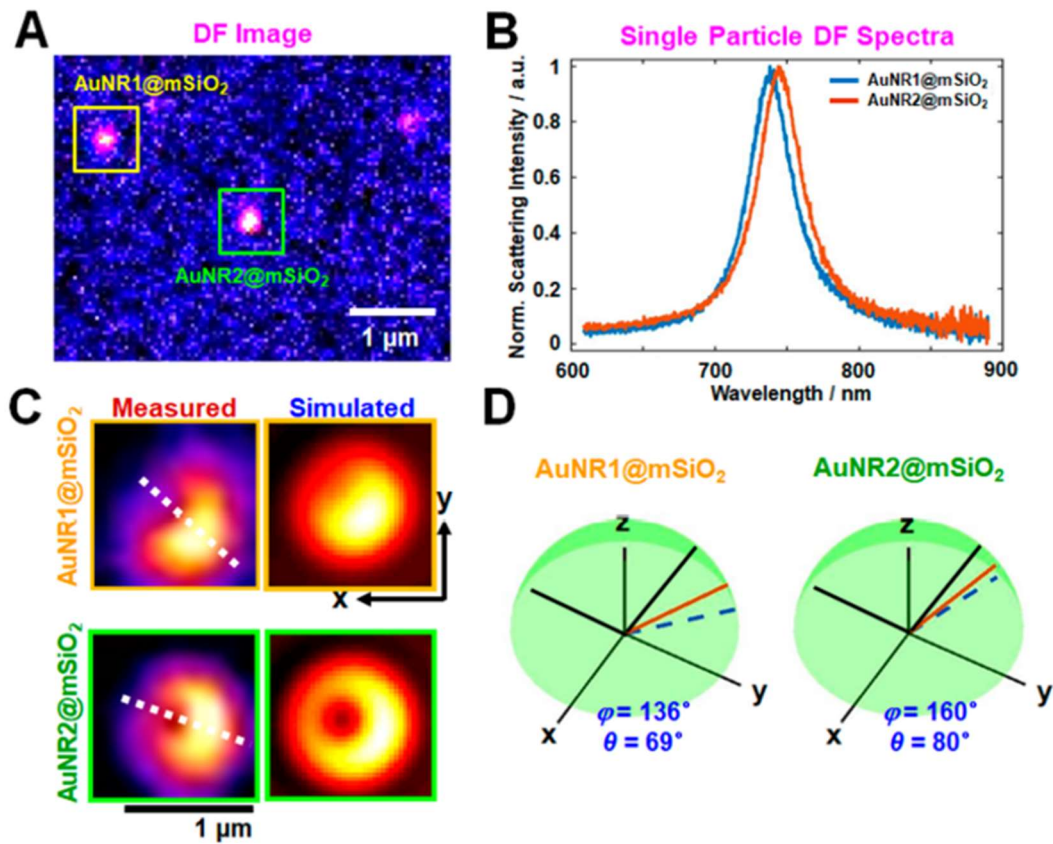


Figure 25. Defocused orientation imaging of spherical AuNRs@mSiO₂. **(A)** A DF scattering image of single AuNRs@mSiO₂ in the focal plane. **(B)** Single particle scattering spectra of two AuNRs@mSiO₂ indicated by a square in **(A)**. **(C)** Measured defocused image patterns of the two AuNRs@mSiO₂ (left). The white dashed line indicates the single dipole orientation. The scale bar represents 1 μm. The corresponding best-fit simulated scattering patterns for the two AuNRs@mSiO₂ are also presented (right). **(D)** The 3D spatial orientations of two AuNRs@mSiO₂ determined through the pattern match analysis are illustrated. The red line shows the determined 3D orientation, and the blue-dotted line is the corresponding in-plane projection.

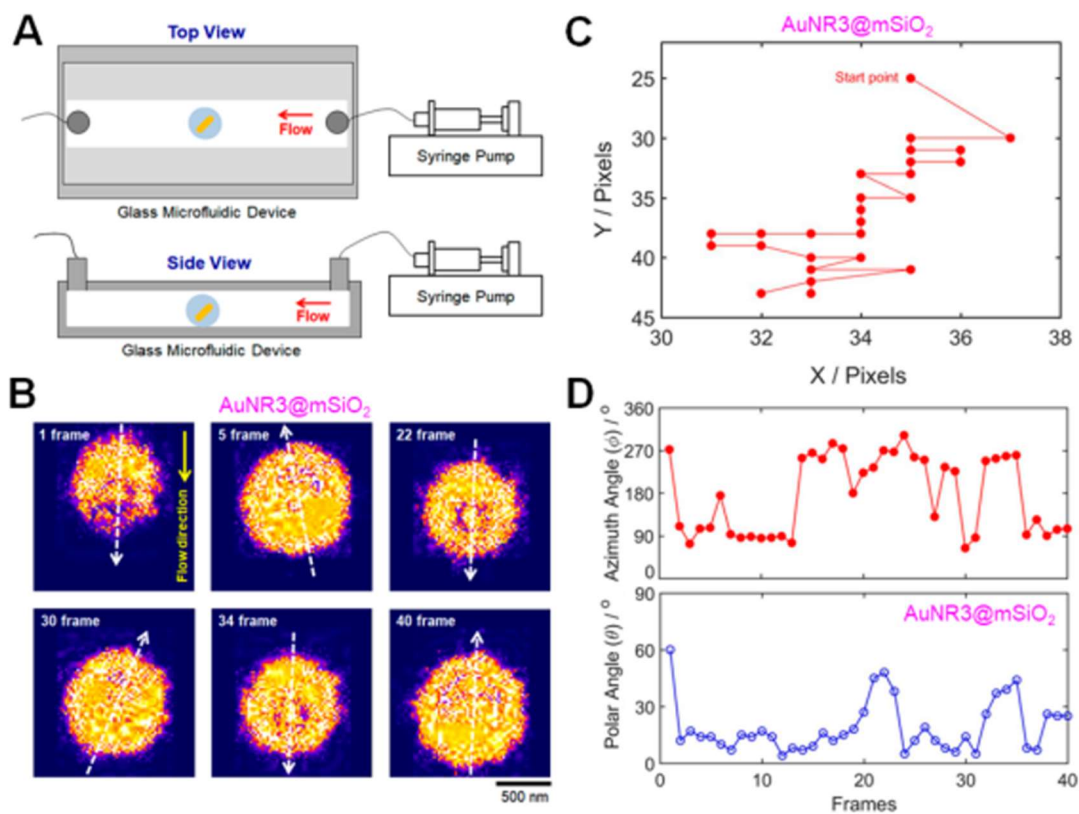


Figure 26. In situ control and tracking of positions and 3D orientations of single AuNRs@mSiO₂. **(A)** Schematic showing the concept of controlling the positions and spatial orientations of a single AuNR@mSiO₂ by applying an external fluidic force. **(B)** Doughnut-shaped defocused scattering images of AuNR3@mSiO₂ to show clear transitions between up and down in the opening direction on the patterns indicated by a white-dotted arrow. **(C)** Trajectory of the center position of AuNR3@mSiO₂ when moving forward by the external flow. **(D)** Real-time tracking of azimuthal (top) and polar (bottom) angles of AuNR3@mSiO₂ for 40 consecutive frames. The temporal resolution was 100 ms.

3.2.8 Supplementary Materials

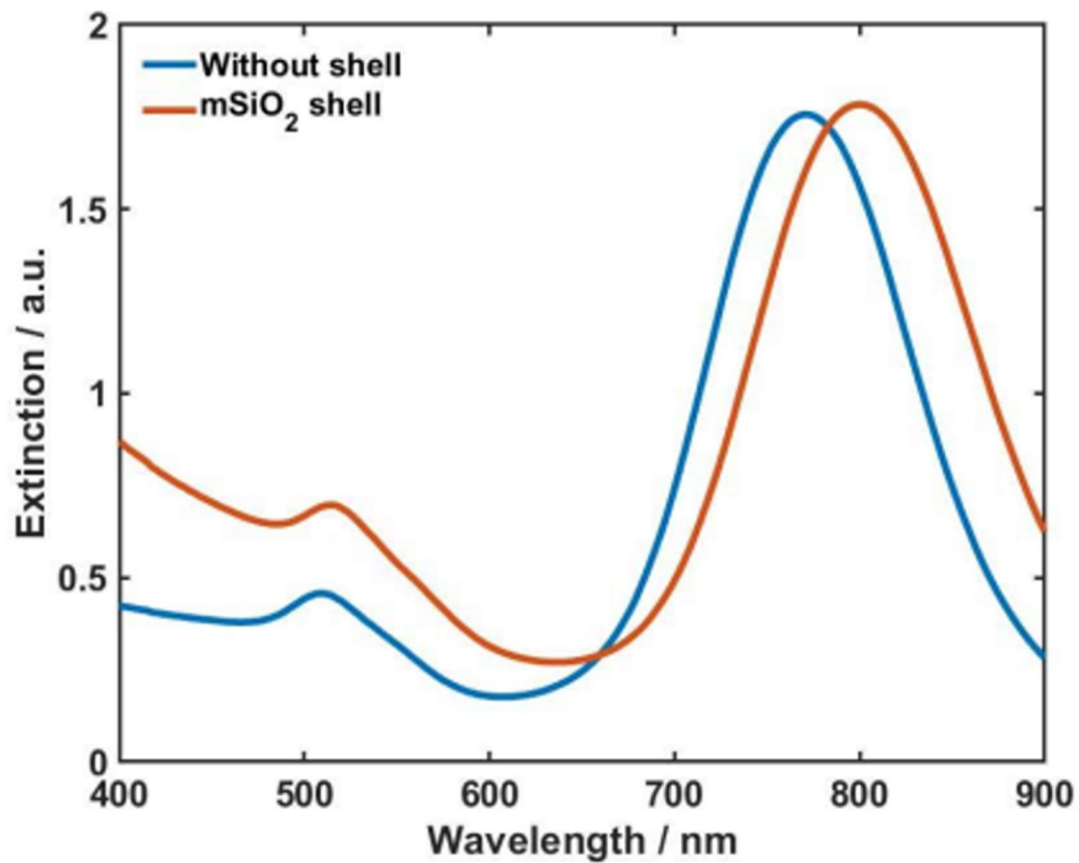


Figure S7. UV-Vis extinction overlaid spectra of AuNRs without shell (blue curve) and AuNRs@mSiO₂ (red curve). Two distinct LSPR peaks are observed for the anisotropic AuNRs.

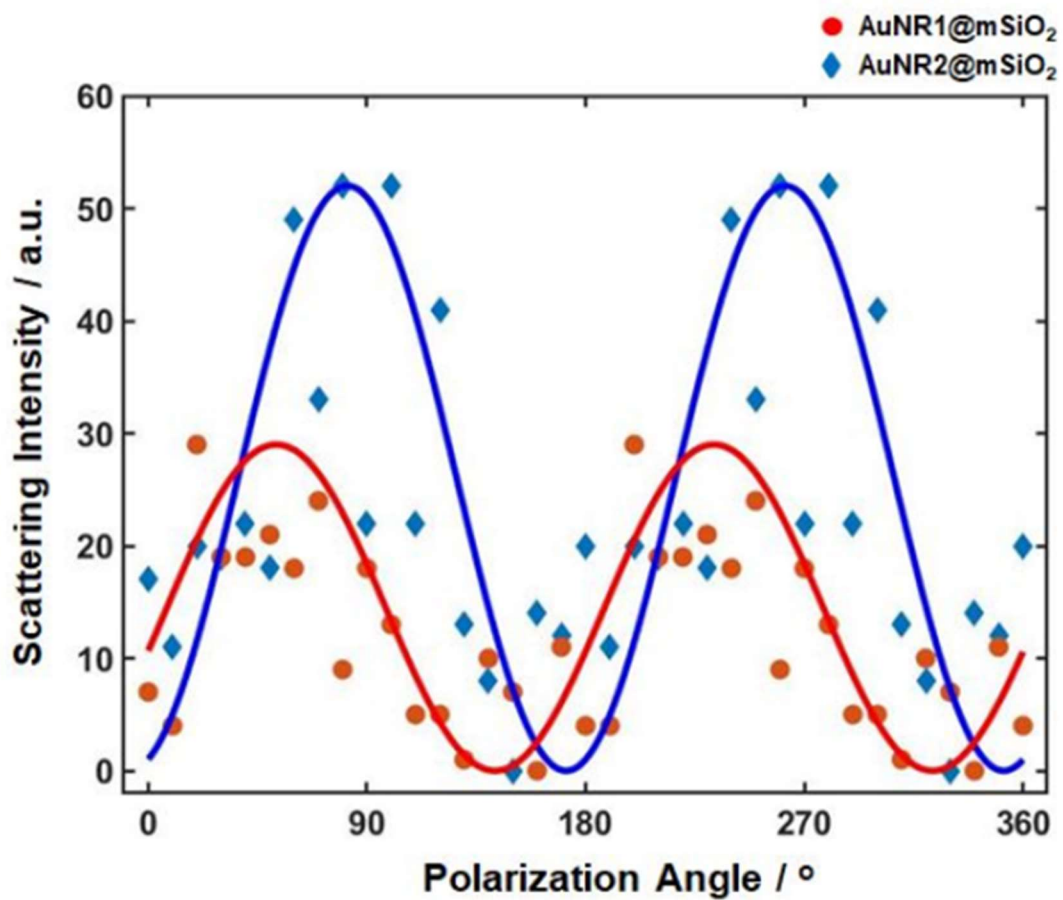


Figure S8. Changes in the DF scattering intensities of two in-focus AuNRs@mSiO₂ (AuNR1@mSiO₂ and AuNR2@mSiO₂) in Fig. 25 as a function of polarization angle with 10° increment.

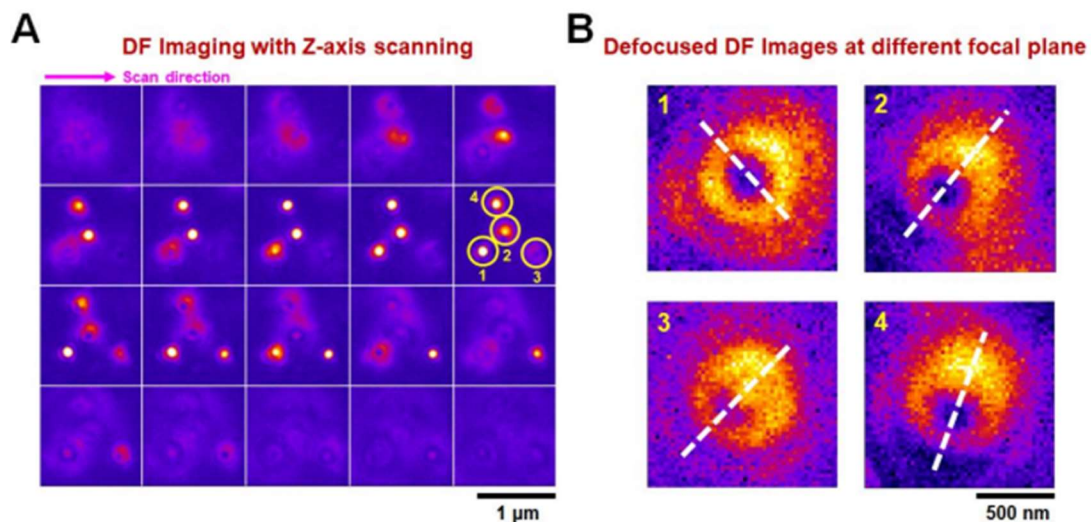


Figure S9. (A) Consecutive DF images of the embedded AuNRs ($25 \text{ nm} \times 73 \text{ nm}$) measured by z-axis scanning with a vertical step size of 40 nm. The AuNRs in gel matrix have random 3D orientations at the different focal planes. (B) Defocused scattering patterns of the four AuNRs circled in (A) obtained at the different focal planes. The white-dotted line shows an in-plane orientations of the AuNRs.

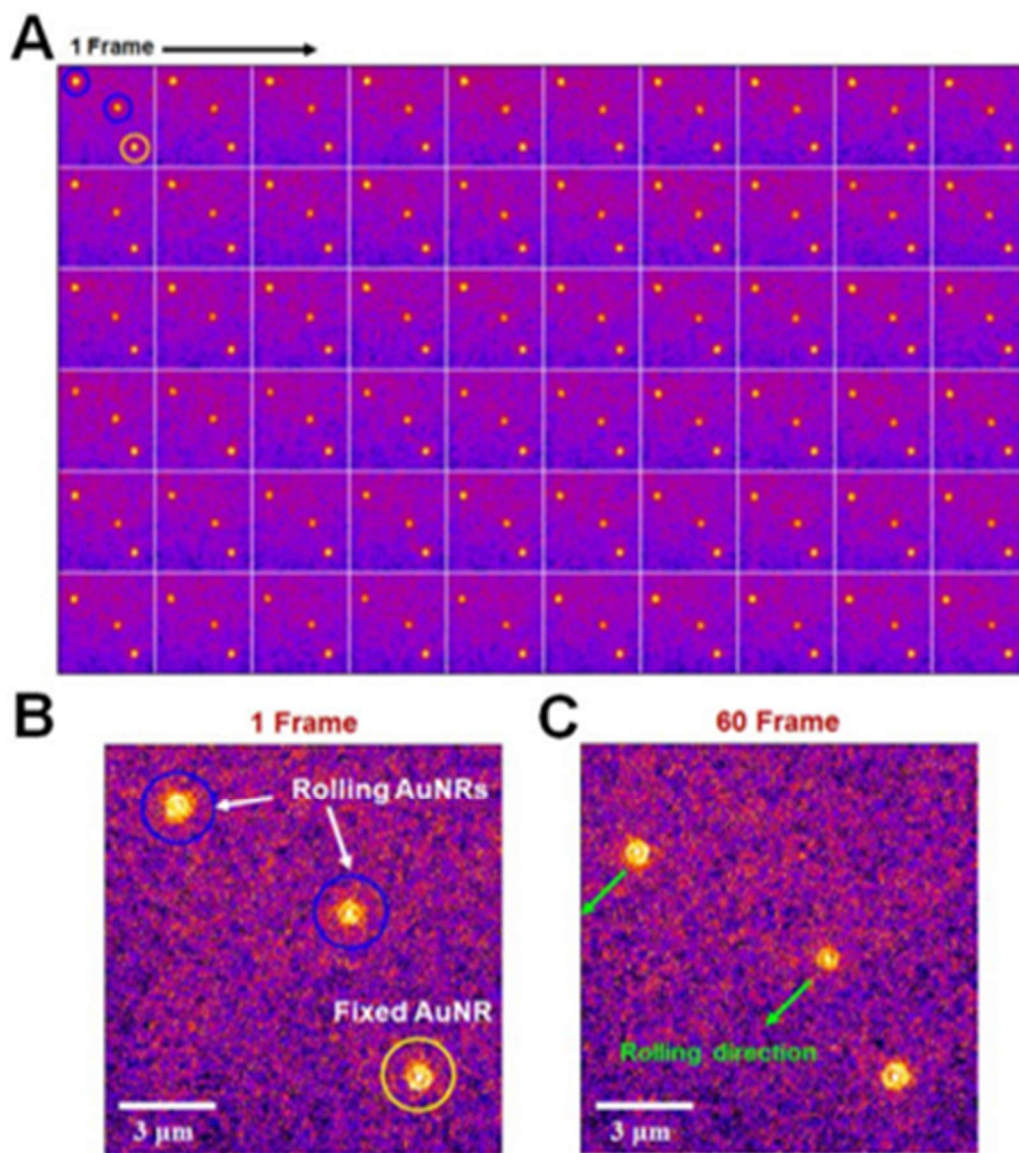


Figure S10 (A) Consecutive DF scattering images of AuNRs@mSiO₂ chosen from movie recorded at a temporal resolution of 100 ms. (B, C) Enlarged DF scattering images of AuNRs@mSiO₂ recorded at 1 Frame (B) and 60 Frame (C), respectively.

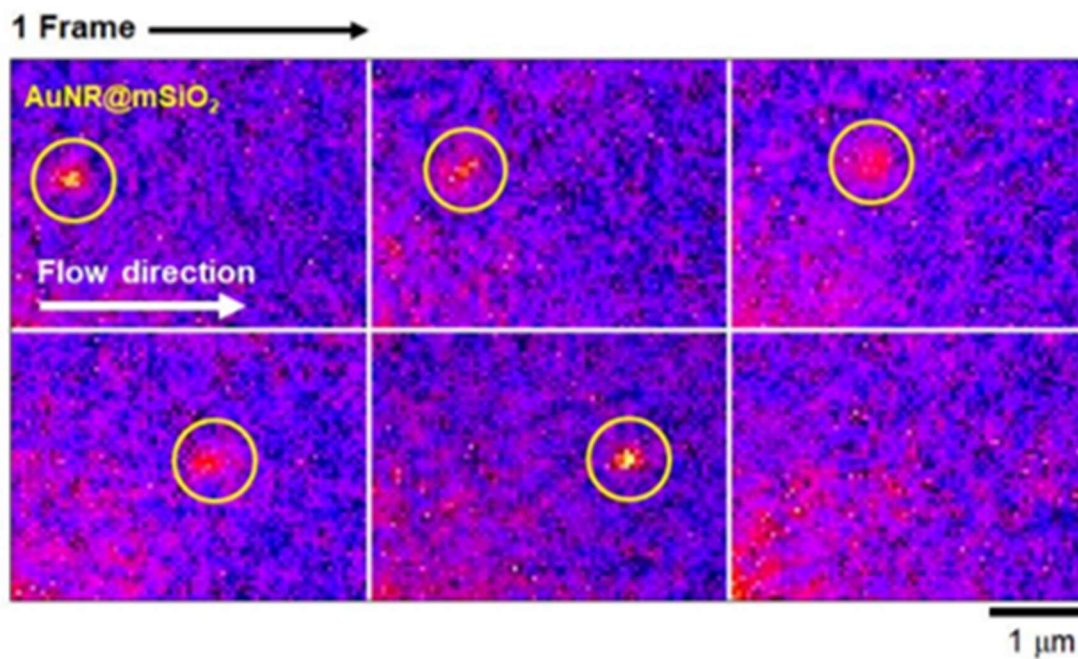


Figure S11. Consecutive DF images of a AuNR@mSiO₂ chosen from recorded movie. This movie was recorded at the frame rate of 10 fps. The AuNR@mSiO₂ is detached from a glass slide over time under the same external fluidic condition (a flow rate of 0.5 μL/min in a flow cell).

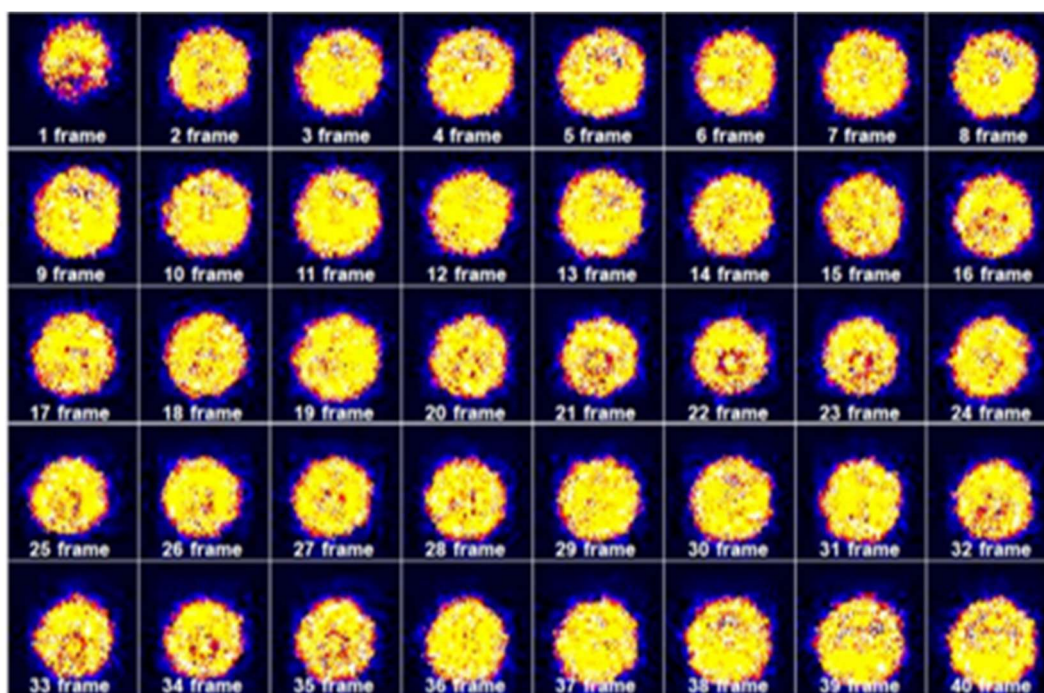


Figure S12. Consecutive DF scattering images of AuNR3@mSiO₂ as a function of frames obtained from recorded movie.

3.3 Mesoporous Silica Shell-Coated Single Gold Nanorods as Multifunctional Orientation Probes in Dynamic Biological Environments

Geun Wan Kim In-Seob Han,* and Ji Won Ha*

A paper published in RSC Advances, **2021**, 11, 38632-38637.

Reproduced by permission of the Royal Society of Chemistry

*Corresponding author

3.3.1 Abstract

Mesoporous silica shell-coated gold nanorods (AuNRs@mSiO₂) can be employed as promising multifunctional orientation probes in biological studies owing to their anisotropic optical properties, enhanced stability, excellent biocompatibility, etc. In this study, the optical properties of single AuNRs@mSiO₂ are characterized under dark-field and differential interference contrast (DIC) microscopy. Furthermore, we presented polarization-dependent, periodic DIC images and intensities of single AuNRs@mSiO₂ at their localized surface plasmon resonance wavelength and investigated their use as multifunctional orientation probes in dynamic biological environments. Moreover, the real-time rotational motions of the AuNRs@mSiO₂ on the HeLa cell membranes were tracked with millisecond temporal resolution. Overall, AuNRs@mSiO₂ demonstrated their capacity to act as multifunctional optical probes owing to the combined effect of the Au core, which can serve as an orientation probe and a local heat generator for phototherapy, and the mesoporous silica shell, which can be used as a reservoir of chemotherapeutics owing to its excellent loading capacity.

3.3.1 Introduction

Plasmonic gold nanorods (AuNRs) have numerous biomedical applications because of their unique shape-induced optical properties which can be attributed to the localized surface plasmon resonance (LSPR) effect, facile surface modification, etc.¹⁻³ For example, AuNRs have been used in phototherapy⁴ owing to their high efficiency in photothermal conversion and as local heat generators in chemotherapy treatments to activate and enhance photothermally induced drug release.^{5,6}

Despite their merits for biomedical applications, the presence of highly toxic cetyltrimethylammonium bromide (CTAB) bilayers used in the seed-mediated growth strategy limits the direct use of AuNRs.⁷ Thus, the surface functionalization of AuNRs is mandatory to improve their biocompatibility. Recently, mesoporous silica shell-coated AuNRs (AuNRs@mSiO₂, core@shell) have exhibited excellent biocompatibility.⁸ Furthermore, they can be used for synergistic phototherapy and chemotherapy combination using the mesoporous silica pores as reservoirs for chemotherapeutics owing to their high loading capacity, while the AuNRs serve as a local heat generator to induce phototherapy and trigger drug release.⁸⁻¹²

AuNRs have also been effectively used as orientation probes with a few polarization-based optical techniques, including dark-field (DF) polarization microscopy,¹³ photothermal heterodyne imaging (PHI),¹⁴ differential interference contrast (DIC) polarization anisotropy,^{1,15} and total internal reflection (TIR) scattering microscopy.¹⁶⁻¹⁸ Therefore, AuNRs@mSiO₂ can be used as multifunctional optical probes in biological studies. For example, the AuNR core can serve as an orientation

probe and a heat generator in phototherapy, whereas the mesoporous silica shell can be used as a chemotherapeutics reservoir.^{8, 10, 12} However, our understanding of their use as multifunctional orientation probes is still limited in dynamic biological environments.

The scattering-based methods, such as DF microscopy, are challenging for identifying AuNRs from cellular components and other debris that scatter light. In this regard, interference-based DIC microscopy is more suitable for investigating rotational motions of AuNRs in biological environments.

In the present study, we aim to investigate the optical properties of single AuNRs@mSiO₂ in DF and DIC microscopy. The effect of light polarization on the DIC image patterns and intensities of single AuNRs@mSiO₂ at their LSPR wavelengths is observed, and their use as multifunctional orientation probes in dynamic biological environments is examined under a DIC microscope.

3.3.3 Experimental Section

Materials and Chemicals

AuNRs@mSiO₂ were purchased from Nanopartz (Loveland, CO, USA). The cervical carcinoma cell line, HeLa-WT, was obtained from the Korean Cell Line Bank (Seoul, South Korea). Fetal bovine serum (FBS) was purchased from Sigma-Aldrich (St. Louis, MO, USA). Deionized water (18.2 MΩ cm) was prepared using a Sartorius Arium®Pro Ultrapure water system.

Sample Preparation and Characterization

The AuNRs@mSiO₂ solution was diluted with 18.2-M Ω pure water to the proper concentration and then sonicated for 15 min at room temperature. The samples were prepared by spin-casting the solution on the precleaned glass slide and covered with a 22 mm \times 22 mm No. 1.5 coverslip. The concentration of AuNRs@mSiO₂ on the glass surface was controlled to be $\sim 1 \mu\text{m}^{-2}$ to facilitate single-particle characterization and to minimize interparticle LSPR coupling. Structural characterization was performed using a transmission electron microscope (TEM; H-8100, HITACHI, JAPAN) and a scanning electron microscope (SEM; JSM-6500, JEOL, JAPAN).

Cell Culture

The HeLa cells were placed in a cell culture flask and grown in a cell culture medium supplemented with 10% FBS in a cell culture incubator (37°C, 5% CO₂) for 24 h. For sub-culturing, 200 μL of the cell suspension was transferred to a 22 \times 22 mm² No. 1.5 poly-L-lysine-coated coverslip (Corning, NY) and stored in a Petri dish, which was then incubated for 1 h to allow the cells to attach to the coverslip. The coverslip was covered with 1.5 mL of the cell culture medium containing 10% FBS supplement, and the Petri dish was placed in the incubator for 24 h.

DF Microscopy and Spectroscopy

DF microscopy was performed under a Nikon inverted microscope (ECLIPSE

Ti-U). In DF mode, the microscope utilized a Nikon Plan Fluor 100× 0.5–1.3 oil iris objective and a Nikon DF condenser. An Andor iXon^{EM+} CCD camera (iXon Ultra 897) was employed to record DF images of AuNRs@mSiO₂, which were analyzed using Image J. DF scattering spectra were measured and captured using an Andor spectrometer (SHAMROCK 303i, SR-303I-A) and an Andor CCD camera (Newton DU920P-OE). The scanning stage moved the sample to the desired location so that only the scattered light from the selected location was collected by the objective for spectral measurement. The scattered light was directed to the entrance of the spectrometer, dispersed by a grating (300 l/mm), and detected by the Newton CCD camera. The background was measured at a region without any particles. Data analysis was performed with specially designed MATLAB programs.

Differential Interference Contrast Microscopy

DIC microscopy was performed using a Nikon inverted microscope (ECLIPSE Ti-U) comprising two Nomarski prisms, two polarizers, and a quarter waveplate. The samples were illuminated through an oil immersion condenser (numerical aperture (NA) = 1.4). The signals that passed through the sample were collected using a Plan Apo oil-immersion objective (100×, NA = 1.4). A bandpass filter with a 720-nm central range (full width at half maximum, ±5 nm) was obtained from Thorlabs (Newton, NJ, USA) and inserted into the beam path of the microscope to illuminate the samples. A rotational study was conducted at 720 nm excitation by rotating the stage 10° per step for single AuNRs@mSiO₂. The fixed AuNRs@mSiO₂

were positioned in different orientations as the stage was rotated. The Andor iXon^{EM+} CCD camera was used to record highly detailed DIC images of the AuNRs@mSiO₂, which were analyzed using Image J

3.3.4 Result and Discussion

TEM images of single AuNRs@mSiO₂ are shown in **Fig. 27A**. The average width and length of AuNRs@mSiO₂ were 40 nm and 120 nm, respectively. In the ultraviolet–visible light extinction spectrum of AuNRs@mSiO₂ dispersed in water, shown in **Fig. 27B**, the transverse and longitudinal LSPR peaks were observed at 526 and 723 nm, respectively. The thickness of silica shell was approximately 18 nm.

We performed single-particle measurements to understand the scattering properties of AuNRs@mSiO₂ and eliminated the effect of averaging under DF scattering microscopy and spectroscopy. The AuNRs@mSiO₂ were illuminated with a randomly polarized white light tightly focused using a high NA oil condenser under DF microscopy. A DF scattering image of two AuNRs@mSiO₂ (labeled as AuNR1@mSiO₂ and AuNR2@mSiO₂ and marked with yellow squares) deposited on a glass slide are shown in **Fig. 28A**; single particle scattering spectra of the two highlighted nanorods are shown in **Fig. 28B**. The LSPR wavelength of the single AuNRs@mSiO₂ in the single-particle spectra appeared at 690–760 nm, which can be ascribed to heterogeneity in particle size. This result from the single-particle measurements is consistent with the result from the ensemble experiments shown in **Fig. 27B**.

DIC microscopy is better suited to probe orientation and rotational motion of nanoprobe in live cells.^{3, 19-21} DIC microscopy resolves the optical path difference between two mutually orthogonally polarized beams separated by a shear distance along the optical axis of a Nomarski prism, making it insensitive to scattered light from surrounding cellular components while maintaining its high-throughput capability. Therefore, the DIC microscopy-based single-particle rotational tracking technique is effectively used in studies of the rotational dynamics in live cells.

The optical properties of single AuNRs@mSiO₂ fixed on a glass slide were then examined under DIC microscopy at 720-nm excitation close to their longitudinal LSPR wavelength; a DIC image of single AuNRs@mSiO₂ on a glass slide at 720 nm is shown in **Fig. 28A**. The orientation of the AuNR core inside the silica shell was defined as the orientation angle φ between the longitudinal axis of AuNR and dark axis, as shown in the inset of **Fig. 29A**. The orientation angle increased in the counterclockwise direction toward the bright axis. Different DIC image patterns of single AuNRs@mSiO₂ were observed owing to their spatial orientation on the glass slide; i.e., a bright image pattern was observed for AuNR3@mSiO₂ since it was aligned parallel to the bright polarization axis ($\varphi = 90^\circ$, blue arrow), whereas a dark image pattern was observed for AuNR4@mSiO₂. Therefore, DIC microscopy facilitated orientation-dependent DIC image patterns of single AuNRs@mSiO₂ to be observed with high contrast and sensitivity. The scattering spectrum of the AuNR3@mSiO₂ highlighted by a yellow square in **Fig. 29A** was obtained to confirm that it was a single nanoparticle rather than an aggregate and is shown in **Fig. 29B**. The measured

longitudinal LSPR peak of AuNR3@mSiO₂ appeared at 720 nm, which is consistent with the single-particle spectra in **Fig. 29B**. Next, polarization-dependent DIC imaging was performed for the fixed AuNR3@mSiO₂ at an excitation of 720 nm by rotating the stage 10° per step to position AuNR3@mSiO₂ in different orientations. The complete set of obtained DIC images of AuNR3@mSiO₂ from 0° to 180° at intervals of 10° is shown in **Fig. 29C**, where the image patterns periodically changed as a function of the rotation angle.

The normalized DIC intensities of AuNR3@mSiO₂ for two bright (blue) and dark (red) polarization directions were then plotted as a function of rotation angle in **Fig. 30A** to gain a deeper insight into the polarization dependence. As the stage was rotated, the DIC bright (red) and dark (blue) intensity curves were anti-correlated, i.e., an increase in the bright intensity was accompanied by a decrease in the dark intensity, and vice versa. These observed polarization-sensitive, periodic DIC images and intensities of single AuNRs@mSiO₂ indicate that the spatial orientation of single AuNRs@mSiO₂ can be determined via DIC microscopy and polarization anisotropy.

DIC polarization anisotropy using an intensity ratio instead of absolute intensities is less affected by intensity instabilities and can thus provide more accurate, reproducible, and reliable angle measurements.^{1, 3, 15} The DIC polarization anisotropy P can be obtained from the bright and dark intensities of a single DIC image of the AuNR@mSiO₂, as¹⁵

$$P = \frac{I_{B,N} - I_{D,N}}{I_{B,N} + I_{D,N}} \quad (5)$$

where $I_{B,N}$ and $I_{D,N}$ are the normalized bright and dark intensities, respectively. The

calculated DIC polarization anisotropy P of AuNR3@mSiO₂ as a function of orientation angle φ is shown in **Fig. 30B**, where the DIC polarization anisotropy P oscillated between minimum and maximum values of -1 and $+1$ depending on the orientation. P reached the maximum value of $+1$ when AuNR3@mSiO₂ was aligned parallel to the bright axis. As shown in **Fig. 30B**, the experimental P values obtained from Eq. (5) agreed well with the calculated P values, thereby validating that DIC polarization anisotropy allows for accurate measurements of the orientation angles of single AuNRs@mSiO₂. The DIC polarization anisotropy P can be related to the orientation angle φ , as

$$\varphi = \arccos\left(\sqrt{\frac{A - \sqrt{A^2 - 2A}}{2}}\right), \quad P < 0 \quad (7)$$

$$\varphi = \arccos\left(\sqrt{\frac{A + \sqrt{A^2 - 2A}}{2}}\right), \quad P > 0$$

where A is defined as $(P - 1)/P$. Thus, the orientation angle φ can be obtained from a measured DIC polarization anisotropy P .

The next crucial step was to verify that single AuNRs@mSiO₂ could be used as high-contrast multifunctional orientation probes in dynamic biological environments under DIC microscopy. In recent studies, single AuNRs@mSiO₂ have been employed as efficient drug delivery cargoes in biological applications.^{8, 10-12, 22} Tracking rotational and translational dynamics of individual AuNRs@mSiO₂ on live cell membranes will provide a better understanding of drug delivery mechanisms and other cellular processes, such as endocytosis. AuNRs@mSiO₂ rotating on live cell

membranes were thus used as a model system to verify their use as multifunctional orientation probes in dynamic biological systems.

The rotational motions of surface-bound AuNRs@mSiO₂ were recorded at a temporal resolution of 100 ms under DIC microscopy, as shown in **Fig. S13**. The AuNR5@mSiO₂ rotated quickly when it first fell on the HeLa cell membrane, as revealed by an image flicker. A captured DIC image of AuNR5@mSiO₂ bound to a live cell membrane is shown in **Fig. 31A**. The DIC image patterns changed dynamically as a function of time, as demonstrated by the 20 consecutive frames from recorded movie shown in **Fig. 31B**. The DIC polarization anisotropy P values for these 20 images were randomly distributed between -1 and $+1$, as demonstrated in **Fig. 31C**. More experimental data for AuNR6@mSiO₂ rotating on the live cell membrane are provided in **Fig. S13**. The results support the utility of single AuNRs@mSiO₂ as sensitive orientation probes under DIC microscopy and demonstrate that DIC polarization anisotropy allows precise determination of their real-time orientation during dynamic biological processes.

Further, AuNRs@mSiO₂ present two main advantages over bare AuNRs (no silica shell) that have been conventionally used as orientation probes in biological studies, whose orientation angles can both be obtained with high sensitivity under DIC microscopy. First, AuNRs@mSiO₂ can be used as multifunctional orientation probes because of the added functions compared with the bare AuNR probe.^{23, 24} For example, the mesoporous silica shell in a drug delivery system can provide excellent loading capacity, reduced toxicity, and enhanced stability. Second, as demonstrated in **Fig. 31**,

the Au core inside the silica shell can be used as an orientation probe and a local heat generator to induce phototherapy in biological systems. Therefore, AuNRs@mSiO₂ can be used as multifunctional orientation probes in various biomedical studies

3.3.5 Conclusion

In summary, the optical properties of single AuNRs@mSiO₂ at their LSPR wavelengths under DF and DIC microscopy and their use as orientation probes in dynamic biological systems were examined. Single AuNRs@mSiO₂ showed polarization-sensitive, periodic DIC images and intensities at their LSPR wavelengths with high contrast and sensitivity. The real-time rotational motions of AuNRs@mSiO₂ were tracked on live cell membranes under DIC microscopy to verify the capability of single AuNRs@mSiO₂ as multifunctional orientation probes. The results presented here support the use of single AuNRs@mSiO₂ as sensitive multifunctional optical probes owing to the combined effect of the Au core, which can serve as an orientation probe and a local heat generator for phototherapy, and mesoporous silica shell, which can be used as efficient drug carriers due to its excellent loading capacity in many biological applications

3.3.6 References

1. Ha, J. W.; Sun, W.; Stender, A. S.; Fang, N., Dual-Wavelength Detection of Rotational Diffusion of Single Anisotropic Nanocarriers on Live Cell Membranes. *J. Phys. Chem. C* **2012**, *116* (4), 2766.
2. Ma, Z.; Xia, H.; Liu, Y.; Liu, B.; Chen, W.; Zhao, Y., Applications of gold nanorods in biomedical imaging and related fields. *Chinese Science Bulletin* **2013**, *58* (21), 2530-2536.
3. Xiao, L.; Ha, J. W.; Wei, L.; Wang, G.; Fang, N., Determining the Full Three-Dimensional Orientation of Single Anisotropic Nanoparticles by Differential Interference Contrast Microscopy. *Angew. Chem., Int. Ed.* **2012**, *51* (31), 7734.
4. Ali, M. R. K.; Wu, Y.; El-Sayed, M. A., Gold-Nanoparticle-Assisted Plasmonic Photothermal Therapy Advances Toward Clinical Application. *The Journal of Physical Chemistry C* **2019**, *123* (25), 15375-15393.
5. Zan, M.; Li, J.; Huang, M.; Lin, S.; Luo, D.; Luo, S.; Ge, Z., Near-infrared light-triggered drug release nanogels for combined photothermal-chemotherapy of cancer. *Biomaterials Science* **2015**, *3* (7), 1147-1156.
6. Wu, X.; Liu, J.; Yang, L.; Wang, F., Photothermally controlled drug release system with high dose loading for synergistic chemo-photothermal therapy of multidrug resistance cancer. *Colloids and Surfaces B: Biointerfaces* **2019**, *175*, 239-247.
7. Wan, J.; Wang, J.-H.; Liu, T.; Xie, Z.; Yu, X.-F.; Li, W., Surface chemistry but not aspect ratio mediates the biological toxicity of gold nanorods in vitro

and in vivo. *Scientific Reports* **2015**, *5* (1), 11398.

8. Li, C.; Feng, K.; Xie, N.; Zhao, W.; Ye, L.; Chen, B.; Tung, C.-H.; Wu, L.-Z., Mesoporous Silica-Coated Gold Nanorods with Designable Anchor Peptides for Chemo-Photothermal Cancer Therapy. *ACS Applied Nano Materials* **2020**, *3* (6), 5070-5078.

9. Ha Lien, N. T.; Phan, A. D.; Van Khanh, B. T.; Thuy, N. T.; Trong Nghia, N.; My Nhung, H. T.; Hong Nhung, T.; Quang Hoa, D.; Duong, V.; Minh Hue, N., Applications of Mesoporous Silica-Encapsulated Gold Nanorods Loaded Doxorubicin in Chemo-photothermal Therapy. *ACS Omega* **2020**, *5* (32), 20231-20237.

10. Liu, G.; Liang, H.; He, Y.; Lu, L.; Wang, L.; Liu, P.; Cai, K., A nanoplatform based on mesoporous silica-coated gold nanorods for cancer triplex therapy. *Journal of Materials Chemistry B* **2020**, *8* (42), 9686-9696.

11. Liu, J.; Detrembleur, C.; De Pauw-Gillet, M.-C.; Mornet, S.; Jérôme, C.; Duguet, E., Gold Nanorods Coated with Mesoporous Silica Shell as Drug Delivery System for Remote Near Infrared Light-Activated Release and Potential Phototherapy. *Small* **2015**, *11* (19), 2323-2332.

12. Monem, A. S.; Elbially, N.; Mohamed, N., Mesoporous silica coated gold nanorods loaded doxorubicin for combined chemo-photothermal therapy. *International Journal of Pharmaceutics* **2014**, *470* (1), 1-7.

13. Sönnichsen, C.; Alivisatos, A. P., Gold Nanorods as Novel Nonbleaching Plasmon-Based Orientation Sensors for Polarized Single-Particle Microscopy. *Nano*

Letters **2005**, 5 (2), 301-304.

14. Chang, W.-S.; Ha, J. W.; Slaughter, L. S.; Link, S., Plasmonic nanorod absorbers as orientation sensors. *Proceedings of the National Academy of Sciences* **2010**, 107 (7), 2781-2786.

15. Won Ha, J.; Sun, W.; Wang, G.; Fang, N., Differential interference contrast polarization anisotropy for tracking rotational dynamics of gold nanorods. *Chemical Communications* **2011**, 47 (27), 7743-7745.

16. Ha, J. W.; Marchuk, K.; Fang, N., Focused Orientation and Position Imaging (FOPI) of Single Anisotropic Plasmonic Nanoparticles by Total Internal Reflection Scattering Microscopy. *Nano Lett.* **2012**, 12 (8), 4282.

17. Marchuk, K.; Fang, N., Three-Dimensional Orientation Determination of Stationary Anisotropic Nanoparticles with Sub-Degree Precision under Total Internal Reflection Scattering Microscopy. *Nano Lett.* **2013**, 13 (11), 5414.

18. Marchuk, K.; Ha, J. W.; Fang, N., Three-Dimensional High-Resolution Rotational Tracking with Superlocalization Reveals Conformations of Surface-Bound Anisotropic Nanoparticles. *Nano Letters* **2013**, 13 (3), 1245-1250.

19. Gu, Y.; Ha, J. W.; Augspurger, A. E.; Chen, K.; Zhu, S.; Fang, N., Single Particle Orientation and Rotational Tracking (SPORT) in biophysical studies. *Nanoscale* **2013**, 5 (22), 10753-10764.

20. Gu, Y.; Sun, W.; Wang, G.; Fang, N., Single Particle Orientation and Rotation Tracking Discloses Distinctive Rotational Dynamics of Drug Delivery Vectors on Live Cell Membranes. *Journal of the American Chemical Society* **2011**, 133

(15), 5720-5723.

21. Wang, G.; Sun, W.; Luo, Y.; Fang, N., Resolving Rotational Motions of Nano-objects in Engineered Environments and Live Cells with Gold Nanorods and Differential Interference Contrast Microscopy. *Journal of the American Chemical Society* **2010**, *132* (46), 16417-16422.

22. Song, Z.; Liu, Y.; Shi, J.; Ma, T.; Zhang, Z.; Ma, H.; Cao, S., Hydroxyapatite/mesoporous silica coated gold nanorods with improved degradability as a multi-responsive drug delivery platform. *Materials Science and Engineering: C* **2018**, *83*, 90-98.

23. Kim, G. W.; Lee, S. Y.; Ha, J. W., Three-dimensional defocused orientation sensing of single bimetallic core-shell gold nanorods as multifunctional optical probes. *Analyst* **2017**, *142* (6), 899.

24. Lee, S. Y.; Ha, J. W., Characterizing the optical properties of single palladium-coated core-shell gold nanorods as multifunctional orientation probes. *Physical Chemistry Chemical Physics* **2016**, *18* (48), 32682-32685.

3.3.7 Figures and Captions

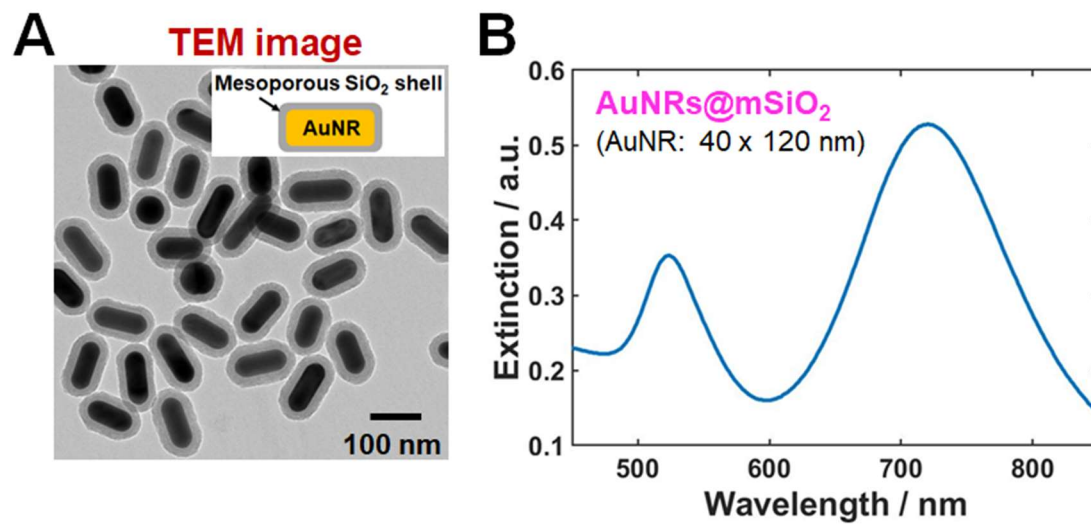


Figure 27. (A) TEM image of AuNRs@mSiO₂. The average length and width are 120 and 40 nm. The inset illustrates the AuNRs@mSiO₂. (B) Normalized ultraviolet–visible (UV–Vis) extinction spectrum of AuNRs@mSiO₂ dispersed in water.

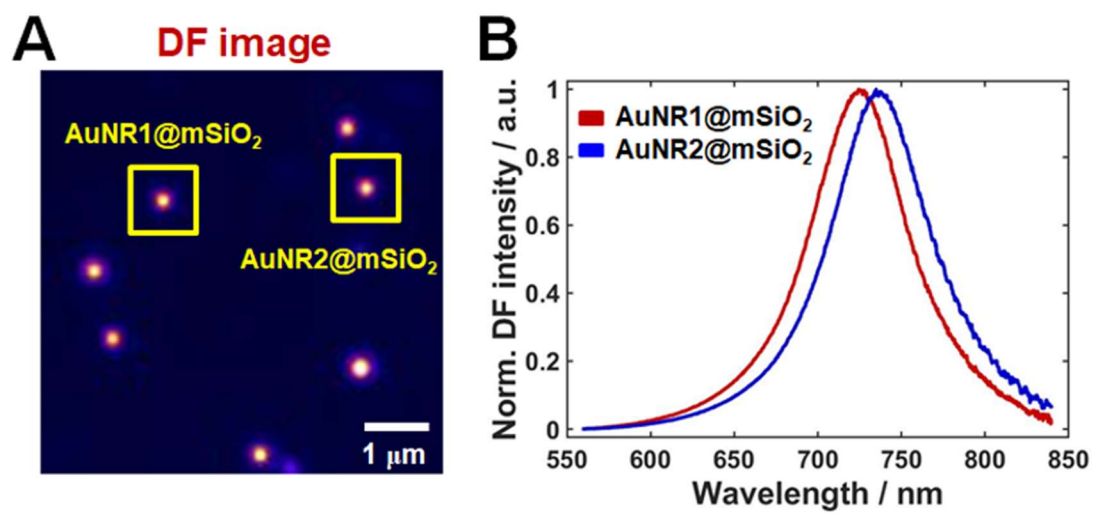


Figure 28. (A) DF image of single AuNRs@mSiO₂ on a glass slide. (B) Single-particle scattering spectra of the two AuNRs@mSiO₂ (AuNR1@mSiO₂, AuNR2@mSiO₂) marked with a yellow square in (A).

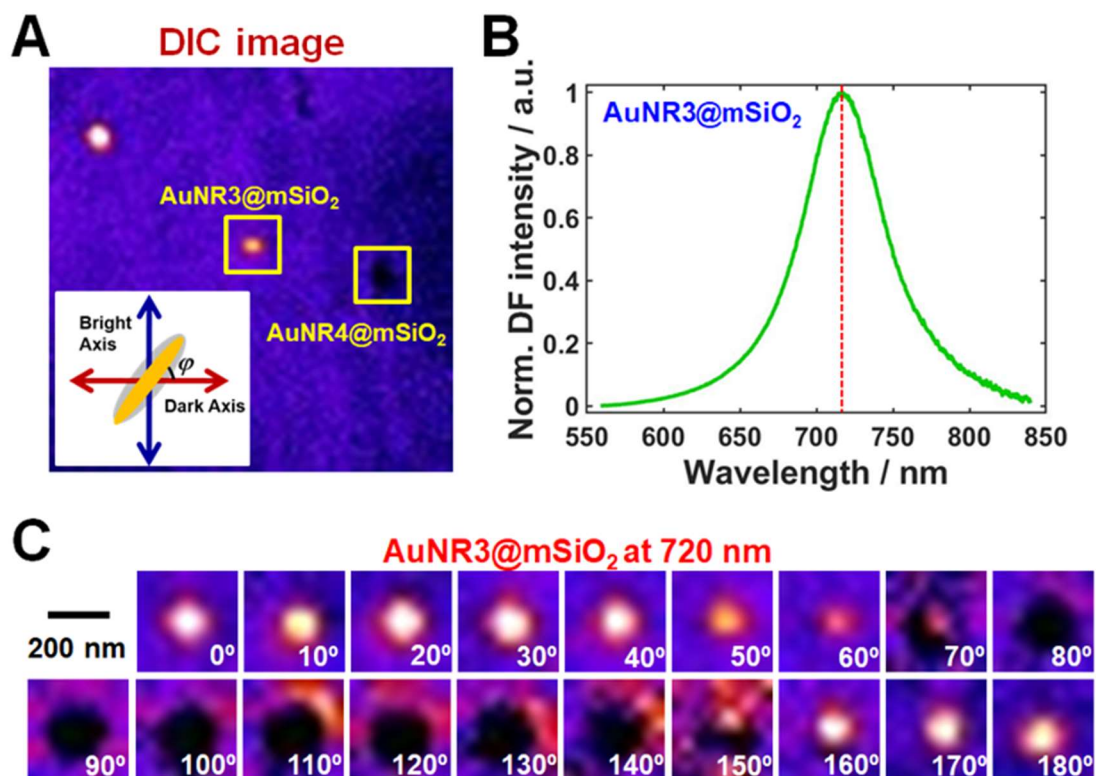


Figure 29. (A) DIC image of single AuNRs@mSiO₂ with different orientations on a glass slide. The AuNRs@mSiO₂ were illuminated at their longitudinal SPR wavelength of 720 nm. The inset represents the definition of the orientation angle φ of a AuNR@mSiO₂ with respect to the dark polarization axis. (B) Single-particle scattering spectrum of AuNR3@mSiO₂, highlighted by the yellow square in (A). The longitudinal SPR peak was observed at approximately 720 nm. (C) Polarization-dependent DIC images of single AuNR3@mSiO₂ obtained by rotating the stage in increments of 10° at 720 nm excitation.

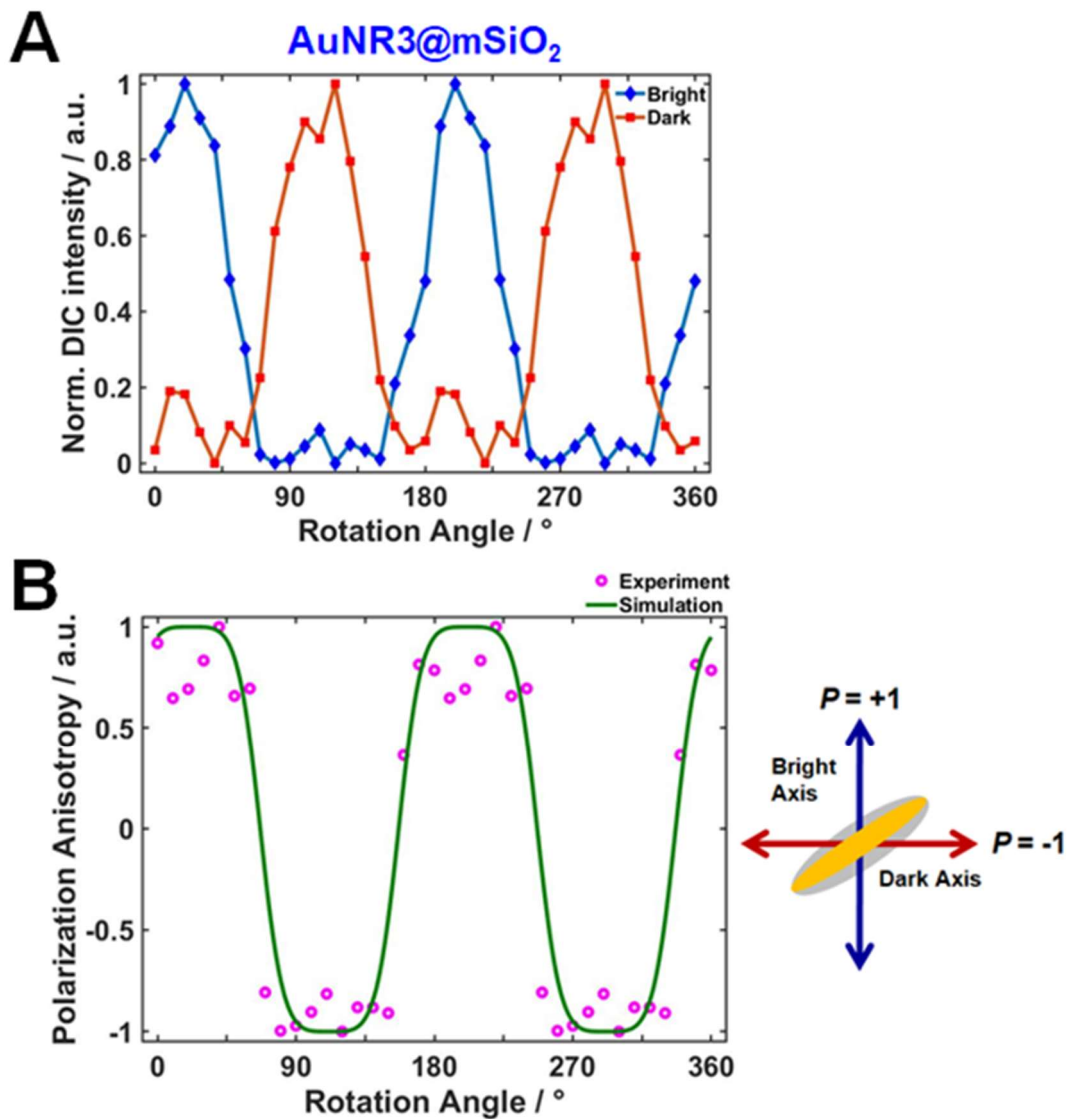


Figure 30. (A) DIC intensity profiles and (B) polarization anisotropy P of AuNR3@mSiO₂ as a function of rotation angle. In (B), the experimental values of P (pink dots) fit the calculated P values well (green curve).

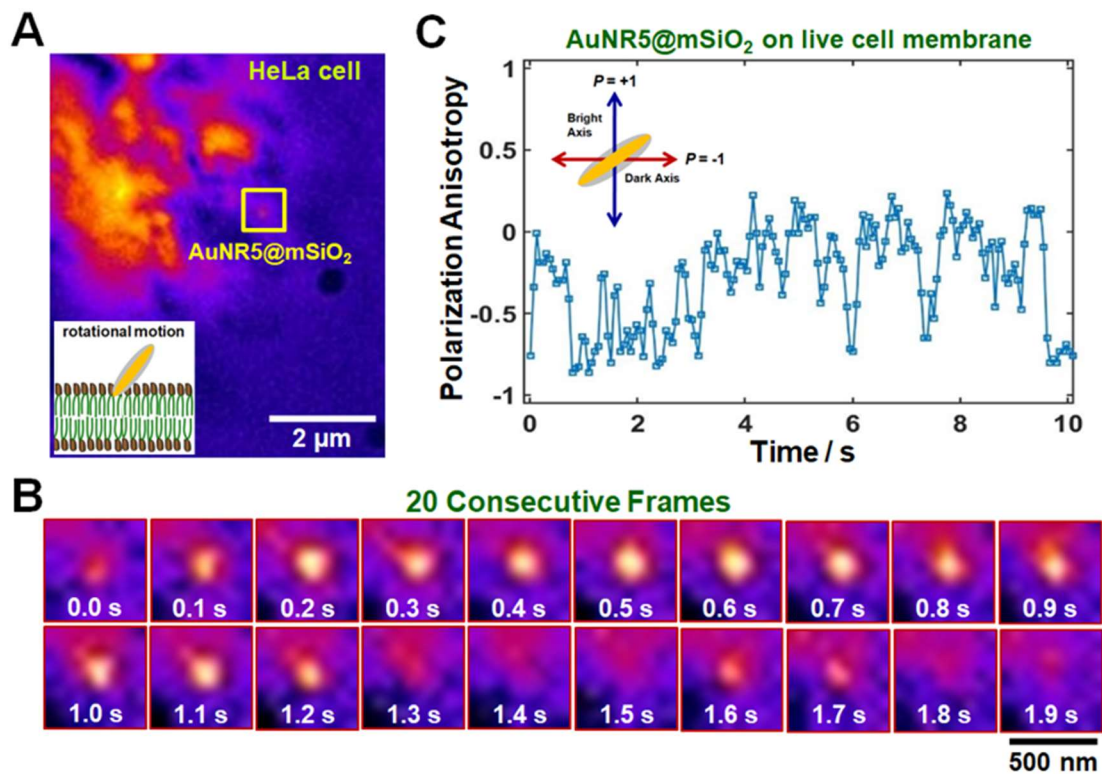


Figure 31. (A) DIC image of AuNR5@mSiO₂ bound onto a live cell membrane. (B) 20 successive DIC images of AuNR5@mSiO₂ chosen from recorded movie. The temporal resolution was 100 ms. (C) DIC polarization anisotropy P for AuNR5@mSiO₂ as a function of time for all consecutive frames in recorded movie.

3.3.8 Supplementary Materials

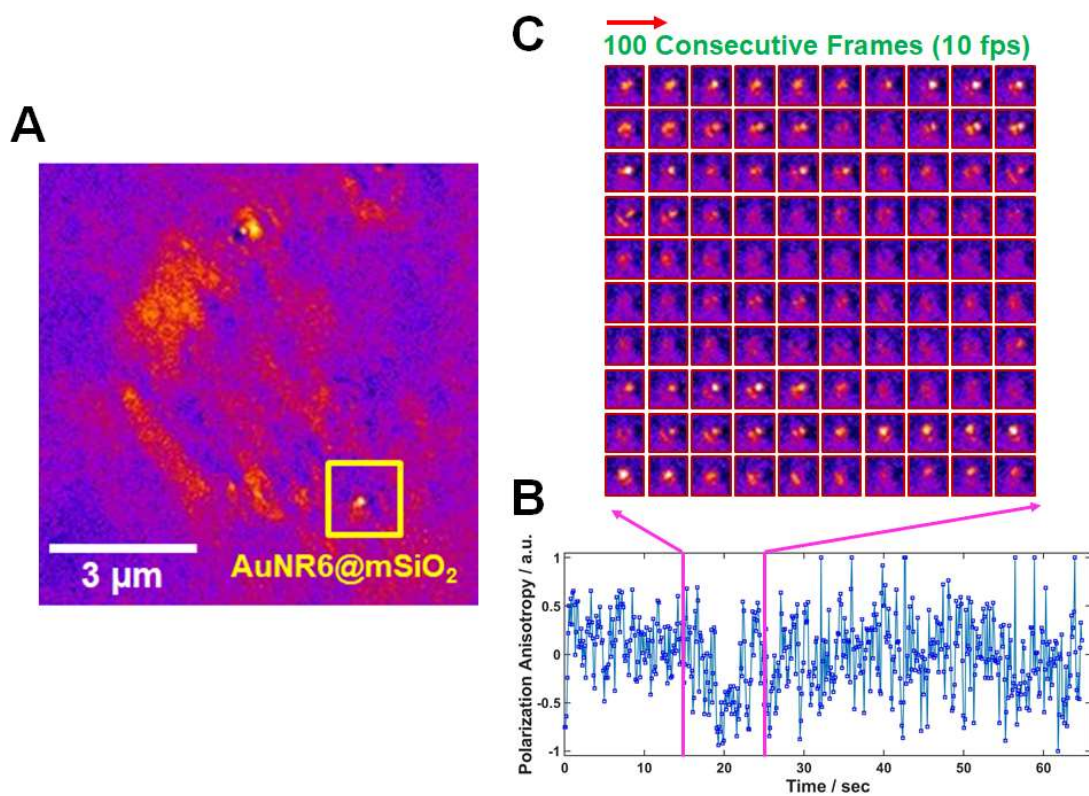


Figure S13. (A) DIC image of AuNR6@mSiO₂ bound onto a live cell membrane. (B) DIC polarization anisotropy P for AuNR6@mSiO₂ as a function of time for all consecutive frames. (C) 100 successive DIC images of AuNR6@mSiO₂ chosen from all consecutive frames in (B). The temporal resolution was 100 ms.

Chapter 4. Structural and Spectral Changes of AuNPs Physical and Chemical Reaction

4.1 Single-particle study: effects of oxygen plasma treatment on structural and spectral changes of anisotropic gold nanorods

Geun Wan Kim and Ji Won Ha*

A paper published in *Physical Chemistry Chemical Physics*, **2020**, 22, 11767.

Reproduced by permission of the Royal Society of Chemistry

*Corresponding author

4.1.1 Abstract

Oxygen plasma treatment is a common method for removing the surfactant capping material from gold nanoparticles, improving their functionalization and lowering their cytotoxicity for biological studies. This single-particle study investigates the effects of oxygen plasma treatment on the structural and localized surface plasmon resonance (LSPR) spectral variations of anisotropic gold nanorods (AuNRs). Single AuNRs subjected to different plasma treatment times were characterized by scanning electron microscopy and dark-field microscopy. The AuNR length was a gradually decreasing function of plasma treatment time. After 120 s of plasma treatment, the aspect ratio of the AuNRs was reduced by a major structural deformation. Furthermore, increasing the plasma treatment time gradually broadened the LSPR linewidth of the single AuNRs. This trend was attributed to the decreased aspect ratio and the increased plasmon damping. These results provide vital and

fundamental information on the relationship among plasma treatment time, structural change, and LSPR damping at the single-particle level.

4.1.2 Introduction

Localized surface plasmon resonance (LSPR), defining the coherent oscillations of free electrons in the conduction band of noble metallic structures, has attracted considerable interest for its signature optical properties.¹⁻⁴ In particular, plasmonic gold nanoparticles (AuNPs) have the advantages of biocompatibility,⁵ high photo-stability,^{6, 7} chemical and physical stability,⁸ and easy surface modification or functionalization⁹ with biological molecules. Anisotropic AuNPs have been widely applied in biological and chemical sensing,^{10, 11} bioimaging,^{12, 13} surface-enhanced Raman spectroscopy,¹³⁻¹⁵ plasmon-enhanced fluorescence,¹⁶ energy harvesting,^{17, 18} catalysis,¹⁵ and biomedical therapies.^{19, 20}

Anisotropic AuNPs such as gold nanorods (AuNRs),²¹ nanobipyramids,²² nanourchins,¹¹ nanostars,²³ and triangular nanoplates²⁴ have been widely studied, as their shapes induce unique optical properties. In previous studies, anisotropic AuNPs have been mainly investigated at the ensemble level, which provides only the averaged spectral information of individual nanoparticles with inherent inhomogeneity or polydispersity. This limitation of ensemble averaging can be overcome by advanced experimental and simulation techniques. Recent advances in single-particle spectroscopy techniques can deepen our understanding of the optical properties of AuNPs.²⁵

Anisotropic AuNPs are synthesized with various surfactants that lower their polydispersity and allow determination of their geometry. The surfactant also prevents aggregation of the synthesized AuNPs by colloidally stabilizing their surfaces. A common surfactant, especially for AuNRs, is cetyltrimethylammonium (CTAX), where $X = Cl^-$ or Br^- . However, the CTAX bilayer interrupts further functionalization of the AuNR surface, and its high cytotoxicity²⁶ is unsuitable for intracellular uses. Therefore, in biological studies, the surface capping material is often removed by oxygen plasma treatment and the CTAX bilayer is replaced with other polymer and biological molecules.²⁷⁻³⁰ So far, the structural instability and morphological transitions of AuNRs upon heating have been investigated.³¹⁻³⁵ At present, however, how the oxygen plasma treatment affects the structural and spectral changes of single AuNRs is poorly understood. To better understand the relationship among the plasma treatment time, structural change, and LSPR linewidth broadening at the single-particle level, further studies are required.

In the present study, we treated AuNRs on a substrate with oxygen plasma and monitored their structural and spectral changes after various treatment times by using scanning electron microscopy (SEM) and dark-field (DF) microscopy and spectroscopy. We first present the AuNR size as a function of plasma exposure time using SEM imaging analysis. We then demonstrate the linewidth variations in the LSPR of single particle scattering spectra after different plasma exposure times. The LSPR linewidth is quantified by its full width at half maximum (FWHM).

4.1.3 Experimental Section

Materials and Sample Preparation

CTAB-stabilized AuNRs with an average size of 25 nm × 73 nm were obtained from Nanopartz (Loveland, CO, USA). The AuNR colloid solution was diluted with 18.2-M Ω pure water to the proper concentration and the diluted solution was sonicated for 15 min at room temperature to avoid the NR aggregation. The samples were then prepared by drop casting a diluted solution containing AuNRs on the pre-cleaned glass slide. Afterward, a 20 mm × 20 mm no. 1.5 coverslip (Corning, NY) was placed on the glass slide.

Structural Characterizations

After the AuNR samples were treated with oxygen plasma, structural characterizations of CTAB-stabilized AuNRs were carried out using a scanning electron microscope (SEM, JSM6500F, JEOL, Japan). Then, we checked the structural changes of single AuNRs from SEM images and determined their length and diameter.

Oxygen Plasma Treatment

Oxygen plasma treatment is commonly used for removing CTAB capping material coated on the surface of AuNRs. In this study, the oxygen plasma treatment was performed using a plasma cleaner (PDC-32G-2, Harrick plasma, U.S.A.). All oxygen plasma treatments were carried out with a maximum RF power of 18W at various plasma treatment times.

Scattering-Based Dark-Field Microscopy

DF images were obtained under a Nikon inverted microscope (ECLIPSE Ti-U). In DF mode, we utilized a Nikon Plan Fluor 100× 0.5-1.3 oil iris objective and a Nikon DF condenser. An Andor iXon^{EM+} CCD camera (iXon Ultra 897, UK) was used to obtain the DF images of the AuNRs. In this study, collected images were analyzed with Image J and Matlab.

Single Particle Scattering Spectroscopy

DF scattering spectra were acquired with an Andor spectrophotometer (SHAMROCK 303i, SR-303I-A) connected with an Andor CCD camera (Newton DU920P-OE). When obtaining a spectrum, the scanning stage moved the sample to the desired location so that only scattered light from the selected location was collected by the objective. The scattered light was directed to the entrance of the spectrophotometer, dispersed by a grating (300 l/mm), and detected by the Newton CCD camera. The background was measured at a region without any particles. Data analysis was performed with specially designed Matlab programs.

4.1.4 Results and Discussion

The AuNRs (average size 25 nm × 73 nm) were purchased from Nanopartz (Loveland, CO, USA). **Fig. S14** shows a UV-vis extinction spectrum of the AuNRs dispersed in distilled water. Characteristic transverse and longitudinal LSPR peaks are present at approximately 521 nm and 702 nm, respectively. In this study, AuNRs were

chosen for two main reasons. First, they are widely used in many applications, such as biosensing and bio-imaging, and their surfaces are easily modified by other biomolecules through thiol chemistry. Second, the optical properties of AuNRs can be conveniently tuned from visible to near-IR by controlling their aspect ratios (ARs). Furthermore, the longitudinal LSPR peak is very sensitive to structural and AR changes.

Oxygen plasma treatment is commonly used for cleaning, surface activation, and etching of AuNRs. For example, plasma treatment removes the surfactant capping material from AuNRs. Furthermore, Winkler et al. described the morphological changes of gold nanoparticles (~ 5 nm in diameter) due to adsorption onto a silicon substrate and low-power oxygen plasma treatment.³⁶ During the plasma treatment, the gold nanoparticles behave like droplets of a non-wetting liquid.³⁶ However, the effect of treatment time on the structural changes of anisotropic AuNRs is largely unknown at the single-particle level. To acquire this understanding, the present study attempts to elucidate the structural effects of high-power oxygen plasma treatment on anisotropic AuNRs capped with a surfactant bilayer (CTAB), which colloiddally stabilizes the AuNRs in solution. After drop-casting the solution on a pre-cleaned glass slide, the CTAB-capped AuNRs were deposited as shown in **Fig. 32A**. The sample was placed in an oxygen plasma cleaner, where the CTAB was removed by oxygen plasma treatment (**Fig. 32B**).

To characterize the structural changes of the AuNRs after oxygen plasma treatment, we obtained SEM images of AuNRs treated for different times. The SEM

images in **Fig. 33** show the size and shape changes of the AuNRs after plasma treatment times of 0, 5, 10, 30, 60, 120, 180, 300, and 1800 s. From the obtained SEM images, we characterized the plasma-induced structural and size changes of the AuNRs and constructed length and diameter of the AuNRs. Before the oxygen plasma treatment, the average diameter and length of the particles were 23.5 (± 1.70) nm and 69.6 (± 6.19) nm, respectively, giving an AR of 2.96. After treatment with oxygen plasma for 120 s, the diameter and length reduced to 22.5 (± 2.15) nm and 64.3 (± 9.98) nm (120 s), respectively, giving an AR of 2.86.

Other important observations in different oxygen plasma treatment time (**Fig. 33**) require further discussion. First, the oxygen plasma treatment induced structural changes in the AuNRs. In particular, both the length and diameter of the AuNRs decreased with increasing plasma treatment time, but the structural change was greater along the length (or longitudinal axis) than across the diameter (or transverse axis) of the particles. Second, a major structural change appeared between the plasma treatment times of 120 and 180 s. As shown in **Fig. S15**, the size and shape of the AuNRs greatly changed after 180 s of plasma treatment, and the length remarkably reduced from 64.3 nm (at 120 s) to 61.6 nm. In contrast, the transverse length increased from 22.5 nm (at 120 s) to 25.3 nm (at 180 s). The AuNRs appeared to have melted after 180 s of plasma treatment, and their size was little altered by longer plasma treatments (**Fig. S15**). Precisely, at oxygen plasma treatment times exceeding 120 s, the AuNRs deformed into structures with shorter lengths and larger diameters (or lower ARs, as shown in **Fig. S15B**). This result suggests that by controlling the ARs with

oxygen plasma treatment, we can change the size of AuNRs and tune their optical properties.

Besides the structural characterization using SEM, we elucidated the LSPR spectral variations of the AuNRs after different plasma treatment times by using single-particle microscopy and spectroscopy. In particular, we focused on the LSPR linewidths (FWHM) of the single-particle spectra, which provided insights into plasmon damping in single AuNRs. Plasmon damping is closely related to plasmon energy loss, which greatly reduces the scattering intensity and broadens the linewidth of LSPR.^{22, 37, 38} To the best of our knowledge, the relationship between oxygen plasma treatment time and the plasmon damping degree of single AuNR particles has not been previously reported.

In this study, the concentration of AuNRs deposited on the glass slide was controlled to be approximately $1 \mu\text{m}^{-2}$ in order to facilitate single particle characterization and to minimize inter-particle LSPR coupling, resulting in spectral shifts. The DF scattering images and spectra of single AuNRs were obtained at oxygen plasma treatment times of 0, 5, 10, 30, 60, 120, 180, 300, and 1800 s. Panels A and B of **Fig. 34** show DF scattering images before the oxygen plasma treatment and after 1800 s of treatment, respectively. **Fig. 34C** compares the single-particle scattering spectra of particles AuNR1 and AuNR2, highlighted by the yellow-edged squares in the DF images (**Fig. 34C**). Furthermore, the scattering spectra were well fitted with the Lorentzian function used to obtain the homogeneous LSPR linewidth and LSPR wavelength. After 30 minutes of plasma treatment, the FWHM of the LSPR spectrum

was broadened by strong plasmon damping. This LSPR linewidth broadening is ascribed to the decreased length and AR of the AuNRs (see **Fig. S15**), consistent with our previous result in which the LSPR linewidth increased with decreasing AR of single AuNRs.

To better understand the increase in LSPR linewidth with plasma treatment time, we analyzed the single particle scattering spectra of AuNRs measured at different treatment times. **Fig. 35** plots the LSPR linewidth broadening versus plasma treatment time, obtained from the single-particle DF scattering spectra of many AuNRs. The LSPR linewidth is an increasing function of plasma treatment time and exhibited an abrupt change from 120 s to 180 s, consistent with the SEM characterization results (**Fig. 33 and Fig. S15**). Up to 120 s of plasma treatment, the LSPR linewidths remained almost constant despite the removal of the CTAB capping material from the AuNR surfaces. After 180 s, the large broadening of the LSPR linewidth reflected the large structural change of the AuNRs. **Fig. S16** shows the variation of the LSPR wavelength as a function of the plasma treatment time. Therefore, oxygen plasma treatment, which is commonly used to remove capping material for surface modification in biological studies, must be carefully timed.

4.1.5 Conclusion

In summary, we investigated the effects of oxygen plasma treatment on the structural and LSPR spectral changes of anisotropic AuNRs by using SEM and single-particle DF microscopy. The oxygen plasma treatment induced structural changes in

the AuNRs and a large deformation manifesting as a decreased AR occurred after 120–180 s of treatment. As the plasma treatment time increased, the LSPR linewidth increased as the plasmons were damped by the structural deformation and decreased AR of the AuNRs. These findings were consistent with the SEM characterization results. The results suggest that the optical properties of AuNRs can be altered by controlling their ARs using oxygen plasma treatment. Furthermore, this single-particle study provides a fundamental understanding of the relationship among the oxygen plasma treatment time and the structural and spectral changes of AuNRs.

4.1.6 References

1. Novotny, L.; van Hulst, N., Antennas for light. *Nature Photonics* **2011**, *5* (2), 83-90.
2. Schuller, J. A.; Barnard, E. S.; Cai, W.; Jun, Y. C.; White, J. S.; Brongersma, M. L., Plasmonics for extreme light concentration and manipulation. *Nature Materials* **2010**, *9* (3), 193-204...
3. Willets, K. A.; Duyne, R. P. V., Localized Surface Plasmon Resonance Spectroscopy and Sensing. *Annual Review of Physical Chemistry* **2007**, *58* (1), 267-297.
4. Li, Y.; Jing, C.; Zhang, L.; Long, Y.-T., Resonance scattering particles as biological nanosensors in vitro and in vivo. *Chemical Society Reviews* **2012**, *41* (2), 632-642.
5. Murphy, C. J.; Gole, A. M.; Stone, J. W.; Sisco, P. N.; Alkilany, A. M.; Goldsmith, E. C.; Baxter, S. C., Gold Nanoparticles in Biology: Beyond Toxicity to Cellular Imaging. *Accounts of Chemical Research* **2008**, *41* (12), 1721-1730.
6. Sperling, R. A.; Rivera Gil, P.; Zhang, F.; Zanella, M.; Parak, W. J., Biological applications of gold nanoparticles. *Chemical Society Reviews* **2008**, *37* (9), 1896-1908.
7. Wu, X.; Yeow, E. K. L., Fluorescence blinking dynamics of silver nanoparticle and silver nanorod films. *Nanotechnology* **2007**, *19* (3), 035706.
8. Lee, D.-E.; Koo, H.; Sun, I.-C.; Ryu, J. H.; Kim, K.; Kwon, I. C., Multifunctional nanoparticles for multimodal imaging and theragnosis. *Chemical*

Society Reviews **2012**, 41 (7), 2656-2672.

9. Sperling, R. A.; Parak, W. J., Surface modification, functionalization and bioconjugation of colloidal inorganic nanoparticles. *Philosophical Transactions of the Royal Society A: Mathematical, Physical and Engineering Sciences* **2010**, 368 (1915), 1333-1383.

10. Zhang, C.; Paria, D.; Semancik, S.; Barman, I., Composite-Scattering Plasmonic Nanoprobes for Label-Free, Quantitative Biomolecular Sensing. *Small* **2019**, 15 (38), 1901165.

11. Thapliyal, N. B.; Chiwunze, T. E.; Karpoormath, R.; Cherukupalli, S., Fabrication of highly sensitive gold nanourchins based electrochemical sensor for nanomolar determination of primaquine. *Materials Science and Engineering: C* **2017**, 74, 27-35.

12. Gu, Y.; Ha, J. W.; Augspurger, A. E.; Chen, K.; Zhu, S.; Fang, N., Single Particle Orientation and Rotational Tracking (SPORT) in biophysical studies. *Nanoscale* **2013**, 5 (22), 10753-10764.

13. Zhang, Y.; Qian, J.; Wang, D.; Wang, Y.; He, S., Multifunctional Gold Nanorods with Ultrahigh Stability and Tunability for In Vivo Fluorescence Imaging, SERS Detection, and Photodynamic Therapy. *Angewandte Chemie International Edition* **2013**, 52 (4), 1148-1151.

14. Julien-Rabant, C.; Débarre, A.; Métivier, R.; Laurent, G., Single particle SERS signal on gold nanorods: comparative study of diarylethene photochromic isomers. *Journal of Optics* **2015**, 17 (11), 114018.

15. Zhang, Q.; Large, N.; Nordlander, P.; Wang, H., Porous Au Nanoparticles with Tunable Plasmon Resonances and Intense Field Enhancements for Single-Particle SERS. *The Journal of Physical Chemistry Letters* **2014**, *5* (2), 370-374.
16. Abadeer, N. S.; Brennan, M. R.; Wilson, W. L.; Murphy, C. J., Distance and Plasmon Wavelength Dependent Fluorescence of Molecules Bound to Silica-Coated Gold Nanorods. *ACS Nano* **2014**, *8* (8), 8392-8406.
17. Zhu, G.; Peng, B.; Chen, J.; Jing, Q.; Lin Wang, Z., Triboelectric nanogenerators as a new energy technology: From fundamentals, devices, to applications. *Nano Energy* **2015**, *14*, 126-138.
18. Wang, C. C. D.; Choy, W. C. H.; Duan, C.; Fung, D. D. S.; Sha, W. E. I.; Xie, F.-X.; Huang, F.; Cao, Y., Optical and electrical effects of gold nanoparticles in the active layer of polymer solar cells. *Journal of Materials Chemistry* **2012**, *22* (3), 1206-1211.
19. Giljohann, D. A.; Seferos, D. S.; Daniel, W. L.; Massich, M. D.; Patel, P. C.; Mirkin, C. A., Gold Nanoparticles for Biology and Medicine. *Angewandte Chemie International Edition* **2010**, *49* (19), 3280-3294.
20. Lal, S.; Clare, S. E.; Halas, N. J., Nanoshell-Enabled Photothermal Cancer Therapy: Impending Clinical Impact. *Accounts of Chemical Research* **2008**, *41* (12), 1842-1851.
21. Pérez-Juste, J.; Pastoriza-Santos, I.; Liz-Marzán, L. M.; Mulvaney, P., Gold nanorods: Synthesis, characterization and applications. *Coordination Chemistry Reviews* **2005**, *249* (17), 1870-1901.

22. Lee, S. Y.; Tsalu, P. V.; Kim, G. W.; Seo, M. J.; Hong, J. W.; Ha, J. W., Tuning Chemical Interface Damping: Interfacial Electronic Effects of Adsorbate Molecules and Sharp Tips of Single Gold Bipyramids. *Nano Lett.* **2019**, *19* (4), 2568.
23. Nehl, C. L.; Liao, H.; Hafner, J. H., Optical Properties of Star-Shaped Gold Nanoparticles. *Nano Letters* **2006**, *6* (4), 683-688.
24. Smith, K. W.; Yang, J.; Hernandez, T.; Swearer, D. F.; Scarabelli, L.; Zhang, H.; Zhao, H.; Moringo, N. A.; Chang, W.-S.; Liz-Marzán, L. M.; Ringe, E.; Nordlander, P.; Link, S., Environmental Symmetry Breaking Promotes Plasmon Mode Splitting in Gold Nanotriangles. *The Journal of Physical Chemistry C* **2018**, *122* (25), 13259-13266.
25. Moerner, W. E., Single-Molecule Spectroscopy, Imaging, and Photocontrol: Foundations for Super-Resolution Microscopy (Nobel Lecture). *Angewandte Chemie International Edition* **2015**, *54* (28), 8067-8093.
26. Hauck, T. S.; Ghazani, A. A.; Chan, W. C. W., Assessing the Effect of Surface Chemistry on Gold Nanorod Uptake, Toxicity, and Gene Expression in Mammalian Cells. *Small* **2008**, *4* (1), 153-159.
27. Martinsson, E.; Shahjamali, M. M.; Large, N.; Zraee, N.; Zhou, Y.; Schatz, G. C.; Mirkin, C. A.; Aili, D., Influence of Surfactant Bilayers on the Refractive Index Sensitivity and Catalytic Properties of Anisotropic Gold Nanoparticles. *Small* **2016**, *12* (3), 330-342.
28. Li, H.; Singh, A.; Bayram, F.; Childress, A. S.; Rao, A. M.; Koley, G., Impact of oxygen plasma treatment on carrier transport and molecular adsorption in

- graphene. *Nanoscale* **2019**, *11* (23), 11145-11151.
29. Guo, Y.; Zhu, X.; Li, N.; Yang, J.; Yang, Z.; Wang, J.; Yang, B., Molecular Sensitivities of Substrate-Supported Gold Nanocrystals. *The Journal of Physical Chemistry C* **2019**, *123* (12), 7336-7346.
30. Alba, M.; Pazos-Perez, N.; Vaz, B.; Formentin, P.; Tebbe, M.; Correa-Duarte, M. A.; Granero, P.; Ferré-Borrull, J.; Alvarez, R.; Pallares, J.; Fery, A.; de Lera, A. R.; Marsal, L. F.; Alvarez-Puebla, R. A., Macroscale Plasmonic Substrates for Highly Sensitive Surface-Enhanced Raman Scattering. *Angewandte Chemie International Edition* **2013**, *52* (25), 6459-6463.
31. Taylor, A. B.; Siddiquee, A. M.; Chon, J. W. M., Below Melting Point Photothermal Reshaping of Single Gold Nanorods Driven by Surface Diffusion. *ACS Nano* **2014**, *8* (12), 12071-12079.
32. Censabella, M.; Grimaldi, M. G.; Ruffino, F., Shape design of supported Au nanorods through morphological evolution: Coalescence, instability, reshaping. *Materials Characterization* **2019**, *147*, 101-115.
33. Khalavka, Y.; Ohm, C.; Sun, L.; Banhart, F.; Sönnichsen, C., Enhanced Thermal Stability of Gold and Silver Nanorods by Thin Surface Layers. *The Journal of Physical Chemistry C* **2007**, *111* (35), 12886-12889.
34. Mohamed, M. B.; Ismail, K. Z.; Link, S.; El-Sayed, M. A., Thermal Reshaping of Gold Nanorods in Micelles. *The Journal of Physical Chemistry B* **1998**, *102* (47), 9370-9374.
35. Wang, Y.; Teitel, S.; Dellago, C., Surface-Driven Bulk Reorganization of

Gold Nanorods. *Nano Letters* **2005**, *5* (11), 2174-2178.

36. Katarzyna, W., Morphological changes of gold nanoparticles due to adsorption onto silicon substrate and oxygen plasma treatment. *RSC advances* **2014**, *v. 4* (no. 25), pp. 12729-12736-2014 v.4 no.25.

37. Lee, S. Y.; Ha, J. W., Characterizing the optical properties of single palladium-coated core-shell gold nanorods as multifunctional orientation probes. *Physical Chemistry Chemical Physics* **2016**, *18* (48), 32682-32685.

38. Moon, S. W.; Tsalu, P. V.; Ha, J. W., Single particle study: size and chemical effects on plasmon damping at the interface between adsorbate and anisotropic gold nanorods. *Physical Chemistry Chemical Physics* **2018**, *20* (34), 22197-22202.

4.1.7 Figures and Captions

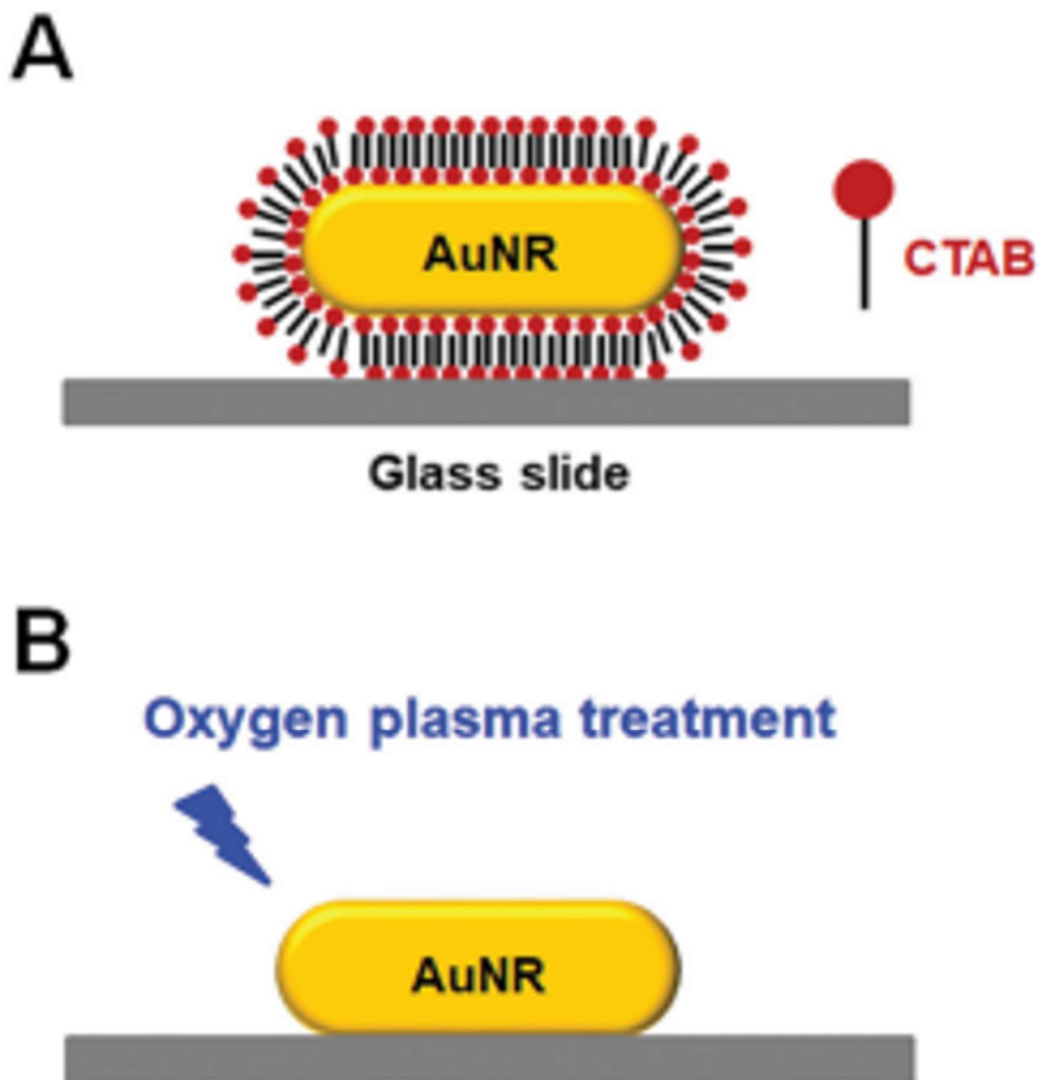


Figure 32. Schematics of (A) a CTAB-capped AuNR on the glass slide substrate before the oxygen plasma treatment, and (B) removal of CTAB from the AuNR surface by oxygen plasma treatment.

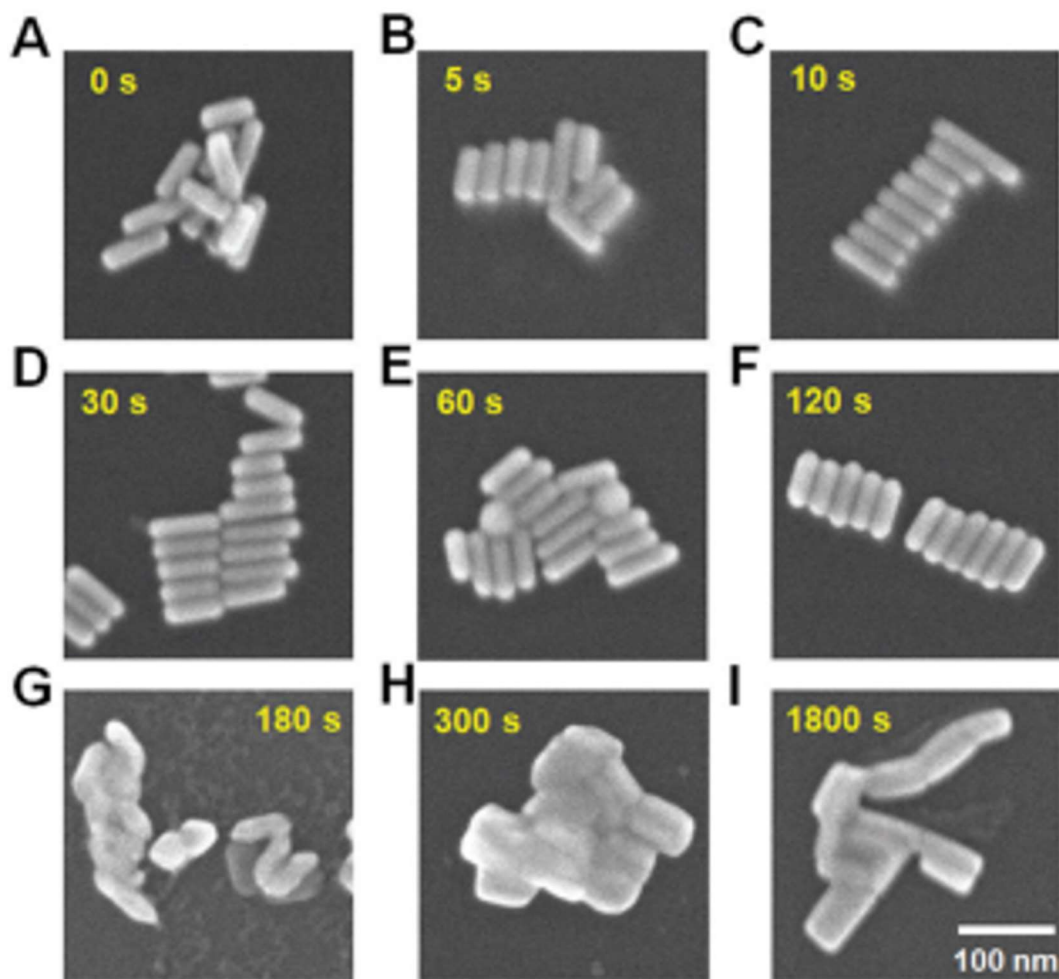


Figure 33. (A–I) SEM images of AuNRs after different oxygen plasma treatment times. A large structural deformation is observed at 180 s. In the *ex-situ* measurements, a new sample was used for each exposure time.

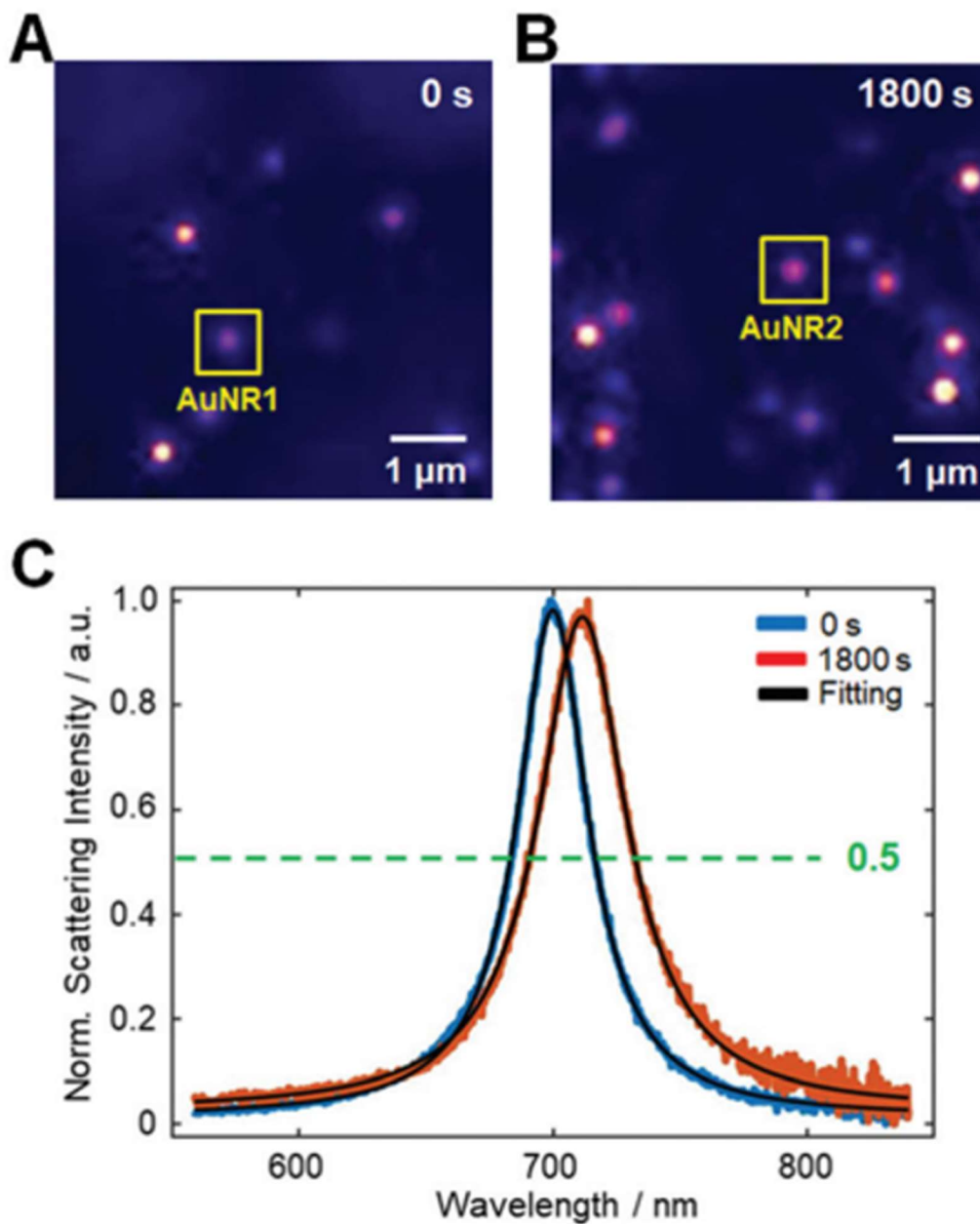


Figure 34. (A, B) DF images of single AuNRs before and after 1800 s of oxygen plasma treatment, respectively. (C) Normalized DF spectra of two AuNRs (AuNR1 and AuNR2) highlighted by the yellow-edged squares in panels (A) and (B). The scattering spectra were fitted by the Lorentzian function to extract the homogeneous LSPR linewidth and LSPR wavelength.

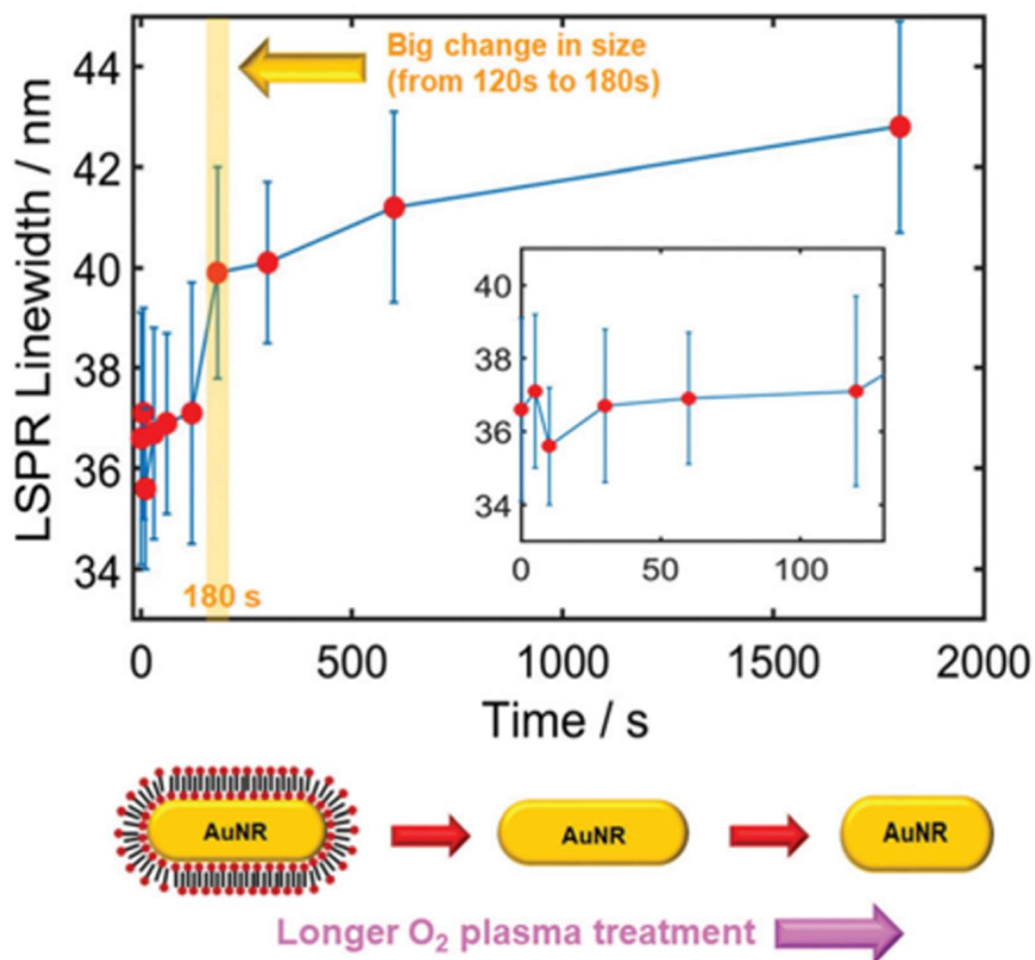


Figure 35. LSPR linewidth of AuNRs versus plasma treatment time. Increasing the oxygen plasma treatment time for removing the CTAB capping material shortened the AuNRs, as shown in the schematic. The inset is an enlargement of the main plot in the range of 0–120 s.

4.1.8 Supplementary Materials

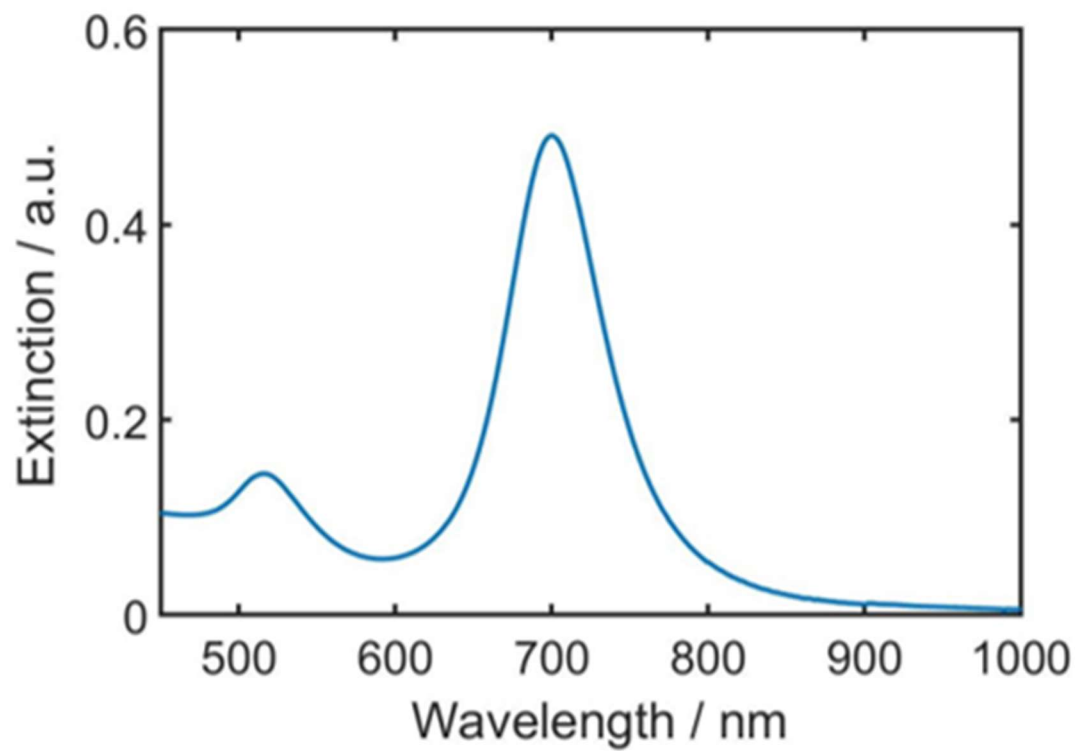


Figure S14. UV-Vis extinction spectrum of AuNRs (25 nm × 73 nm on average) showing two distinct transverse and longitudinal LSPR peaks.

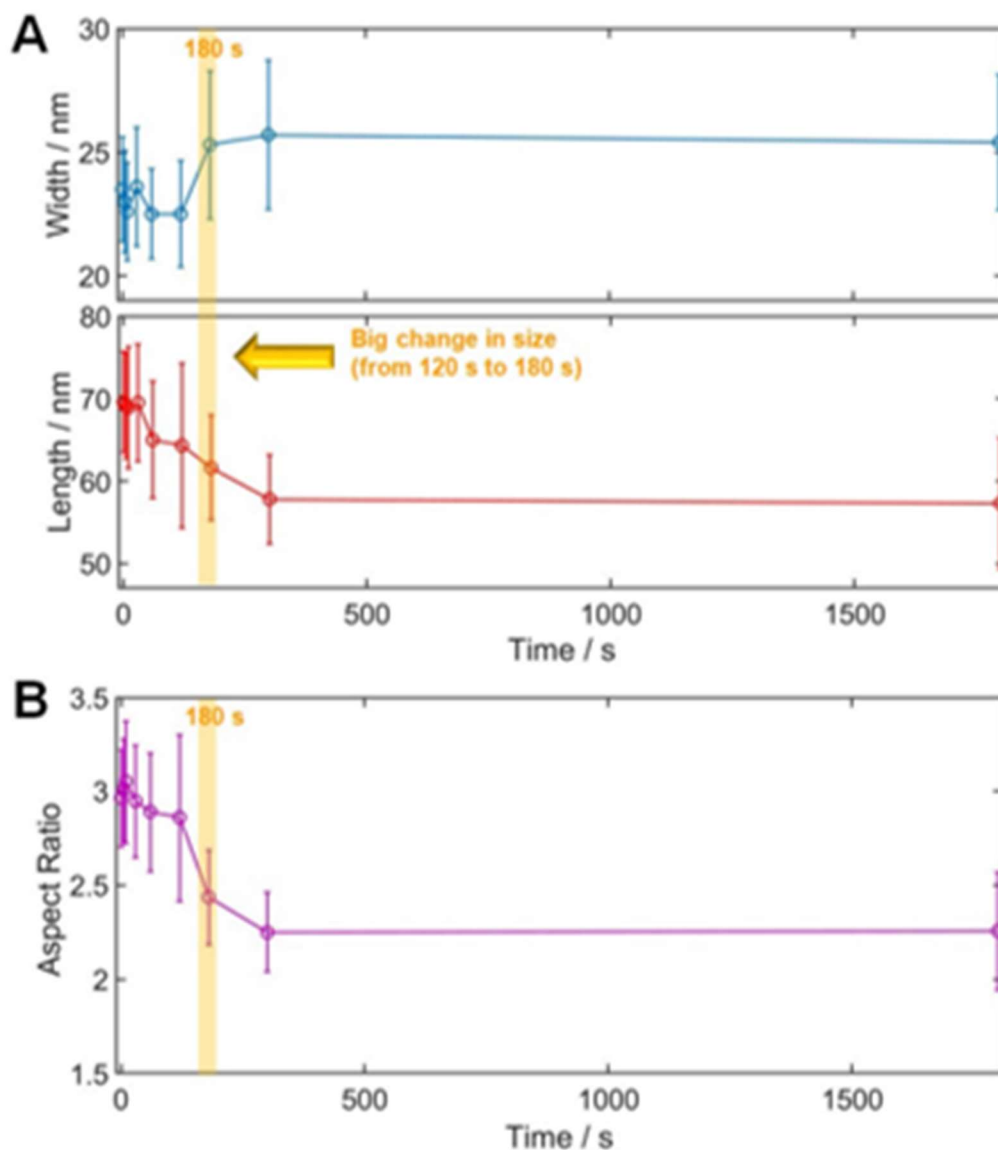


Figure S15. (A) Changes in the width (top) and length (bottom) of AuNRs as a function of the plasma treatment time (0, 5, 10, 30, 60, 120, 180, 300, and 1800 s). (B) Corresponding change in aspect ratio (AR) of AuNRs.

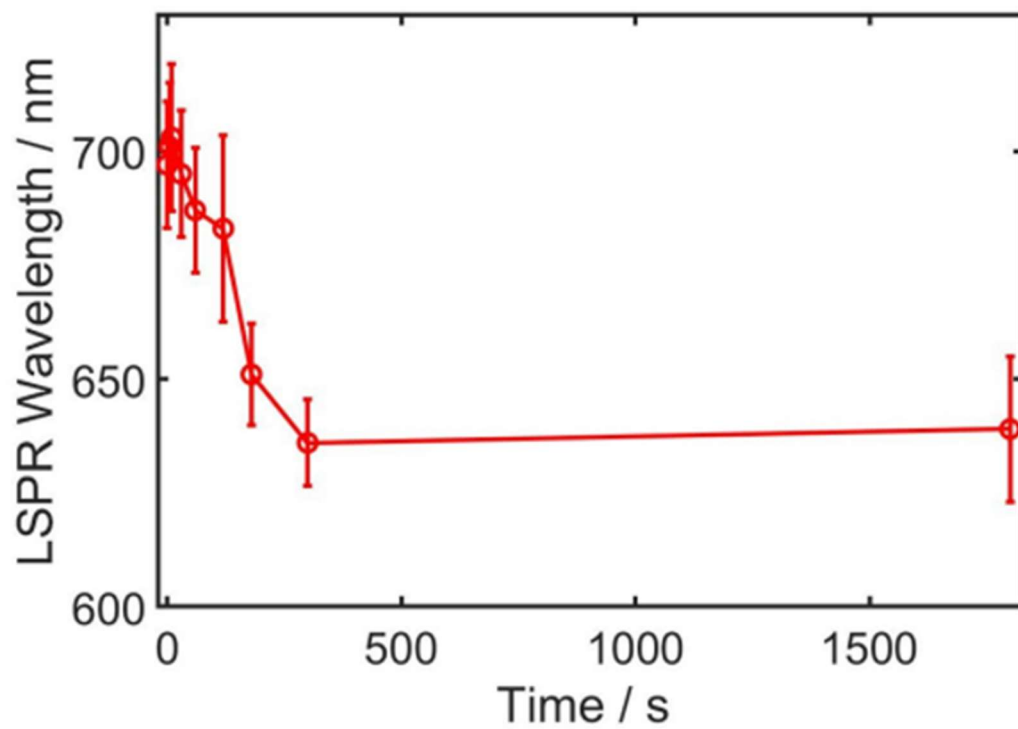


Figure S16. Changes in the LSPR wavelength of AuNRs as a function of the plasma treatment time (0, 5, 10, 30, 60, 120, 180, 300, and 1800 s).

4.2 Single-Particle Study: Plasmonic Damping Induced by Mercury Amalgamation in Mesoporous Silica Coated Gold Nanorods

Geun Wan Kim, and Ji Won Ha*

A paper in preparation to be published

*Corresponding author

4.2.1 Abstract

Amalgamation is a concentrating process in which metallic gold or silver is mixed with mercury (Hg). In this work, we investigated the plasmon damping of individual mesoporous silica coated gold nanorods (AuNRs@mSiO₂) caused by the formation of the Hg-Au alloy structure. First, we compared the structural change and the formation of the Hg-Au alloy of bare AuNRs and AuNRs@mSiO₂ using scanning electron microscopy (SEM) and energy-dispersive x-ray spectroscopy (EDS). In the Hg amalgamation, the aspect ratio of bare AuNRs decreased due to Hg amalgam formation. Still, then that of AuNRs@mSiO₂ were unchanged because the silica shell suppressed the deformation of core-AuNR. Second, dark-field (DF) microscopy and spectroscopy were used to gain deeper insight into the optical properties and plasmon damping of the Hg-AuNRs@mSiO₂ at the single particle level. A strong plasmon damping in the scattering spectra of individual Hg-AuNRs@mSiO₂ was observed due to the formation of Hg amalgamation on the core AuNR surface. Finally, we performed in-situ monitoring of strong plasmonic damping resulting from Hg amalgamation. We confirmed the optical change due to deposition and slow diffusion of Hg on the surface of core AuNR without deformation. Furthermore, the results indicate that the plasmon

damping in single AuNRs@mSiO₂ can be used as a promising strategy for Hg sensing.

4.2.2 Introduction

There have been numerous studies with the goal of improving the magnetic,¹⁻³ catalytic,⁴⁻⁶ and optical^{7,8} properties of bimetallic nanoparticles. Nanoalloy structure^{9,10} consisting of two or more metal elements display improved chemical and optical properties compared with the pure metal nanostructure. Moreover, recent advances in the synthesis of metallic nanoparticles attracted a growing interest in bimetallic nanoparticles, which have desired shape, narrow size distribution, and component elements. However, we have a limited understanding of the changes in optical and chemical properties of nanoalloy structures during the growth process.

Because of recent advances in nanotechnology, Mercury (Hg) amalgam, typical and traditional nanoalloys, was employed for the new application in several fields. Strong affinity and amalgam formation between Hg and Gold (Au) was used to accurately sense mercury¹¹⁻¹⁶ and water purification by removing mercury ions from polluted water¹⁷⁻¹⁹. Despite the previous study on the growth process of Hg amalgamation²⁰⁻²², the change of physical and chemical properties of metallic nanoparticles during Hg amalgamation was not fully understood.

The optical properties of noble metal nanoparticles based on localized surface plasmon resonance (LSPR) effect are affected by size²³, shape^{10, 24}, and refractive index of surrounding medium²⁵. Especially, Anisotropic Au nanoparticles such as Au nanorods (AuNRs)²⁶, nanourchins²⁷, nanostars²⁸, bipyramids²⁹, nanoplates³⁰ have been

widely investigated due to their optical properties induced by anisotropic shape. During Hg amalgamation, it is well known that AuNRs undergo the deformation from rod shape to spherical shape²⁰⁻²². Deformation of AuNRs induced by Hg amalgamation makes a change of optical properties, which makes it difficult to understand the bimetallic effect during Hg amalgamation.

Our previous study presented that the silica shell on AuNRs improves structural and spectral stability to core AuNRs while interfering negligibly with their chemical and physical properties.³¹ Thus, the thermodynamic stability of AuNPs can be dramatically enhanced by silica shells and maintain the optical properties. In this study, we demonstrate the effect of the mesoporous silica coating of AuNRs according to Hg amalgamation. The changes of optical properties of nanorods were observed by DF microscopy. Detailed SEM image analysis revealed the structural stability of AuNR@mSiO₂ when exposed to Hg amalgamation solution. The distribution of the Hg element on nanorods was confirmed by EDX analysis. In-situ monitoring of Hg amalgamation under DF microscopy was also carried out to deeper understand the formation of the Hg-Au core-shell structure.

4.2.3 Experimental Section

Materials and Sample Preparation.

AuNRs with 25 nm × 73 nm and AuNRs@mSiO₂ were obtained from Nanopartz (Loveland, CO, USA). The AuNRs colloid solution was first diluted with 18.2-M Ω pure water to the appropriate concentration. The diluted solution was then

sonicated for 15 min at room temperature. The samples were prepared by spin-casting the AuNPs solution onto a pre-cleaned glass slide. Subsequently, a 22 mm × 22 mm no. 1.5 coverslip (Corning, NY) was placed on the glass slide. In this study, the concentration of AuNPs on the glass surface was controlled to approximately $1 \mu\text{m}^{-2}$ to facilitate single-particle characterization and minimize interparticle LSPR coupling, which can result in a spectral shift.

Structural Characterization.

Structural characterizations, Energy dispersive X-ray analysis and X-ray elemental mapping of AuNRs before and after amalgamation were carried out using a scanning electron microscope (SEM) (Nano230 FE-SEM, FEI, Czech).

Scattering-based Dark-Field Microscopy.

DF microscopy imaging was performed under a Nikon inverted microscope (ECLIPSE Ti-U). In DF mode, the microscope utilized a Nikon Plan Fluor 100× 0.5-1.3 oil iris objective and a Nikon DF condenser. An Andor iXonEM+ CCD camera (iXon Ultra 897) was used to record highly detailed DF scattering images of AuNRs and AuNRs@mSiO₂. The collected images were analyzed using ImageJ.

Single Particle Scattering Spectroscopy.

DF scattering spectra were acquired with an Andor spectrophotometer (SHAMROCK 303i, SR-303I-A) connected with an Andor CCD camera (Newton

DU920P-OE). When obtaining a spectrum, the scanning stage moved the sample to the desired location so that only scattered light from the selected location was collected by the objective. The scattered light was directed to the entrance of the spectrophotometer, dispersed by a grating (300 l/mm), and detected by the Newton CCD camera. The background was measured at a region without any particles. Data analysis was performed with specially designed Matlab programs.

4.2.4 Result and Discussion

In this study, Hg-Au core-shell structure was formed by direct exposure of AuNRs and AuNR@mSiO₂ immobilized on glass slides to HgCl₂ and NaBH₄ solution. We conducted an experiment comparing Bare AuNR and AuNRs coated with a mesoporous silica shell. **Fig. 36** displays the schematic images before and after Hg amalgamation of bare AuNR and AuNR@mSiO₂. In a previous study, a decrease of the aspect ratio of bare AuNR is well known during the Hg amalgamation²⁰⁻²². After spin-casting, the AuNR@mSiO₂ solution on a pre-cleaned slide glass, both bare AuNR and AuNR@mSiO₂ were deposited as shown in **Fig. 36**. The medium of the sample was then exchanged for the Hg amalgamation solution. The Hg²⁺ ion in the Hg amalgamation solution was reduced by NaBH₄ and adsorbed onto the surface of AuNRs and AuNR@mSiO₂. In this step, deposition of the Hg atom on the surface of AuNRs leads to the formation of an Au-Hg core-shell structure due to the high affinity between Au and Hg. Next step, the diffusion of Au atoms at the Au/Hg interface or in the Hg shell led to deformation of AuNRs due to lower cohesive energy of Hg (0.67

eV/atom) versus Au (3.81 eV/atom). During this step, the aspect ratio of AuNRs is reduced because the Hg amalgamation preferential occurred at both tips of AuNRs that reducing the length of it.

FE-SEM, EDX and elemental mapping and line scanning were used to characterize the morphology and composition of AuNRs@mSiO₂ before and after Hg amalgamation. In the previous study, the aspect ratio of Bare AuNR (25 nm × 73 nm) was gradually decreasing after Hg amalgamation. **Fig. S17** displays the same result as the previous works. In the present study, we characterized the structural changes of the AuNRs@mSiO₂ after Hg amalgamation and verified the effect of silica coating on the structural stability of AuNR cores. SEM images of bare AuNR and AuNRs@mSiO₂ were obtained after 1 hour reaction time. As shown in **Fig. 37 A, C**, the aspect ratio of AuNRs@mSiO₂ was not gradually increasing during Hg amalgamation. This result is clearly different from bare AuNRs, which display significant structural deformation after amalgamation. Because there is no significant change of AuNR@mSiO₂, we obtained the EDX elemental mapping analysis to clarify whether Hg amalgamation occurs to AuNR cores in a mesoporous silica shell. In EDX elemental mapping image (**Fig. 37C, D, F**), we can see that Au and Hg atoms appeared along the core AuNRs. Therefore, we confirmed that the silica shell significantly enhanced the structural stability of AuNRs despite Hg amalgamation.

From the obtained SEM images, we characterized the structural changes of both particles and constructed length and diameter histograms. In absence of amalgamation solution, AuNRs show approximately 25 nm in diameter and 73 nm in

length, the aspect ratio of 2.78, (**Fig. 38A**). However, after Hg amalgamation, the average diameter and length of bare AuNR were 31.8 nm and 65.7 nm, respectively, giving and the aspect ratio of 2.07. More images of bare AuNR can be found in supplementary materials **Fig. S17A, B**. Before Hg amalgamation, the average aspect ratio of AuNRs@mSiO₂ is 2.76, 33.6 nm in diameter and 92.8 nm in length, respectively (**Fig. 38B**). After Hg amalgamation for 1 hour, the average aspect ratio is approximately 2.92, 31.8 nm and 93.1 nm, respectively.

Next, we investigated the LSPR spectral changes of both bare AuNRs and AuNR@mSiO₂ before and after Hg amalgamation under scattering based DF microscopy. The LSPR linewidths can present understanding into plasmonic damping in single Au nanoparticles. Plasmonic damping is closely associated with plasmon energy loss, which considerably reduces the scattering intensity and broadens the linewidth of the LSPR spectrum. **Fig. 39A** shows the DF images of the bare AuNRs immobilized on the slide glass, and **Fig. 39B** shows a DF image of AuNRs@mSiO₂. **Fig. 39C, D** provided their normalized single particle scattering spectra before and after Hg amalgamation from both particles highlighted by red dashed square. In single particle spectra of both particles, there are remarkable spectral changes that LSPR blue shift and linewidth broadening. The average longitude LSPR wavelength of bare AuNR was 1.748 eV and the average full width at half maximum (FWHM) was 79.75 meV. After injecting Hg amalgamation solutions, LSPR wavelength appeared at 1.827 eV, FWHM was 241.5 meV due to strong plasmonic damping induced by Hg amalgamation. While AuNR@mSiO₂ shows the LSPR wavelength at 1.702 eV and

FWHM at 111.5 meV before amalgamation. Next, after an hour of Hg amalgamation, the LSPR peak was 1.807 eV and FWHM was 140.8 meV.

To obtain deeper insight into LSPR spectral changes caused by Hg amalgamation, the in-situ monitoring of Hg amalgamation was conducted. After spin-casting both bare AuNRs and AuNR@mSiO₂ solution on a pre-cleaned slide glass, we obtained the initial single particle spectrum of each particle on water medium. Next, we take the single particle spectra every 3 minutes after replacing the medium from water to Hg amalgamation solution. **Fig. 40A, B** plots the LSPR shift and linewidth broadening versus Hg amalgamation time. For the first 3 minutes, Bare AuNRs show fast and strong plasmonic damping due to the adsorption of Hg atoms onto the surface of Bare AuNRs. Since then, slight spectral changes were occurred induced by diffusion of Hg atom into AuNRs. Because of the mesoporous silica shell, which disturbs the access of Hg atom to AuNR cores, Hg amalgamation of AuNR@mSiO₂ is slower than bare AuNRs. However, for an hour, we can see steady spectral changes caused by adsorption and diffusion of Hg atoms into the AuNR core. Therefore, we observed spectral changes caused by the formation of Hg-Au nanoalloy structure that induces strong plasmonic damping without structural change of AuNR core in a mesoporous silica shell.

4.2.5 Conclusion

In summary, we demonstrate the effect of Hg amalgamation on structural and spectral changes of AuNRs@mSiO₂ by LSPR linewidth broadening due to plasmonic

damping at the single particle level. First, in SEM image analysis, the aspect ratio of AuNRs@mSiO₂ was nearly constant compared with bare AuNR due to structural stability based on the mesoporous silica shell. However, we also find that Hg amalgamation occurred by EDX element mapping data that Hg elements appeared along the AuNR core. In addition, we observed the significant broadening of the LSPR spectrum during the Hg amalgamation because the formation of Hg amalgam induces strong plasmonic damping. This result supports that spectral change induced by Hg amalgamation can be observed without effects of structural changes because the mesoporous silica coating enhanced the structural stability of AuNR core.

4.2.6 References

1. Liu, F.; Zhu, J.; Yang, W.; Dong, Y.; Hou, Y.; Zhang, C.; Yin, H.; Sun, S., Building Nanocomposite Magnets by Coating a Hard Magnetic Core with a Soft Magnetic Shell. *Angewandte Chemie International Edition* **2014**, *53* (8), 2176-2180.
2. Bridot, J.-L.; Faure, A.-C.; Laurent, S.; Rivière, C.; Billotey, C.; Hiba, B.; Janier, M.; Jossierand, V.; Coll, J.-L.; Vander Elst, L.; Muller, R.; Roux, S.; Perriat, P.; Tillement, O., Hybrid Gadolinium Oxide Nanoparticles: Multimodal Contrast Agents for in Vivo Imaging. *Journal of the American Chemical Society* **2007**, *129* (16), 5076-5084.
3. Selvan, S. T.; Patra, P. K.; Ang, C. Y.; Ying, J. Y., Synthesis of Silica-Coated Semiconductor and Magnetic Quantum Dots and Their Use in the Imaging of Live Cells. *Angewandte Chemie International Edition* **2007**, *46* (14), 2448-2452.
4. Blomberg, S.; Gustafson, J.; Martin, N. M.; Messing, M. E.; Deppert, K.; Liu, Z.; Chang, R.; Fernandes, V. R.; Borg, A.; Grönbeck, H.; Lundgren, E., Generation and oxidation of aerosol deposited PdAg nanoparticles. *Surface Science* **2013**, *616*, 186-191.
5. Ullah, S.; Ferreira-Neto, E. P.; Pasa, A. A.; Alcântara, C. C. J.; Acuña, J. J. S.; Bilmes, S. A.; Martínez Ricci, M. L.; Landers, R.; Fermino, T. Z.; Rodrigues-Filho, U. P., Enhanced photocatalytic properties of core@shell SiO₂@TiO₂ nanoparticles. *Applied Catalysis B: Environmental* **2015**, *179*, 333-343.
6. Qi, J.; Chen, J.; Li, G.; Li, S.; Gao, Y.; Tang, Z., Facile synthesis of

core-shell Au@CeO₂ nanocomposites with remarkably enhanced catalytic activity for CO oxidation. *Energy & Environmental Science* **2012**, *5* (10), 8937-8941.

7. Lim, J.; Jeong, B. G.; Park, M.; Kim, J. K.; Pietryga, J. M.; Park, Y.-S.; Klimov, V. I.; Lee, C.; Lee, D. C.; Bae, W. K., Influence of Shell Thickness on the Performance of Light-Emitting Devices Based on CdSe/Zn_{1-x}Cd_xS Core/Shell Heterostructured Quantum Dots. *Advanced Materials* **2014**, *26* (47), 8034-8040.

8. Kim, T.; Kang, H.; Jeong, S.; Kang, D. J.; Lee, C.; Lee, C.-H.; Seo, M.-K.; Lee, J.-Y.; Kim, B. J., Au@Polymer Core-Shell Nanoparticles for Simultaneously Enhancing Efficiency and Ambient Stability of Organic Optoelectronic Devices. *ACS Applied Materials & Interfaces* **2014**, *6* (19), 16956-16965.

9. Ferrando, R.; Jellinek, J.; Johnston, R. L., Nanoalloys: From Theory to Applications of Alloy Clusters and Nanoparticles. *Chemical Reviews* **2008**, *108* (3), 845-910.

10. Cortie, M. B.; McDonagh, A. M., Synthesis and Optical Properties of Hybrid and Alloy Plasmonic Nanoparticles. *Chemical Reviews* **2011**, *111* (6), 3713-3735.

11. Rex, M.; Hernandez, F. E.; Campiglia, A. D., Pushing the Limits of Mercury Sensors with Gold Nanorods. *Analytical Chemistry* **2006**, *78* (2), 445-451.

12. Huang, H.; Qu, C.; Liu, X.; Huang, S.; Xu, Z.; Zhu, Y.; Chu, P. K., Amplification of localized surface plasmon resonance signals by a gold nanorod assembly and ultra-sensitive detection of mercury. *Chemical Communications* **2011**,

47 (24), 6897-6899.

13. Singh, A.; Pasricha, R.; Sastry, M., Ultra-low level optical detection of mercuric ions using biogenic gold nanotriangles. *Analyst* **2012**, *137* (13), 3083-3090.

14. James, J. Z.; Lucas, D.; Koshland, C. P., Gold Nanoparticle Films As Sensitive and Reusable Elemental Mercury Sensors. *Environmental Science & Technology* **2012**, *46* (17), 9557-9562.

15. Deng, L.; Ouyang, X.; Jin, J.; Ma, C.; Jiang, Y.; Zheng, J.; Li, J.; Li, Y.; Tan, W.; Yang, R., Exploiting the Higher Specificity of Silver Amalgamation: Selective Detection of Mercury(II) by Forming Ag/Hg Amalgam. *Analytical Chemistry* **2013**, *85* (18), 8594-8600.

16. Crockett, J. R.; Win-Piazza, H.; Doebler, J. E.; Luan, T.; Bao, Y., Plasmonic Detection of Mercury via Amalgamation on Gold Nanorods Coated with PEG-Thiol. *ACS Applied Nano Materials* **2021**, *4* (2), 1654-1663.

17. Ojea-Jiménez, I.; López, X.; Arbiol, J.; Puentes, V., Citrate-Coated Gold Nanoparticles As Smart Scavengers for Mercury(II) Removal from Polluted Waters. *ACS Nano* **2012**, *6* (3), 2253-2260.

18. Lo, S.-I.; Chen, P.-C.; Huang, C.-C.; Chang, H.-T., Gold Nanoparticle–Aluminum Oxide Adsorbent for Efficient Removal of Mercury Species from Natural Waters. *Environmental Science & Technology* **2012**, *46* (5), 2724-2730.

19. Pacheco, S.; Medina, M.; Valencia, F.; Tapia, J., Removal of Inorganic Mercury from Polluted Water Using Structured Nanoparticles. *Journal of Environmental Engineering* **2006**, *132* (3), 342-349.

20. Liu, Y.; Huang, C. Z., Real-Time Dark-Field Scattering Microscopic Monitoring of the in Situ Growth of Single Ag@Hg Nanoalloys. *ACS Nano* **2013**, *7* (12), 11026-11034.
21. Schopf, C.; Wahl, A.; Martín, A.; O’Riordan, A.; Iacopino, D., Direct Observation of Mercury Amalgamation on Individual Gold Nanorods Using Spectroelectrochemistry. *The Journal of Physical Chemistry C* **2016**, *120* (34), 19295-19301.
22. Schopf, C.; Martín, A.; Schmidt, M.; Iacopino, D., Investigation of Au–Hg amalgam formation on substrate-immobilized individual Au nanorods. *Journal of Materials Chemistry C* **2015**, *3* (34), 8865-8872.
23. Sánchez-Iglesias, A.; Pastoriza-Santos, I.; Pérez-Juste, J.; Rodríguez-González, B.; García de Abajo, F. J.; Liz-Marzán, L. M., Synthesis and Optical Properties of Gold Nanodecahedra with Size Control. *Advanced Materials* **2006**, *18* (19), 2529-2534.
24. Mock, J. J.; Barbic, M.; Smith, D. R.; Schultz, D. A.; Schultz, S., Shape effects in plasmon resonance of individual colloidal silver nanoparticles. *The Journal of Chemical Physics* **2002**, *116* (15), 6755-6759.
25. Chen, H.; Kou, X.; Yang, Z.; Ni, W.; Wang, J., Shape- and Size-Dependent Refractive Index Sensitivity of Gold Nanoparticles. *Langmuir* **2008**, *24* (10), 5233-5237.
26. Pérez-Juste, J.; Pastoriza-Santos, I.; Liz-Marzán, L. M.; Mulvaney, P., Gold nanorods: Synthesis, characterization and applications. *Coordination Chemistry*

Reviews **2005**, *249* (17), 1870-1901.

27. Thapliyal, N. B.; Chiwunze, T. E.; Karpoormath, R.; Cherukupalli, S., Fabrication of highly sensitive gold nanourchins based electrochemical sensor for nanomolar determination of primaquine. *Materials Science and Engineering: C* **2017**, *74*, 27-35.

28. Senthil Kumar, P.; Pastoriza-Santos, I.; Rodríguez-González, B.; Javier García de Abajo, F.; Liz-Marzán, L. M., High-yield synthesis and optical response of gold nanostars. *Nanotechnology* **2007**, *19* (1), 015606.

29. Lee, S. Y.; Tsalu, P. V.; Kim, G. W.; Seo, M. J.; Hong, J. W.; Ha, J. W., Tuning Chemical Interface Damping: Interfacial Electronic Effects of Adsorbate Molecules and Sharp Tips of Single Gold Bipyramids. *Nano Letters* **2019**, *19* (4), 2568-2574.

30. Smith, K. W.; Yang, J.; Hernandez, T.; Swearer, D. F.; Scarabelli, L.; Zhang, H.; Zhao, H.; Moringo, N. A.; Chang, W.-S.; Liz-Marzán, L. M.; Ringe, E.; Nordlander, P.; Link, S., Environmental Symmetry Breaking Promotes Plasmon Mode Splitting in Gold Nanotriangles. *The Journal of Physical Chemistry C* **2018**, *122* (25), 13259-13266.

31. Lee, J.; Ha, J. W., Influence of oxygen plasma treatment on structural and spectral changes in silica-coated gold nanorods studied using total internal reflection microscopy and spectroscopy. *Analyst* **2021**, *146* (13), 4125-4129.

4.2.7 Figures and Captions

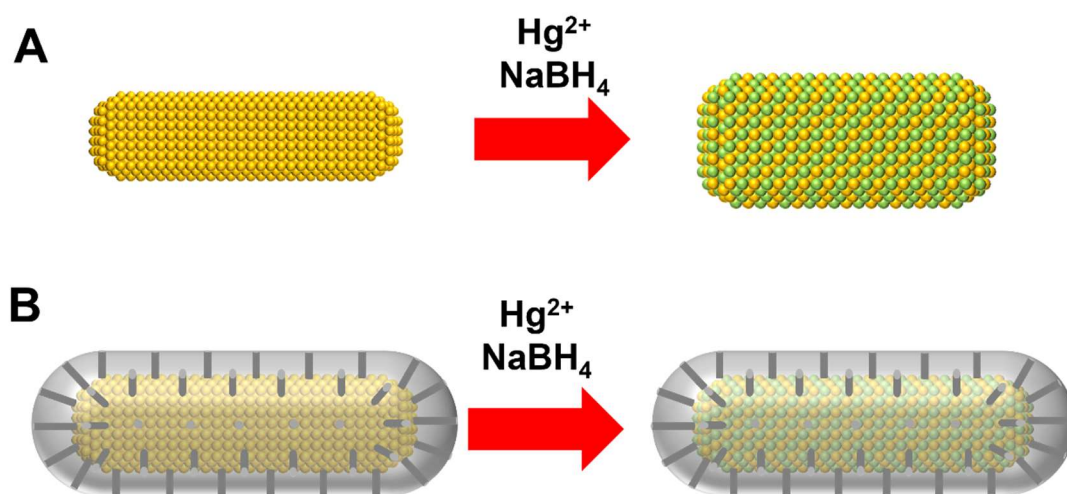


Figure 36. Schematics of Structural changes during mercury amalgamation of (A) Bare AuNR and (B) AuNR@mSiO₂.

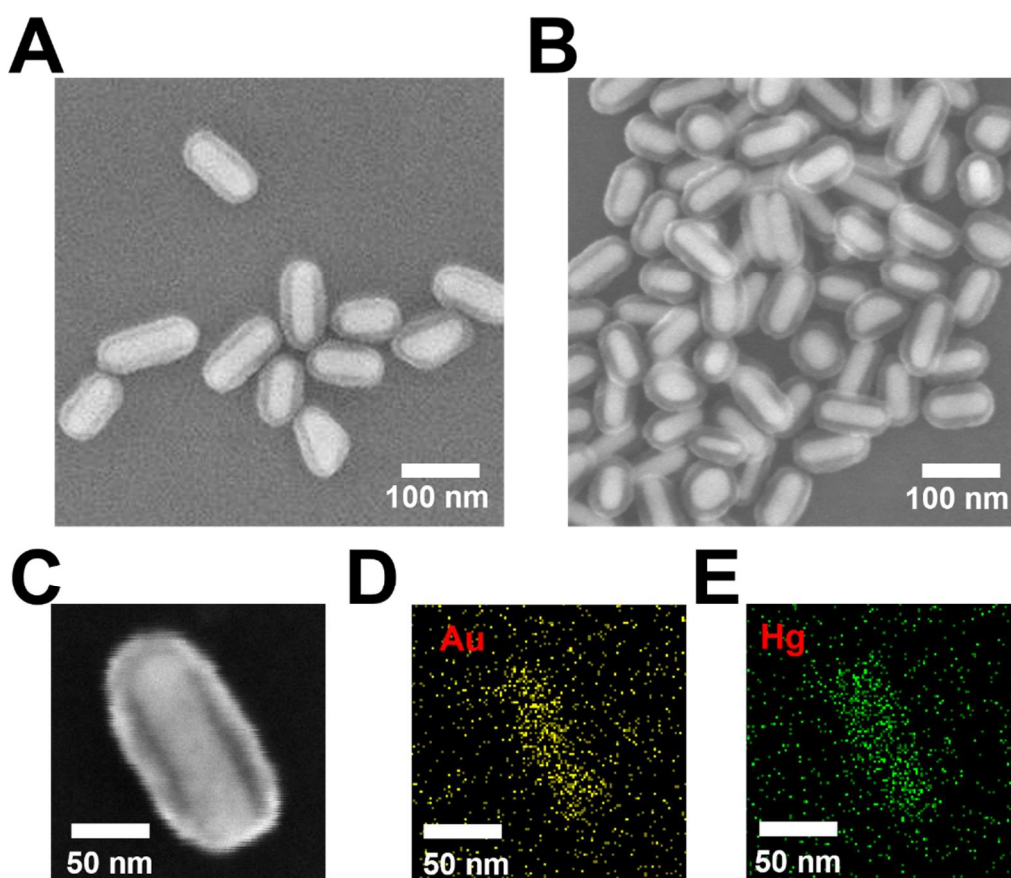


Figure 37. (A) Structure characterization of AuNRs@mSiO₂ and (B) after Hg amalgamation of AuNR@mSiO₂ (C) Enlarged SEM image and corresponding of Au (D) and Hg (E) elemental maps of Hg-AuNR@mSiO₂. Au and Hg elements were homogeneously distributed in the whole AuNR core.

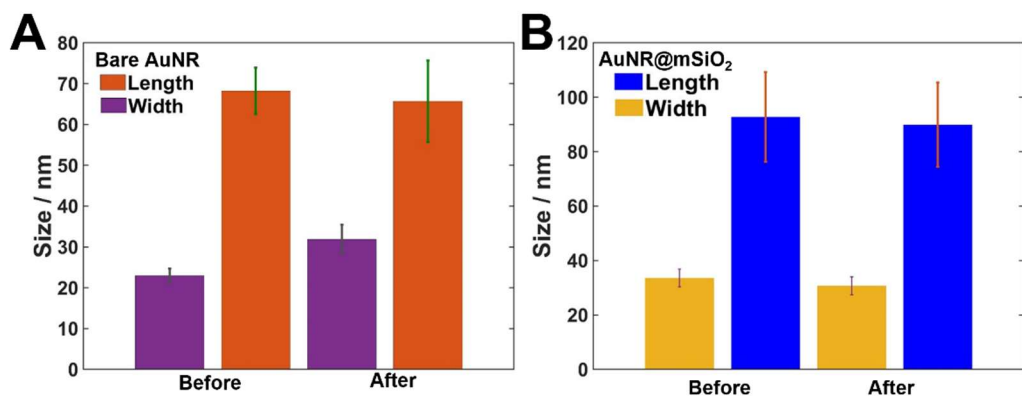


Figure 38. (A) TEM image analysis of the sizes (length and diameter) of bare AuNRs and (B) AuNRs@mSiO₂.

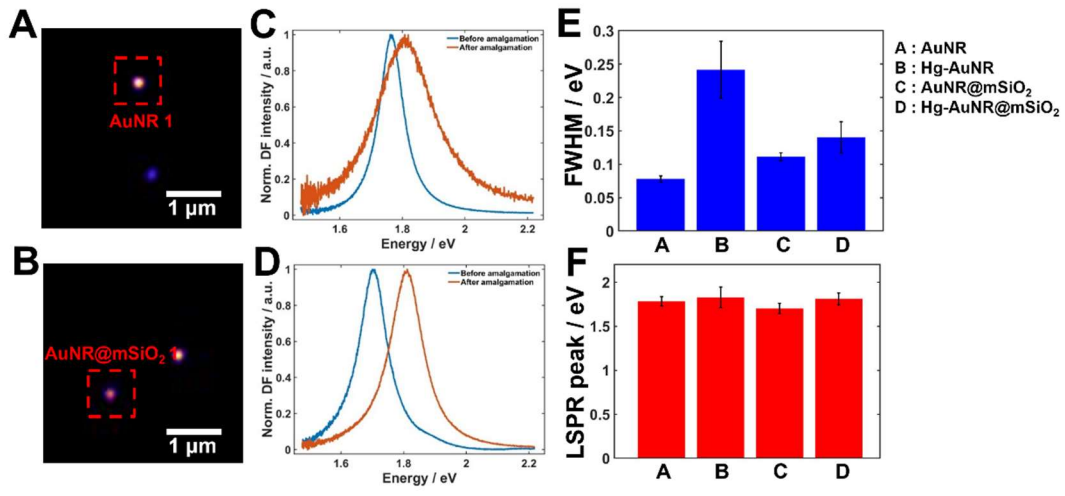


Figure 39. (A) DF scattering images of Bare AuNRs (B), AuNRs@mSiO₂. (C) The overlaid DF scattering spectra of AuNRs before and after amalgamation, (D) and AuNR@mSiO₂ (E) average FWHM and (F) LSPR wavelength based on cumstun MATLAB script.

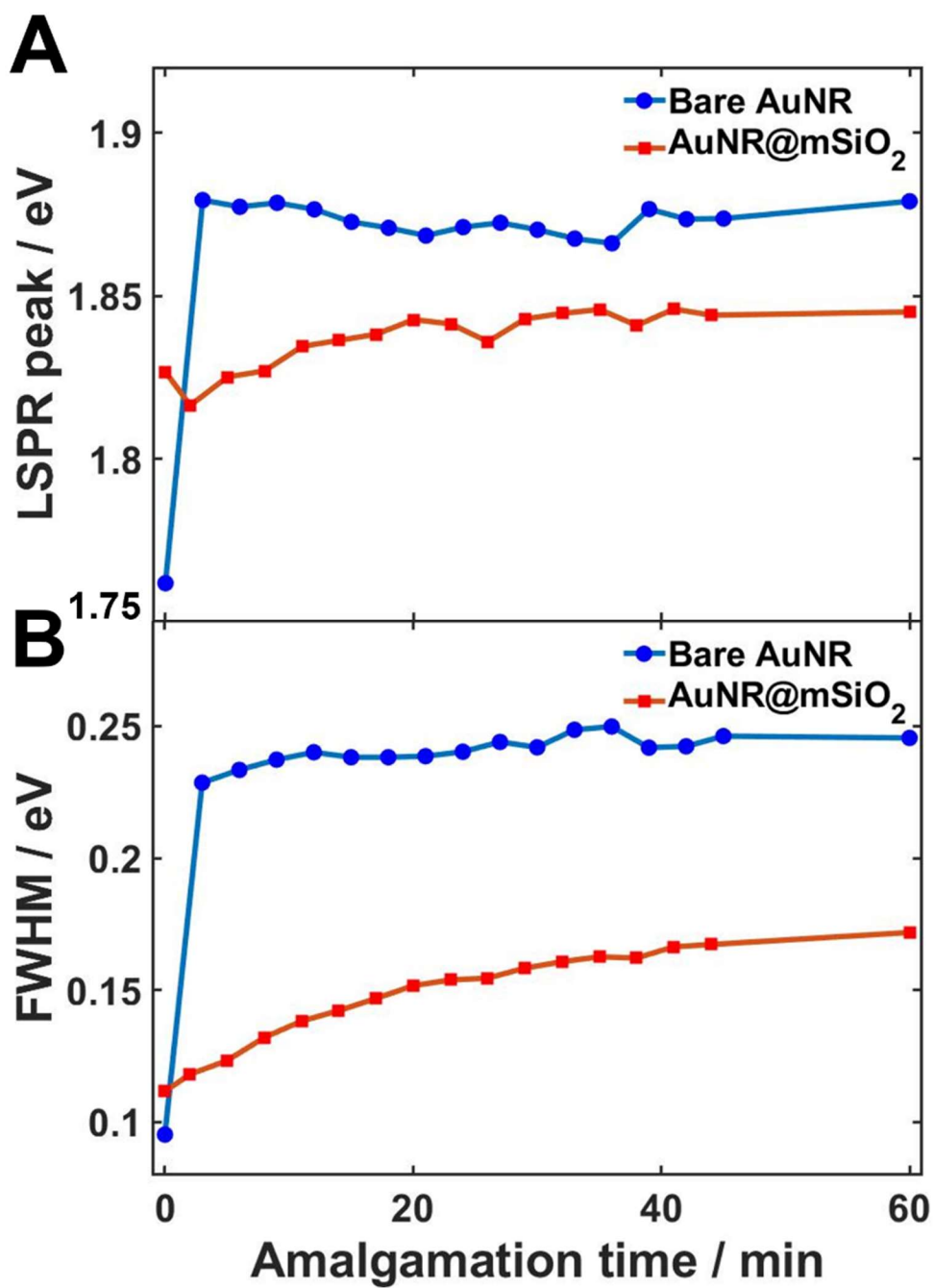


Figure 40. (A) Real time monitoring of the blue shift of LSPR wavelength and (B) FWHM of AuNR and AuNR@mSiO₂ due to mercury amalgamation.

4.2.8 Supplementary Materials

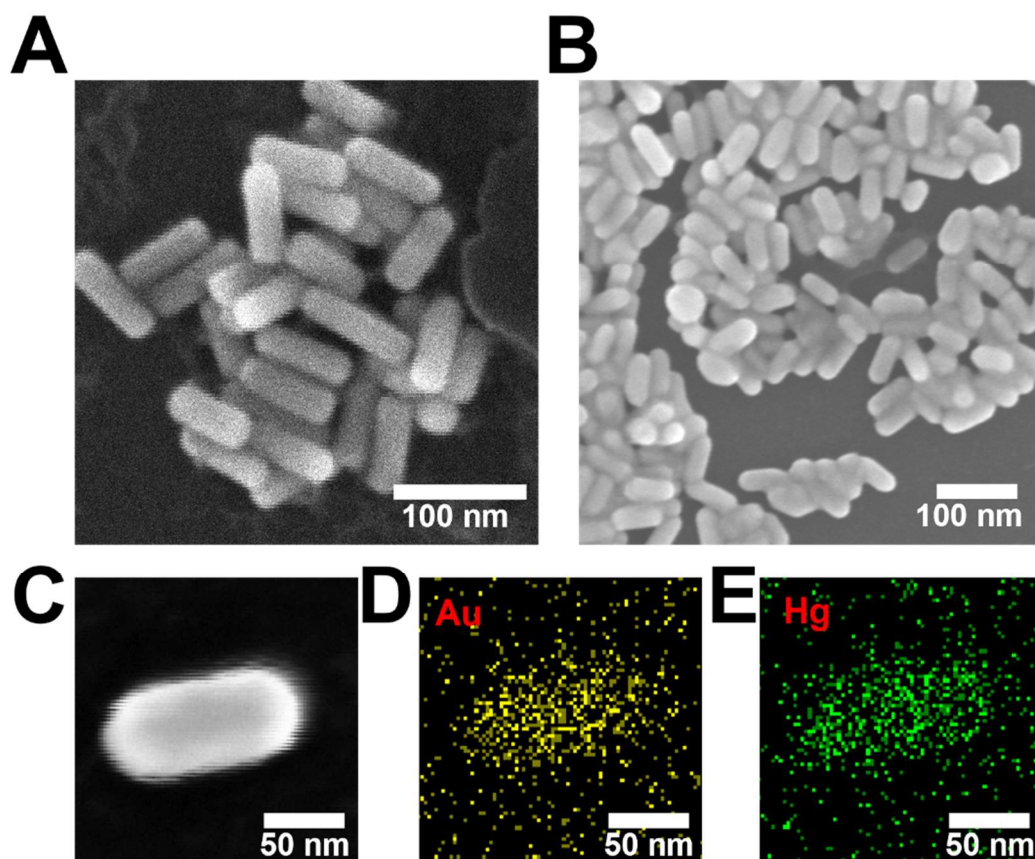


Figure S17. (A) Structure characterization of AuNRs and (B) after Hg amalgamation of AuNRs (C) Enlarged SEM image and corresponding of Au (D) and Hg (E) elemental maps of Hg-AuNR. Au and Hg elements were homogeneously distributed in the whole AuNR.

Chapter 5. Future Works

The light emitted by plasmonic nanoparticles can be used in imaging and sensing, allowing for precise local temperature measurements and chemical reactions at the nanoscale. It also contributes to SERS and plasmon-enhanced fluorescence. Thus, the emission mechanism of plasmonic nanoparticles is an important research topic. Furthermore, the light emitted by single AuNRs exhibits unique spectral characteristics, implying a close relationship with the LSPR, as the emission spectra closely match the corresponding DF scattering spectrum. Therefore, I believe that the emission spectrum of a single AuNR can be a helpful tool for analyzing the optical properties of AuNRs as well as various damping processes, including chemical interface damping.

In many cases, surface modification of plasmonic AuNPs with organic adsorbates, metal, dielectric depositions is required for functionalization, providing an additional source of plasmon damping. Surface scattering from these modifications has a significant impact on LSPR linewidth. This scattering affects the performance of plasmonic nanostructures in applications like LSPR sensing. Chemical interface damping, which is a particle-matter system containing particles and embedding materials, was investigated in previous studies. However, we have a limited understanding of plasmon damping generated by metal adsorbates or semiconductors for elongated metal nanoparticles. In particular, single particle studies on the damping competition between the organic material such as thiol, amine group, and metal or

semiconductor including platinum, palladium, titanium oxide, etc., adsorbed on the surface of AuNP give us a deeper understanding of the plasmonic damping process.

Acknowledgement

First and foremost, I would like to sincerely thank my advisor, Professor Ji Won Ha for his invaluable advice, scientific, professional, and personal, over my years as a graduate student. The work I have done on this thesis is simply one of the many testaments of the inspiration and drive he provides to his students. He brought me the excitement of exploring new knowledge, not only in research but also in life.

I express thanks to all of the members of my committee, Professor Youngil Lee, Professor Jong Wook Hong, Professor Yong-Ill Lee and Professor Seong Ho Kang for their efforts and contribution to the thesis. I would like to special thanks to Professor In-seob Han, and Professor Jung Heon Lee who provide the sample, HeLa cell and AuNRs@mSiO₂. I also want to thank all of group member not only current members, but also Alumni and my friends for their help and friendship.

Last but not least, I'd like to express my gratitude to my family, who have always supported and guided me in my endeavors. They have always backed me up and encouraged me.